TESTING A THERMAL STRESS ORIGIN OF FRACTURES IN PLUTONS OF THE SIERRA NEVADA BATHOLITH

A THESIS SUBMITTED TO THE GRADUATE DIVISION OF THE
UNIVERSITY OF HAWAI'I IN PARTIAL FULFILLMENT
OF THE REQUIREMENTS FOR THE DEGREE OF

MASTER OF SCIENCE

IN

GEOLOGY AND GEOPHYSICS

MAY 1998

By

Stephan Bergbauer

Thesis Committee:

Stephen J. Martel, Chairperson
Aly El-Kadi
John Sinton
Paul Wessel

We certify that we have read this thesis and that, in our opinion, it is satisfactory in scope and quality as a thesis for the degree of Master of Science in Geology and Geophysics.

THESIS COMMITTEE

____
Chairperson

____

____

____

Acknowledgments

This research was supported by the US Department of Energy office of Basic Energy Science through Contract No. DE-FG03-95ER14525. I thank Marty Grove for dating the samples. I also thank Chris Hieronymus for helping me set up the code, and Jordan Muller and Matt Long for their field assistance. Thanks to R. Batiza, K. Rubin, A. El-Kadi, J.M. Sinton, and P. Wessel for their comments. I also thank Nathan Becker for keeping my Mac running.

Paul,
thanks a lot for
your input on this.
I appreciate your
efforts.
Aloha,

Abstract

Field observations, geochemical data, geochronological information, and mechanical analyses together indicate that the formation of steeply dipping mineralized joints in the Lake Edison Granodiorite of the Sierra Nevada batholith in California was strongly influenced by thermal stresses that developed during the initial cooling of the pluton. At the scale of the pluton, joint orientations are represented by photolineament traces, which curve to approach the pluton boundaries at high angles. At the scale of an outcrop, joints approach the contact with the older Lamarck Granodiorite at high angles, and joint traces commonly terminate at or near the contact. These observations are consistent with joint-causing stresses having a thermal origin. The mineralogy of the epidote and chlorite fillings of the joints, in conjunction with radiometric dates from plutons and fractures, ties the formation of the joints to a time range consistent with the initial cooling of the pluton. A thermo-mechanical stress analysis assuming 2-D conductive cooling yields predicted thermal stresses that in key ways are consistent with the observed joint pattern. The orientation of the predicted most compressive thermal stress in the pluton is grossly consistent with the observed photolineament pattern if no tectonic stresses are applied, but a better match of observations and predictions can be obtained if a most compressive regional horizontal stress trending N70E and exceeding the least compressive stress by 10 MPa is superposed on the thermal stresses. Predicted tensile thermal stresses are as large as 60-123 MPa; this is of the same order of magnitude as plausible fluid pressures, remote tectonic stresses, and lateral pressures associated with the overburden. I conclude that thermal stresses must play an important role in the jointing process. If joints in a pluton characteristically form as a result of thermal stresses during cooling, then the large-scale pattern of joints should be predictable based on a pluton's geometry, its age relative to the

adjacent rock, and a knowledge of the regional stress at the time of intrusion. These findings should be applicable to granitic terranes elsewhere. Post-jointing deformation and fluid flow within a pluton can be controlled by early formed joints, so these findings bear on issues pertinent to mining, petroleum recovery, nuclear waste repository siting, and ground water flow.

Table of Contents

List of Tables

List of Figures

Chapter 1: Introduction

Fractures strongly influence the strength, anisotropy, and fluid flow characteristics of rock masses (National Academy of Sciences, 1996); they also can be used to infer the stress conditions in the Earth (Olson and Pollard, 1989). It is important to account for large-scale fracture networks in evaluating the flow of groundwater and hydrocarbons, and also in siting and designing nuclear waste repositories. With the onset of fracturing, a rock mass obtains a structure which will further control its mechanical and hydrologic behavior. For example, in many places faults nucleate from pre-existing dikes and joints (Segall and Pollard, 1983b; Martel et al., 1988; Lisle, 1989; Martel, 1990; Martel and Peterson, 1991). Understanding the factors controlling the initial fracturing in a rock mass thus has broad practical and academic significance.

The focus here is on the development of joints in granitic rocks. Joints, or opening mode fractures, are the most ubiquitous type of fracture (Pollard and Aydin, 1988). Joints in granites are of interest for two main reasons. First, in many places granitic rocks form the foundation of continents. Deformation along fractures in the "basement rocks" will affect the overlying rocks as well. Second, granitic rocks are among the most homogeneous rocks on scales greater than the grain size, and are therefore in many ways more simple from a mechanical standpoint than layered and foliated rocks. An understanding of joints in a relatively simple rock should form a good basis for helping to understand joints in more complicated rocks.

Joints in granitic rock masses can be caused by either extrinsic stresses (e.g., remote tensile tectonic stresses or stresses associated with erosion of the overburden), or by intrinsic stresses associated with pluton cooling (e.g., fluid pressures, thermal stresses), or by a combination. Joints resulting from tectonic loads could be of any age younger than the host rock, could cut well across the boundaries between plutons, and should form patterns consistent with regional stresses rather than with the pluton geometry. In contrast, joints that originate due to cooling should be tied to factors intrinsic to a pluton, such as its age and geometry. Joints due to cooling should only be slightly younger than the host pluton, and their geometry should reflect the geometry of the pluton.

This work targets the origin of joints in granitic rocks of the Sierra Nevada batholith of California. The origin of these joints has intrigued geologists for more than 100 years (e.g. Becker, 1892). The joints are manifest on a regional scale as prominent topographic features, and they are superbly exposed in outcrops (e.g. Segall and Pollard, 1983a). Bateman and Wahrhaftig (1966, p. 122) considered that prominent joints in Sierran plutons are regional in origin and formed "after the consolidation of the entire batholith" because "they cross boundaries between plutons with little or no deflection." Lockwood and Moore (1979) ascribed the fractures to mid-Cenozoic deformation associated with regional extension in the Basin and Range province. Segall et al. (1990), however, presented radiometric evidence indicating that joints of the Lake Edison Granodiorite formed within a few million years of the emplacement of the host plutons.

This research examines the possibility that most of the plutonic joints are caused by stresses due to the initial cooling of the pluton. This examination focuses on one pluton from the Sierra Nevada, the Lake Edison Granodiorite (Bateman, 1992). This pluton and its neighboring intrusions are well suited for investigating fracture origins because deformation of the granitic rocks there subsequent to the initial fracturing generally is small, and a large body of prior field and laboratory research on the rock and its fractures exists (Lockwood and Lydon, 1975; Segall and Pollard, 1980, 1983a, b; Segall, 1984; Martel et al., 1988; Martel, 1990; Bateman, 1992; Tikoff and Teyssier, 1992; Bürgmann and Pollard, 1994; Christiansen, 1995).

Thermal stresses have long been suspected of causing fracturing in cooling plutons (Balk, 1937; Hulin, 1948). Fracturing of minerals in igneous rocks have been attributed to stresses induced by differential contraction during cooling (Devore, 1969). Nur and Simmons (1970) showed theoretically that small cracks in igneous rocks can nucleate due to thermal stresses, and Wang et al. (1989) demonstrated this experimentally. The common hydrothermal fracture-filling mineral assemblage of epidote and chlorite in granitic rocks of the Sierra Nevada batholith is considered to precipitate during cooling and dewatering of a pluton (Best, 1982).

Quantitative two-dimensional treatments of cooling plutons have been presented by Knapp and Norton (1981) and Gerla (1988). These investigations accounted for effects of tectonic, gravitational, magmatic, and thermal processes on fracture formation in cooling bodies with simple geometries. Knapp and Norton (1981) numerically evaluated stresses for a pluton with a rectangular cross section. Gerla (1988) presented an analytical model for calculating stresses in a cooling cylindrical pluton. However, thermal stresses associated with more complex plutons geometries have not been investigated. The technique presented here to calculate thermal stresses in 2-D is fast and applicable to a broad array of pluton shapes and initial conditions.

I integrate information on the geometry and petrology of the host rock and its fractures, radiometric data, and thermo-elastic modeling results to examine plausible joint-causing stresses. First the geometry and mineralogy of the host pluton and its fractures is discussed, followed by the thermal history of the plutons. Two-dimensional analyses of temperatures and stresses in a cooling elastic plate then are used to quantitatively test whether thermal effects are a plausible mechanism for jointing. Although I focus on plutons from the Sierra Nevada, I expect the findings apply to granitic terranes in general.

Chapter 2: Geometry and Mineralogy of Plutons and Fractures

The Lake Edison Granodiorite is an elongate pluton located between Yosemite and Kings Canyon National Parks. The pluton consists mostly of rather homogeneous, fine- to medium-grained hornblende-biotite granodiorite with abundant sphene (Lockwood and Lydon, 1975). The pluton is slightly more than 50 km long. Its long horizontal axis trends NW, roughly parallel to the Sierra Nevada crest, and it ranges in width from 1.5 km to 4 km. The study area is located about midway between the ends of the pluton (Fig. 1), and lies in the Mount Abbot quadrangle (Lockwood and Lydon, 1975). The pluton has a narrow "waist" near the center of the quadrangle. To the west, the Lake Edison Granodiorite (Kle) is bordered by the older Lamarck Granodiorite (Kl). The Lamarck Granodiorite is intruded by the Mount Givens Granodiorite (Kmg). To the east, the Lake Edison Granodiorite is bordered by the younger Mono Creek Granite (Kmo) of Bateman (1992). The contacts between the Lake Edison Granodiorite and the adjacent plutons dip steeply. The Lake Edison Granodiorite is for the most part weakly foliated, with the foliation also dipping steeply and striking roughly parallel to the pluton boundaries. Along the Rosy Finch shear zone (Tikoff and Teyssier, 1992; Tikoff and Saint Blanquat, 1997), however, the foliation is more pronounced and cuts across the pluton (Fig. 1). The pluton crops out over an elevation range of about 1500 meters, providing a minimum vertical extent for the pluton. Ague and Brimhall (1988) contended that the Sierra Nevada batholith locally had a vertical extent of 30-35 km, so the Lake Edison Granodiorite might have been considerably more than 1.5 km from top to bottom.

Fractures in the Lake Edison Granodiorite dip steeply and strike predominantly ENE to NE. The most prominent ones are reflected in Fig. 1 as photolineament traces. Please note that the mapped photolineaments might not reflect the actual fracture density

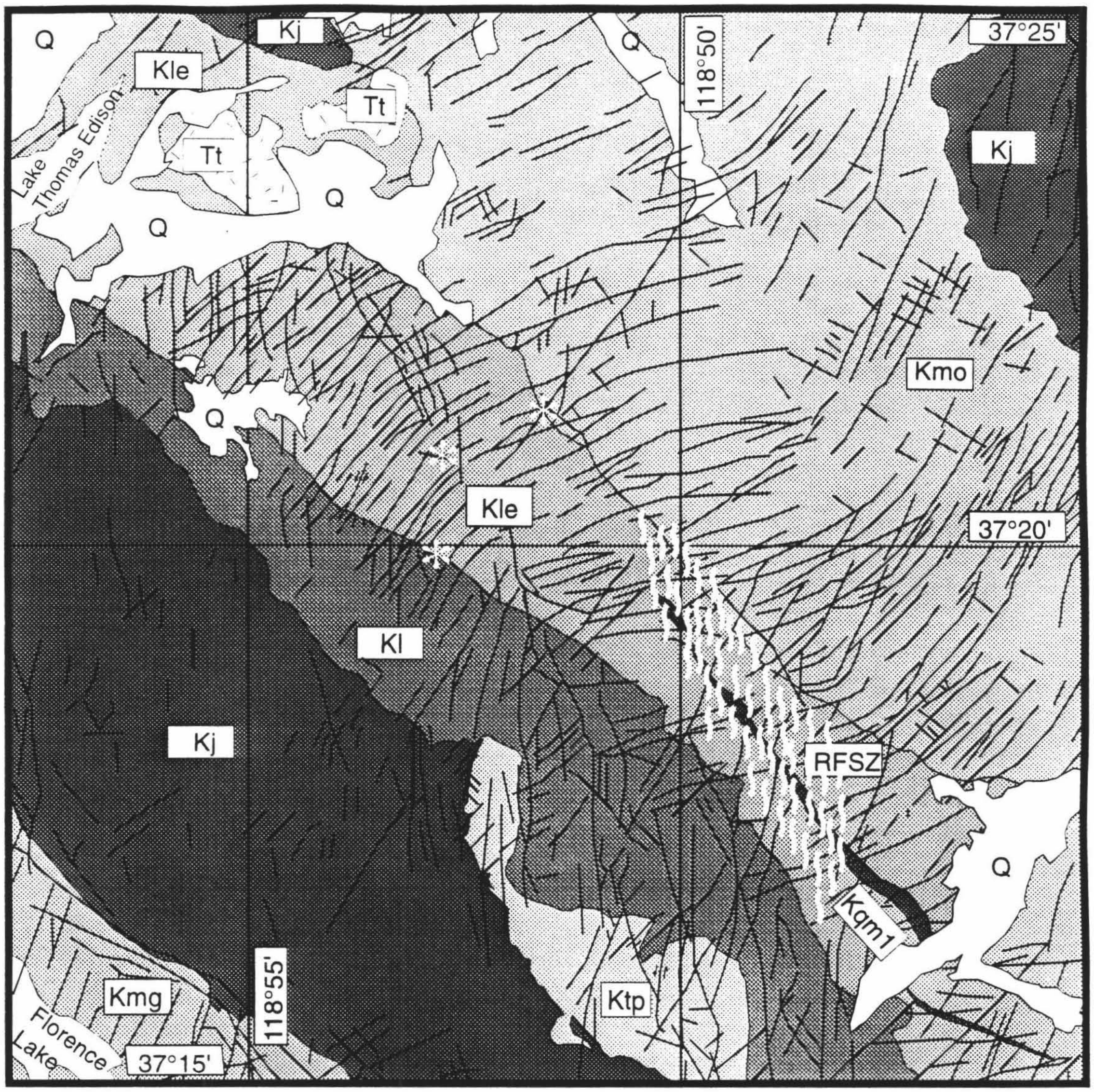

Figure 1. Map showing the generalized geology of a portion of the Mount Abbot quadrangle and prominent fracture systems (modified from Lockwood and Lydon, 1975). The main geologic units shown are, from oldest to youngest, undifferentiated Cretaceous and Jurassic plutons (Kj), the Lamarck Granodiorite (Kl), the Mount Givens Granodiorite (Kmg), the Lake Edison Granodiorite (Kle), the Mono Creek Granite (Kmo), Cretaceous quartz monzonite and granite (Kqm1), Tertiary olivine trachybasalt (Tt), and Quaternary deposits (Q). Sample locations for the radiometric dating are marked by the white asterisks. The locations of both outcrops shown in Fig. 2 coincides with the asterisk at the Kl-Kle contact. RFSZ indicates the Rosy Finch shear zone (Tikoff and Teyssier, 1992).

everywhere within the pluton because Cenozoic deposits cover parts of the intrusion; no photolineaments are shown there. Fractures consist of dikes, parallel joints, small faults, and fault zones (Segall and Pollard, 1983a; Segall, 1984; Martel et al., 1988; Martel, 1990). At the scale of an outcrop the fractures in the Lake Edison Granodiorite and adjacent plutons have straight traces. The longest joint traces and the longest fault zone segments on flat or gently inclined outcrops are about 50 meters long. The longest joint traces on canyon walls appear to extend for a comparable vertical distance. The spacing between fractures ranges from several decimeters to several meters. The joints generally have maximum apertures of no more than a centimeter; commonly the apertures are less than a millimeter. They are filled with a mineral assemblage dominated by undeformed epidote and chlorite, with trace amounts of sericite, muscovite, calcite, and zeolite (Segall and Pollard, 1983a). Based on the spacing of the joints and their apertures, Segall and Pollard (1983a) calculated that the strain accommodated by opening of joints in the nearby Mount Givens Granodiorite is 10^{-4} to 5×10^{-4}. My field inspections indicate that the spacing and apertures of joints there are similar to that in the Lake Edison Granodiorite, and I thus infer that the joint-accommodated strain is comparable.

Figure 2 shows two maps of fracture traces in outcrops along the contact between the Lake Edison Granodiorite and the Lamarck Granodiorite. The inset rose diagrams show the distribution of fracture strikes in those locations. At these outcrops the two plutons can be distinguished based on differences in their color and texture, allowing the location of the contact to be resolved within several centimeters. Markers that are cut by fractures but not laterally offset (e.g., igneous dikes, xenoliths) permit joints to be distinguished from faults. Fractures in both plutons strike at high angles to the contact. However, the fracture spacing is distinctly different on opposing sides of the contact, being less in the Lake Edison Granodiorite. Although most joints that extend into the adjacent intrusion

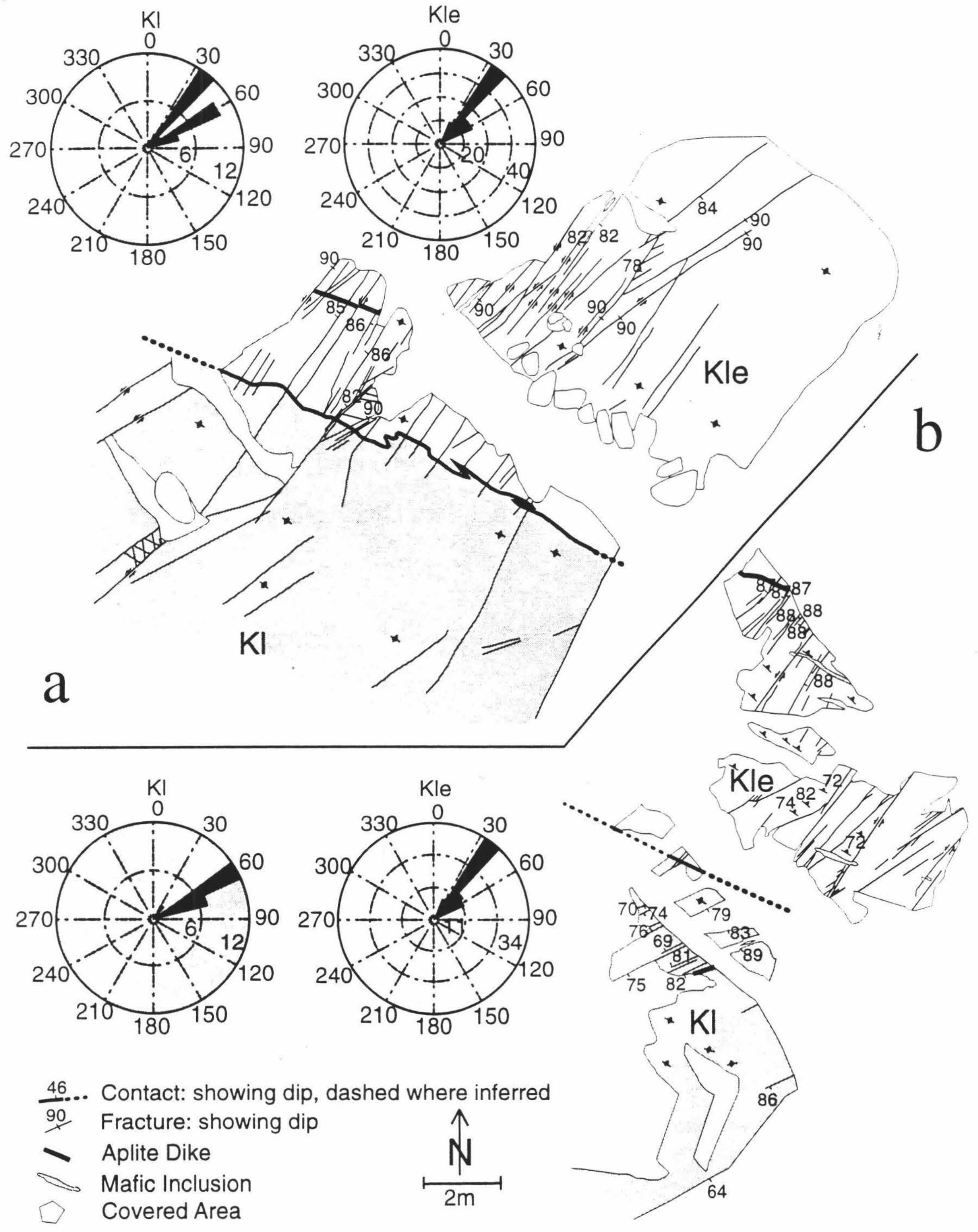

Figure 2. Maps showing two outcrops at the Kl-Kle contact (white asterisk in Fig. 1) and inset rose diagrams. Outcrop **a** lies ca. 100 m northwest of outcrop **b**. Fracture spacing and orientation in both outcrops vary across the contact. Dark and light rose diagrams represent fractures in Kl and Kle, respectively.

terminate within one meter of the contact, some joints do not. The nucleation points of joints that cross the contact can not be established owing to the absence of plumose structure on the rough joint faces. In contrast to the joints, several fault zones near these outcrops do cross the Kle-Kl contact and extend well into both plutons.

The rose diagrams also reflect differences in the fracture patterns. More than twice as many fractures exist in the younger intrusion (Kle). Additionally, the overall strike of the fractures differs on opposing sides of the contact. Whereas joints in the Lake Edison Granodiorite strike roughly N40E, joints in the Lamarck Granodiorite exhibit strikes closer to N60E. In the rose diagrams, a fracture that extends into both plutons is accounted for twice, once for each pluton. The suite of fractures that extends for only a short distance into the Lamarck Granodiorite in outcrop **a** leads to the strong contribution of fractures striking approximately N40E.

At the scale of the pluton the fractures are displayed as vegetated lineaments and grooves in the topography (Fig. 1). The average strike of the fractures within the Lake Edison Granodiorite is roughly at right angles to the long axis of the pluton. Neither the fracture traces nor the pluton contacts are straight at the scale of the pluton. The fracture traces northwest of the "waist" of the pluton near the center of Fig. 1 are concave to the south, whereas the fracture traces southeast of the "waist" are concave to the north. The fractures thus maintain a roughly orthogonal relationship to the pluton boundary even where the boundary orientation changes. A similar geometric relationship between photolineaments and pluton boundaries exists in several other plutons throughout the Sierra Nevada, for example the Granodiorite of Cartridge Pass in the Sierra Nevada (Bergbauer et al., 1998), and the southwest margin of the Mono Creek Granite (Fig. 1).

Chapter 3: Structural History of the Lake Edison Granodiorite

The oldest structure in the pluton is its weak foliation, interpreted to be synmagmatic and resulting from magma flow during crystallization (Bateman, 1992; Christiansen, 1995). Two sets of igneous dikes cut the foliation. One well defined set strikes approximately N20W. The second, younger set contains dikes with a broad range of strikes (Christiansen, 1995). These dikes are in turn cut and offset by ENE-striking joints and faults. Segall and Pollard (1983b) and Martel et al. (1988) concluded that the faults and fault zones evolved from the joints. They inferred that a change in principal stress orientation caused some joints to subsequently slip left-laterally. Fault zones then developed by the linkage of smaller faults. Eventually, some fault zones grew across pluton boundaries and accommodated slip as much as several tens of meters (Lockwood and Lydon, 1975; Martel, 1990). Because the faults and fault zones formed from the preexisting joints, the large-scale orientations of all these younger structures, as represented by the photolineaments, reflect the orientation of the original joints.

Geometric factors suggest that the pluton was not emplaced under isotropic regional stresses. The long horizontal axis of the Lake Edison Granodiorite trends NW, and several steep, dike-like bodies of late Cretaceous age within the pluton strike NW (Kqm1 in Figs. 1 and 3), suggesting that the least compressive horizontal stress was oriented NE during their emplacement (Fig. 3a). These orientations are compatible with plate tectonic reconstructions. The least compressive regional horizontal stress a couple of hundred kilometers inland from a subduction zone commonly parallels the displacement direction of the subducted plate (Nakamura and Uyeda, 1980), and during late Cretaceous time the Farallon plate was being subducted to the northeast beneath the North American plate (Engebretson et al., 1985).

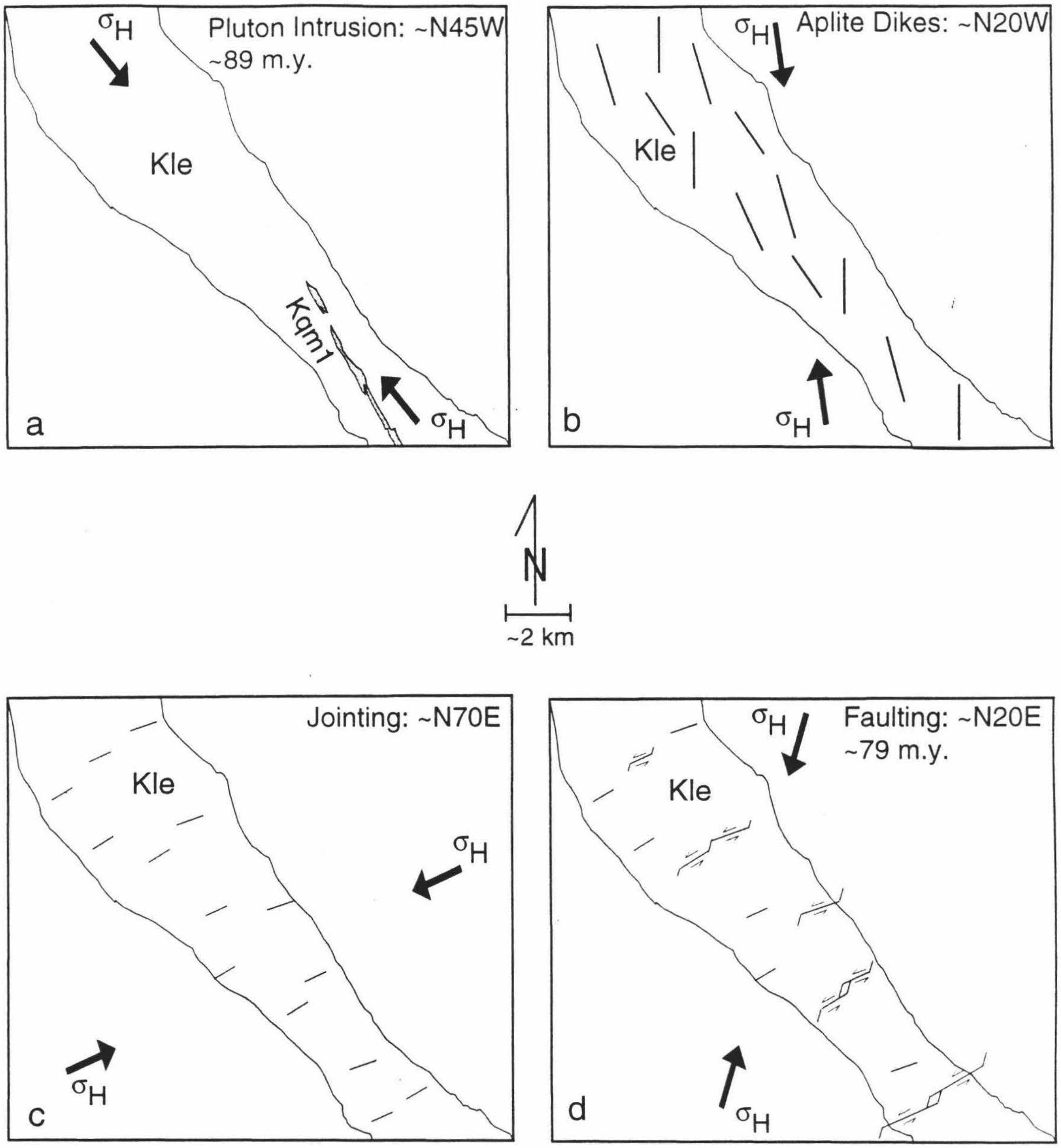

Figure 3. Most compressive horizontal stress directions (σ_H) in the Lake Edison Granodiorite (Kle) inferred from field observations (modified from Christiansen, 1995), when (a) the pluton intruded, (b) the first set of igneous dikes intruded, (c) the joints opened, and (d) the faulting occurred.

Based on the work of Christiansen (1995), three major changes in principal stress orientation can be distinguished in the pluton after its emplacement (Fig. 3b-d). The first generation of dikes strikes approximately N20W. The direction of the most compressive horizontal stress during their formation must have paralleled their strike. Owing to the wide range of strike directions for dikes in the second set, a single principal stress orientation can not be inferred from those dikes (not shown in Fig. 3). When the ENE-striking joints opened, the most compressive horizontal stress was oriented N65E-N75E. Left-lateral faults and fault zones then developed with the most compressive horizontal stress oriented NNE. This stress orientation is indicated by the orientation of secondary fractures at the ends of strike-slip faults. These fractures commonly strike 15-30° counterclockwise from the faults (Segall and Pollard, 1983b; Martel et al., 1988).

Ductile deformation along faults in the Lake Edison Granodiorite becomes more pronounced on faults that near the younger Mono Creek Granite (Bürgmann and Pollard, 1994). This suggests that faulting in the Lake Edison Granodiorite is in some way associated with the intrusion of the younger granite. Because jointing in the Lake Edison Granodiorite preceded faulting, the jointing would appear to precede the intrusion of the Mono Creek Granite. Based on these field observations it appears that the jointing occurred during the period of late Cretaceous plutonism.

Chapter 4: Radiometric Ages

The ^{40}Ar/^{39}Ar dating technique can provide quantitative constraints on the thermal histories of granitic rocks. The dates obtained from this technique can be related to closure temperatures, temperatures below which the diffusion of ^{40}Ar into and out of a mineral ceases. Published closure temperatures are 330± 50°C for biotite (Grove and Harrison, 1996), and 535± 45°C for hornblende (Harrison, 1981). Radiometric dating results for biotites and hornblendes from five samples collected along a traverse across the Lake Edison Granodiorite and the neighboring plutons (white asterisks in Fig. 1) are summarized in Table 1. Samples were taken on either side of the contacts between plutons at two locations. Owing to potassium contamination of the lower temperature gas released in the hornblendes and minor age gradients in the biotites (personal conversation, Marty Grove), the argon release pattern of the samples did not produce clear plateaus. Therefore, the radiometric total gas ages for these samples are used here and listed in Table 1.

Table 1. Summary of ^{40}Ar/^{39}Ar total gas ages for collected samples used in Fig. 4

Sample	Mineral	Total Gas Age (m.y.)	Standard Deviation (m.y.)
KLEF3H	Hornblende	86.5	0.8
KLEF3B	Biotite	83.0	0.1
KLE4H	Hornblende	88.7	0.4
KLE4B	Biotite	80.7	0.2
KLEP5H	Hornblende	85.3	0.7
KLEP5B	Biotite	80.6	0.2
KL2H	Hornblende	90.3	0.7
KL2B	Biotite	80.0	0.2
KMR2H	Hornblende	84.5	0.6
KMR2B	Biotite	81.1	0.1

Figure 4 depicts the newly obtained dates in addition to K-Ar and $^{40}Ar/^{39}Ar$-dates on Kle-fault zone muscovites (Segall et al. 1990), and K-Ar dates for biotites and hornblendes from the Mount Givens Granodiorite (Kistler et al., 1965). Heavy crosses and solid rectangles represent dates obtained in this study from hornblende and biotite, respectively. Gray rectangles indicate biotite dates presented by Christiansen (1995). Gray squares depict muscovite dates from Kle-fault zones (Segall et al., 1990). Thin crosses and white rectangles depict K-Ar dates (Kistler et al., 1965) on hornblendes and biotites, respectively. Figure 4 suggests that the Lamarck Granodiorite cooled through the hornblende closure temperature at around 91 m.y., before the Mount Givens Granodiorite (~89 m.y.), the Lake Edison Granodiorite (~88 m.y.) and the Mono Creek Granite (~85 m.y.). The indicated radiometric age relationships are consistent with cross cutting relationships observed in the field (Bateman, 1992). Interestingly, the Mount Givens Granodiorite appears to have cooled through the biotite closure temperature of 330°C before the other three plutons (Kl, Kle, Kmo), including the apparently older Lamarck Granodiorite. These three plutons appear to have cooled together through the *biotite* closure temperature during the interval from 84 to 80 m.y. This could be due, at least partially, to reheating of the two younger plutons (Kle, Kl) during intrusion of the extensive Mono Creek Granite. Moreover, the scatter of the biotite dates within each pluton suggests that the ambient temperature of the area was below but close to the biotite closure temperature, so that local temperature disturbances were able to delay the cooling of parts of the intrusion through the biotite closure. Radiometric dating of muscovite obtained from secondary fractures within two fault zones in the Lake Edison Granodiorite yielded a mean age of 79 m.y. (Segall et al., 1990), very close to the radiometric ages of biotite in the host rock. The radiometric constraints obtained from these fault zones also represent the youngest possible formation age for the joints and ties the jointing to the period of late Cretaceous plutonism in the Sierra Nevada.

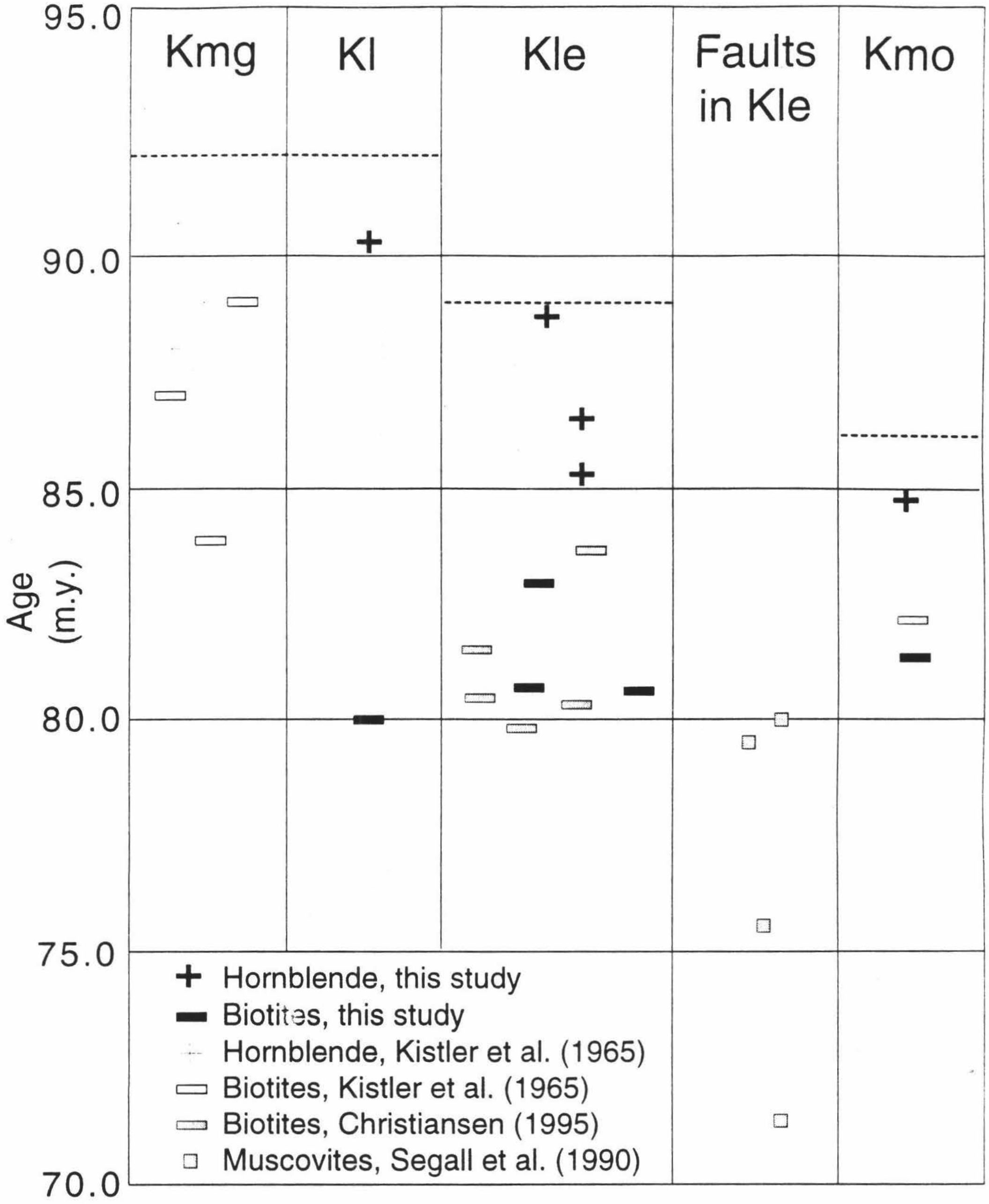

Figure 4. Ar-diffusion ages of fault-zone muscovites compared with ages of host rock (Kle) and adjacent plutons from samples taken in the study area (modified from Segall et al., 1990). Dotted lines indicate assumed intrusion ages for the thermo-mechanical modeling. Joints in Kle are interpreted to have formed between 87 m.y. and 86 m.y.

Chapter 5: Pressure and Temperature Conditions

I now discuss the pressures and temperatures at which the Lake Edison Granodiorite might have been emplaced. This information will be used subsequently in the thermo-mechanical modeling.

Solidus and liquidus temperatures of the granodiorites can be inferred by geochemical means. Geobarometric studies in the central Sierra Nevada indicate confining pressures during pluton emplacement between 100 and 390 MPa and emplacement depths between 3.5 and 14 km (Bateman, 1992; Ague, 1997). Experimental studies by Robertson and Wyllie (1971) and Piwinskii (1968) show that solidus temperatures in granodiorites are unaffected by magma water content in the range from approximately 0.5% by weight (water deficient) to 15% by weight (water excess). Both studies describe solidus temperatures ranging from 750°C at 100 MPa to 680°C at 350 MPa confining pressure. Liquidus temperatures, however, depend on the water content of the magma under water deficient conditions (below 6.5% by weight). Lowest liquidus temperatures of 980°C are obtained for granodiorites with water contents above 6.5% by weight and confining pressures of 100 MPa, and highest liquidus temperatures of more than 1100°C are measured if water is absent for confining pressures 300 MPa.

Once cooled through the solidus temperature, a pluton is certainly able to sustain tensile stresses. However, as the pluton approaches the solidus, it cools through a temperature at which the crystal-liquid admixture constitutes a crystal-bonded aggregate. Such aggregates can transmit seismic shear waves (Sinton et al., 1992). Referred to as the critical crystallinity (Marsh, 1989; Bergantz, 1990), at this point the viscosity increases exponentially. When magmas reach this temperature, their ascent in the crust is likely to halt. According to McBirney (1984) this point is reached over a crystallinity interval of 40-70%, decreasing with increasing silica content. Based on Piwinskii's (1968) experiments under water saturated conditions, 40 to 70% crystallinity in a granodiorite magma is reached at temperatures between 740 and 700°C at 300 MPa and 840 and 830°C at 100 MPa confining pressure. I assume that cooling through 800°C enables the pluton to sustain tensile stresses.

The mineral assemblage in the joints, primarily of undeformed epidote and chlorite with minor amounts of calcite, muscovite, sericite, and zeolites (Segall and Pollard, 1983a), is consistent with the minerals having precipitated under lower greenschist pressure-temperature conditions. The temperature for the greenschist facies at confining pressures of 200 to 500 MPa ranges from 300 to 570°C (Hyndman, 1985, p. 588). According to Best (1982), Sierran magmas contained enough water for the joint fillings to precipitate, but apparently not enough water for large amounts of the granite to hydrothermally react and to form epidote and chlorite. Laboratory results indicate that fluid pressures in magmas can reach overpressures in excess of 500 MPa (Burnham, 1979).

Chapter 6: Constraints of Potential Mechanism for Jointing

A mechanism suggested for the formation of the ENE-striking joints in the Lake Edison Granodiorite should be consistent with the age, geochemistry, and geometry of the joints and the pluton. Whereas the faults formed from preexisting joints, the dates obtained from the fault zones ties joint formation to the initial cooling of the pluton. Moreover, the joints must have opened during the age window represented by the Kle-hornblende and biotite dates because the joint fillings precipitated under greenschist-facies conditions with temperatures between 300°C and 550°C. This allows us to constrain the jointing age between approximately 87 and 81 m.y (Fig. 4). Additionally, the photolineament geometry at the Kle-Kmo contact of the Lake Edison Granodiorite shows that the joints approach the contact at high angles. This "feeling" of the contact indicates that jointing in the Lake Edison Granodiorite occurred before the intrusion of the younger Mono Creek Granite (86 m.y.): given that granodiorite exists on both sides of the contact, I expect the contact to be mechanically invisible once the plutons are cooled. This suggests that the joints formed before approximately 86 m.y. Integrating all the information suggests that the Kle-joints opened between 87 m.y. and 86 m.y.

Although the radiometric data tie the jointing to the time when the pluton was cooling, they do not prohibit fracturing as a result of regional effects. Geometric data, however, strongly support a cooling origin. Columnar joints in a lava flow are well known to form perpendicular to its boundaries. Likewise, the overall orientation of the Kle-fractures at nearly right angles to the pluton boundaries suggests a cooling mechanism. Perhaps more significantly, the orientation of the joints appears to "track" the orientation of the pluton boundary; as the boundary orientation changes so does the orientation of the joints. This pattern is consistent with a cooling origin but is difficult to reconcile with a regional mechanism.

I now turn to the stresses during joint formation. The nearly vertical dip of the joints and the relative displacement across them indicate that the effective most tensile stress at the time of jointing was essentially horizontal. In order for a joint to open, the extrinsic ($T_{tectonic}$) and intrinsic ($T_{thermal}$) tensile stresses across the plane of a joint together must exceed the horizontal component of the compressive lithostatic pressure (P_{hlith}) minus the fluid pressure (P_{fluid}):

$$T_{tectonic} + T_{thermal} > P_{hlith} - P_{fluid}. \qquad (1)$$

This modifies the condition for opening mode fracture of Secor (1965) to account for thermal stresses. I define the driving stress ($\sigma_{driving}$) as:

$$\sigma_{driving} = T_{tectonic} + T_{thermal} + P_{fluid} - P_{hlith}. \qquad (2)$$

The driving stress must be tensile for the joints to open. Segall and Pollard (1983a) calculated a driving stress of 1 to 40 MPa to initiate joint growth in the Mount Givens Granodiorite. According to Olson and Pollard (1989), joints will develop straight traces if the differential stress in the horizontal plane during joint propagation exceeds twice the driving stress. The differential stress at a point is the difference between the most (σ_H) and least compressive horizontal stress (σ_h) and equals twice the maximum shear stress:

$$\sigma_H - \sigma_h = 2\tau_{max}. \qquad (3)$$

The occurrence of joints with straight traces thus relates the maximum shear stress (τ_{max}) to the driving stress:

$$\tau_{\max} \geq \sigma_{driving}. \qquad (4)$$

The joint traces in the Lake Edison Granodiorite are generally straight in outcrops, so the maximum shear stress acting in the intrusion at the time of joint formation would therefore be no less than 1 to 40 MPa (i.e., the driving stress of Segall and Pollard, 1983a).

I now turn to the sources of stress on the right hand side of equation (2). Bateman (1992) and Ague (1997) inferred vertical lithostatic pressures P_{vlith} for Sierran plutons in the range from 100 to 390 MPa, so a maximum bound for P_{hlith} is 390 MPa. A minimum value for P_{vlith} is obtained by assuming a laterally confined Earth, where the horizontal component of the lithostatic pressure is defined as:

$$P_{hlith} = P_{vlith} \cdot \frac{\nu}{1-\nu}. \qquad (5)$$

Using a Poisson's ratio (ν) of 0.25 and formula (5), the associated horizontal component of the lithostatic pressure lies between 30 and 130 MPa. Possible pressures in the horizontal plane due to the effect of overburden therefore range from 30 to 390 MPa. Plausible fluid pressures range from 0 to 500 MPa (Burnham, 1979). Depending on the magnitudes, the difference of these pressures either helps drive or prevent fracturing. However, these pressures will not affect the *orientation* of the most tensile horizontal stress, as they act equally in all directions of the plane. The stresses that govern the overall *orientation* of the most le horizontal stress are regional tectonic loads and thermal stresses.

Chapter 7: Thermo-Mechanical Model

A two-dimensional thermo-elastic numerical analysis (Appendix A) was conducted to test the mechanical viability of a cooling mechanism for jointing in the portion of the Lake Edison Granodiorite shown in Fig. 1. The first part of the analysis was to calculate temperature distributions by numerically solving the diffusion equation for two-dimensional conductive cooling (Carslaw and Jaeger, 1959). The second part of the analysis entailed calculating thermo-elastic stress magnitudes and orientations from the temperatures. Thermal stresses in the modeling domain were assumed to be zero when the Lake Edison Granodiorite was emplaced, and the far-field (i.e., tectonic) stresses were also set to zero. Pluton emplacement was assumed to be rapid relative to the time required for substantial cooling. Given the geometry of the Lake Edison Granodiorite and its fractures, the depth at which the plutons cooled, and the likely vertical extent of the plutons, a 2-D plane analysis was deemed appropriate. The thermo-elastic analyses do not account for stress redistribution associated with fracturing. Appendix B derives the formulas used in the thermo-elastic numerical analysis

A pluton in the model is treated as a hot region in an elastic plate of homogeneous, isotropic, continuous material. At time $t=t_o$ heat starts to flow from the solid pluton into the host rock, and thermal stresses build over time. The first step is to solve the heat diffusion equation in 2-D

$$\kappa \cdot \nabla^2 T = \frac{\partial T}{\partial t}, \tag{6}$$

to determine the temperature distributions T over time t; κ is the thermal diffusivity. Since I am trying to account for the initial fracturing of a newly emplaced pluton, heat transfer inside an unfractured pluton would be dominated by conduction. I solve the governing equations by transforming spatial distributions (e.g., temperatures or displacement potentials) into the spatial frequency domain using 2-D fast Fourier transforms Φ and their inverse Φ^{-1} (Bracewell, 1978). To do this, I first assign wavenumbers in two dimensions, k_{x1} and k_{x2}, to the modeling domain. To find the temperature distributions, the decay of the initial temperature distribution is then calculated in the frequency domain. Transforming this back into the spatial domain gives the temperature distribution T for a cooling time t:

$$T(x_1,x_2,t)=\phi^{-1}\{e^{-\kappa(k_{x1}^2+k_{x2}^2)t}\cdot\phi[T(x_1,x_2,0)]\}. \qquad (7)$$

The second step involves calculating thermoelastic stresses from the temperatures. Plane stress thermoelastic displacement potentials Ψ were used in these calculations (Timoshenko and Goodier, 1970). For the cases considered here, the potentials assume the following form:

$$\psi=\frac{1+\nu}{1-\nu}\alpha\kappa\int_0^t T\,dt, \qquad (8)$$

with

$$u_i = \frac{\partial \psi}{\partial x_i}, \tag{9}$$

where α is the coefficient of thermal expansion, ν is Poisson's ratio, and u_i is the displacement for i=1 or 2. Timoshenko and Goodier considered relaxation of thermal stresses, whereas I examine thermal stress buildup, so equation (7) lacks a leading minus sign on the right side and has different limits of integration than expression (o) of Timoshenko and Goodier (1970, p. 480). The time integral in (8) can be calculated analytically using fast Fourier transforms:

$$\int_0^t T dt = \left[\phi^{-1} \left\{ \frac{e^{-k\left(k_{x1}^2 + k_{x2}^2\right)t}}{-k\left(k_{x1}^2 + k_{x2}^2\right)} \phi\left[T(x_1, x_2, 0)\right] \right\} \right]_0^t . \tag{10}$$

Stresses are obtained from Hooke's law for thermoelastic materials (Timoshenko and Goodier, 1970). To evaluate the thermal stresses, the first partial derivatives of u_i, and hence the second partial derivatives of ψ, with respect to x_1 and x_2 must be calculated. In Fourier space the derivatives are evaluated using

$$\frac{\partial^2 y}{\partial x_i \partial x_j} = \phi^{-1}\left[-k_{xi} k_{xj} \cdot \phi(y)\right] \qquad \text{for i, j= 1 or 2.} \tag{11}$$

In these calculations Poisson's ratio ν was set to 0.25 (Carmichael, 1989), Young's modulus E to 3×10^4 MPa, and the coefficient of thermal expansion α to 8×10^{-6} C^{-1}

(Skinner, 1966). Pluton intrusions are simulated by assigning intrusion temperatures of 800°C to the grid points that coincide with the pluton as shown on the geologic map (Fig. 1). This intrusion temperature is 100K less than the intrusion temperature used in similar calculations on hydrous tonalite magmas by Knapp and Norton (1981). The ambient temperature field was set to 230°C. This is below the biotite closure temperature of 330°C and, considering a geothermal gradient of 28°C/km, simulates the ambient temperature at a depth of eight kilometers. A series of trials showed that this combination of intrusion and ambient temperature in conjunction with a thermal diffusivity κ of $2.45e^{-6}$ m^2/s yields cooling curves that agree well with the temperature-time conditions established above for the plutons by their hornblende and biotite ages. The thermal diffusivity is twice the value given by Carslaw and Jaeger (1959) for unfractured granite, and this might indicate some cooling in the nearby country rock occurred not only by conduction, but also by convection.

Boundary conditions for the thermo-elastic analyses are defined by the periodicity of the fast Fourier transforms (FFT) used to solve the necessary equations. The FFT-based spectral code assumes the modeling domain is periodic in the plane of the analysis. Boundary effects with this method can be minimized by placing the area of interest in the center of a modeling domain large enough so that very little heat reaches the boundaries. However, geologic considerations allow for a smaller modeling domain to be used by invoking no-heat-flow boundary conditions. No-heat-flow boundary conditions were simulated by the method of images (Fig. 5) and assigned to the NW, SW, and SE boundaries of the modeling domain. The no-flow boundary conditions at the NW and SE boundaries are reasonable given the pluton's extent in either direction along its trend. Resulting errors at the study area introduced by this simplification are small in magnitude as the study area is located roughly half way between the northern and southern ends of

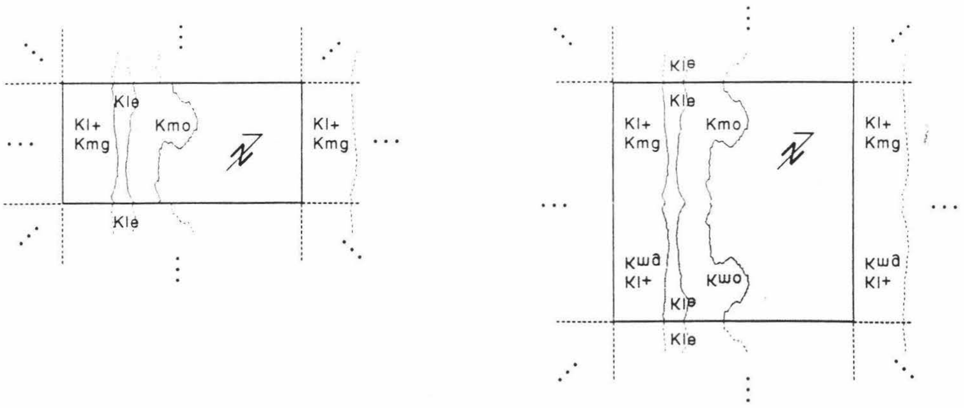

a: Due to the periodicity of the modeling domain (rectangle with solid border), heat can flow across all domain boundaries (solid lines).

b: Image modeling domain (rectangle with solid border) to enforce now-flow condition at SE-boundary. Due to the periodicity of the domain, no-flow conditions thus exist across all horizontal axes of symmetry.

c: Image "new" modeling domain (rectangle with solid border in b) to enforce now-flow condition at NW-boundary. Due to the periodicity of the domain, no-flow conditions thus exist across all horizontal and vertical axes of symmetry.

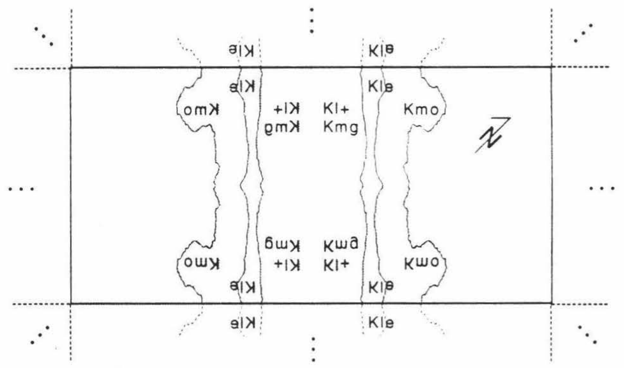

Figure 5. Boundary conditions for the fast Fourier transform-based code. No-heat-flow boundary conditions are modeled using the "method of images". (a) The original modeling domain, (b) the modeling domain after imaging once, and (c) after imaging twice. The three dots symbolize the infinite repetition of the modeling domain in space. NE-extension of the modeling domain is not shown in scale.

the modeling domain. A no-flow boundary condition at the SW margin was assigned considering the size of the two almost concurrent plutons to the west of the area of interest (Kmg and Kl) which are modeled as one single pluton for simplicity. The size of the two plutons together would have resulted in a large modeling domain in order to prevent heat from reaching the domain boundaries. Therefore, half of the surface area of the two combined plutons was used in the model, with a no-flow boundary located roughly along a plane that halves the combined plutons. The NE boundary, however, was chosen to be sufficient distant from the modeled portion of the pluton so that very little heat reached the boundary. After setting up the modeling domain (Fig. 5a), it was imaged once in order to enforce a no-heat-flow condition at the SE boundary (Fig. 5b). Further imaging (Fig. 5c) resulted in a no-flow condition at the SW boundary. Because of the periodicity of the modeling domain, no-heat-flow conditions were thus enforced at all boundaries.

This fast Fourier transform-based method has some significant advantages over finite difference or finite element techniques. For example, the spectral code does not have to step through time to calculate the temperature distribution. This reduces the computation time significantly and allows a variety of geometries and initial conditions to be tested. Additionally, there is no error introduced in the time integration of (10) because it is analytical.

Chapter 8: Model Results for Hypothetical Plutons of Different Geometries

The results presented in this chapter focus on the effects of pluton geometry on magnitude and orientation of thermally induced principle stresses in both the host rock and the cooling intrusion. The cooling times at which the thermal stresses are shown were chosen to highlight key effects. The results for a few relatively simple plan view geometries (Figs. 6-8) are displayed: a circle, a rectangle, and two hourglass forms. Variation of initial conditions and elastic constants also have a significant influence on the results and are reviewed briefly in the discussion. The figures illustrate the intrusion and adjacent host rock. They do not show the entire model domain. The contours represent the most tensile stress, which is considered positive. The tick marks are stress trajectories oriented perpendicular to the direction of the most tensile stress. They indicate the potential propagation direction of a mode I fracture (joint).

Circle: Figure 6 shows the results for a cooling circular pluton. Inside the pluton trajectories perpendicular to the most tensile stress trend radially from the center of the intrusion early in the cooling history (Fig. 6a). However, as time progresses the state of stress in the intrusion approaches hydrostatic (Fig. 6b) with the most tensile stress magnitudes becoming as large as 80 MPa. Depending on the stress required for fracturing, joints could either form early in the cooling history and strike radially from the center, or form later and display a wide range of strikes. In contrast, outside the intrusion the most tensile stress acts radially, reaching magnitudes as large as 50+ MPa. Joints that open there would parallel the pluton contact.

Rectangle: Results for a cooling rectangular pluton are shown in Fig. 7. Tensile stresses reach maximum values of 90+ MPa in the pluton and 50+ MPa in the host rock.

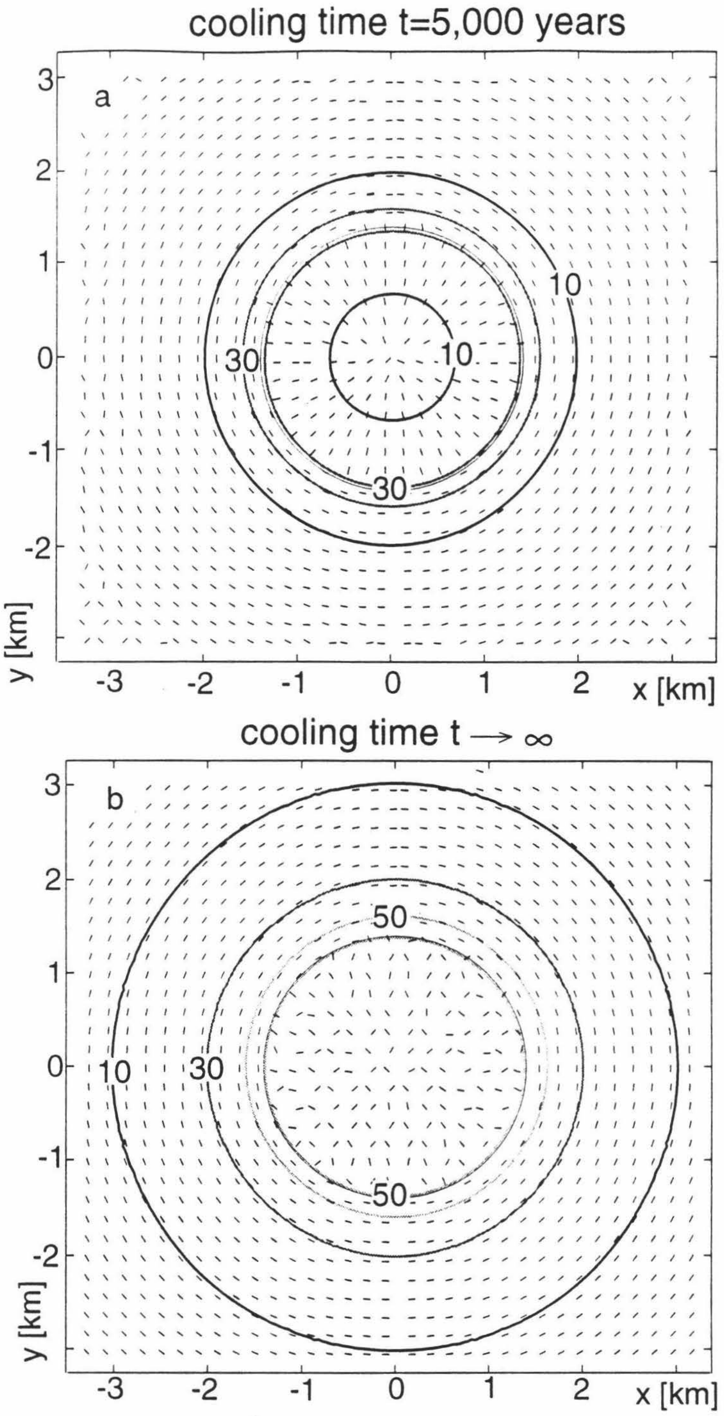

Figure 6. Thermal stress development in host rock and pluton for a circular intrusion after 5,000 years (a) and infinite cooling (b). Contours show most tensile thermal stress magnitudes in MPa. Ticks are perpendicular to the direction of the most tensile thermal stress.

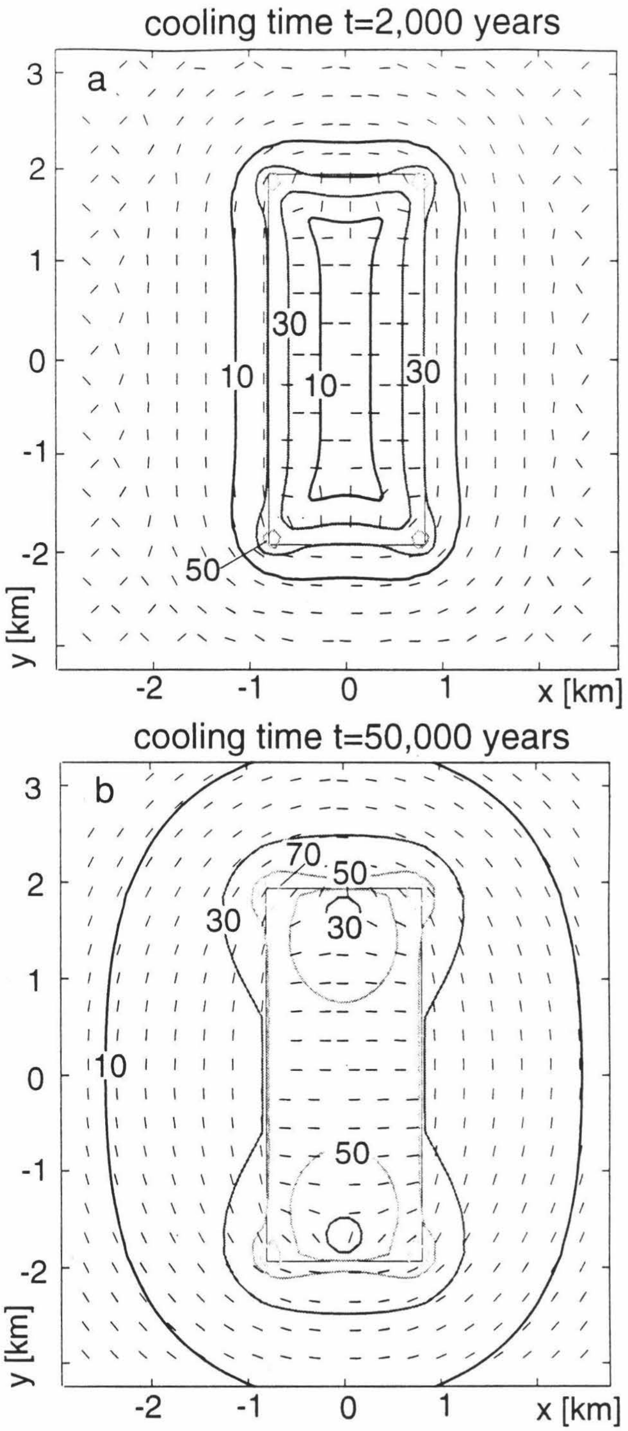

Figure 7. Thermal stress development in host rock and pluton for a rectangular intrusion after 2,000 years (a) and 50,000 years (b) of cooling. Contours show most tensile thermal stress magnitudes in MPa. Ticks are perpendicular to the direction of the most tensile thermal stress.

Thermal stresses in the cooling pluton show maximum values at the corners. In the host rock stress trajectories parallel the intrusion at all times.

Stress trajectories inside the cooling pluton exhibit a more complicated pattern. Early in the cooling history (Fig. 7a) they trend perpendicular to the perimeter. However, as cooling time progresses (Fig. 7b), stress trajectories change orientation to become more perpendicular to the long axis of the rectangle. This sets up the possibility that multiple sets of joints could develop in the ends of an elongate pluton. This could have significant implications regarding fluid flow and subsequent mechanical behavior in these areas.

Hourglass: For the hourglass plutons (Fig. 8) I focus the discussion on the influence of the hourglass shape rather than on the temporal development of thermal stresses build-up. Figure 8 depicts two hourglass forms with the same height but with different curvature. Both simulations are for 50,000 years. Inside both intrusions the stress distributions and magnitudes (30-100+ MPa) are comparable. In both cases stress trajectories inside the intrusion trend perpendicular to the pluton perimeter, and stress magnitudes reach values of 50+ MPa.

However, outside the pluton the stress trajectory patterns differ significantly. For the case of the slim intrusion (Fig. 8b), stress trajectories parallel the intrusion. Outside the waist of the thicker intrusion (Fig. 8a), stress trajectories are perpendicular to the pluton, a change of 90° compared to the slim intrusion. If a fracture were to nucleate in an hourglass-shaped intrusion, it would be far more likely to propagate straight across the contact into the host rock for the intrusion with the greater curvature.

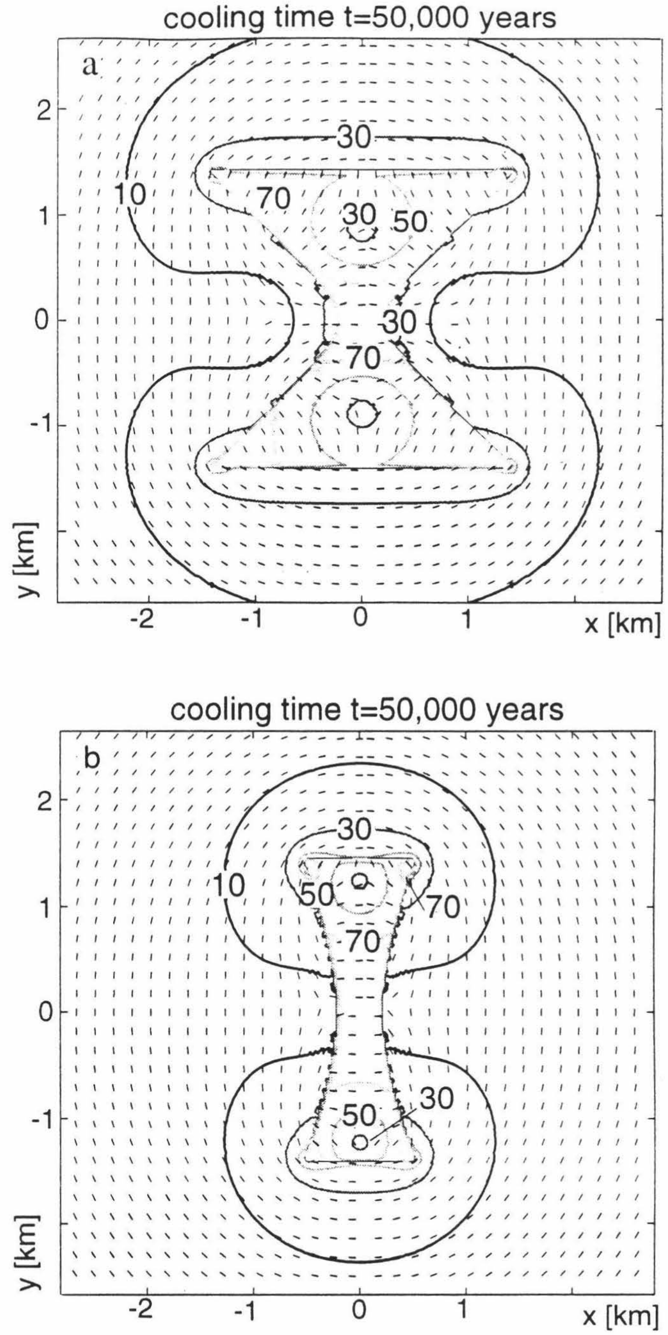

Figure 8. Effects of different geometry for plutons with a "waist" after 50,000 years of cooling for (a) a broad pluton, and (b) a narrow pluton. Contours show most tensile thermal stress magnitudes in MPa. Ticks are perpendicular to the direction of the most tensile thermal stress.

Chapter 9: Model Results for the Lake Edison Granodiorite

The radiometric dates provide constraints on the initial conditions (e.g., temperature distribution at the time of intrusion) for modeling the cooling and stress evolution of the Lake Edison Granodiorite. I model the Mount Givens Granodiorite and the Lamarck Granodiorite intruding simultaneously at 92 m.y. with a temperature of 800°C. The calculations indicate that by about 91 m.y. the Lamarck Granodiorite cools through the hornblende temperature, consistent with the radiometric data. After 3 m.y. of cooling (at 89 m.y.), the intrusion of the Lake Edison Granodiorite is simulated by assigning a temperature of 800°C to the region of the pluton. The plutons are then allowed to cool for another 3 m.y. before the intrusion of the Mono Creek Granite at 86 m.y. Calculated cooling temperatures within the Lake Edison Granodiorite are consistent with the radiometric ages of Fig. 4. Intrusion ages given by Tikoff and Saint Blanquat (1997) for the Lamarck Granodiorite, the Lake Edison Granodiorite, and the Mono Creek Granite are consistent with intrusion ages used here.

Figure 9 (a-c) depicts the modeled thermal stresses in the Lake Edison Granodiorite before the intrusion of the Mono Creek Granite at 86 m.y. Contours in Fig. 9a show the magnitudes of the most tensile horizontal thermal stress. Ticks in Fig. 9b indicate the direction of the most horizontal compressive stress. If a joint were to form it would propagate in the direction of the most compressive horizontal stress. Thermal stresses, assumed to be zero before the intrusion of the Lake Edison Granodiorite, reach maximum values where the pluton has cooled the most and where it is the thinnest. Within the pluton the most tensile thermal stresses are subparallel to the long axis of the pluton and range in magnitude from 60 MPa to 123 MPa (Fig. 9a, b). The calculated stresses are of

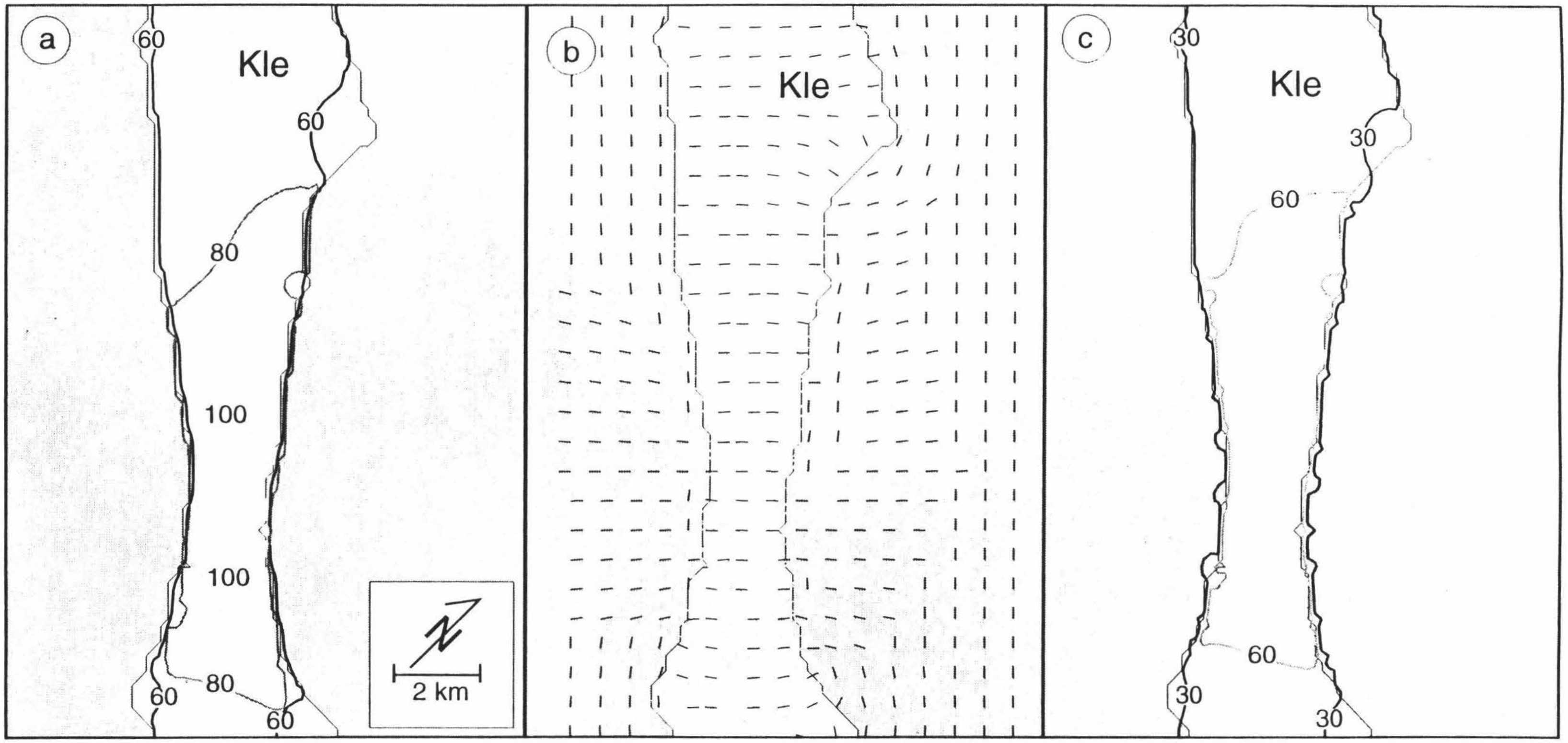

Figure 9. Calculated thermal stresses for the Lake Edison Granodiorite (Kle) at 86 m.y. (a) Magnitudes of the most tensile horizontal thermal stress. (b) Trajectories of the most compressive horizontal thermal stress (heavy ticks) and Kle-photolineaments from Fig. 1 (gray lines) for comparison. (c) Magnitudes of the maximum horizontal thermal shear stress. Stress magnitudes are in MPa. Stress trajectories in the shaded area show the directions of the horizontal most compressive stress in the host rock due to the cooling of Kle, and are not supposed to match the photolineament pattern there. No photolineaments are shown at locations where Kle is covered by younger deposits (see Fig. 1 for comparison).

the same order of magnitude as plausible fluid pressures and pressures due to overburden, and therefore must be an important contribution to the jointing process.

The overall orientations of the predicted most compressive thermal stress in the pluton (ticks in Fig. 9b) compare favorably to the photolineaments (gray lines in Fig. 9b), especially in the northwest half of the study area. Not only do the orientations of the most compressive stresses change across the pluton to approach the contacts at high angles, they also exhibit the same concavity across the pluton as the photolineaments. However, where two sets of photolineaments exist (i.e., in the southeast half of Fig. 9) the modeled stress trajectories approximately bisect the acute angles formed by the photolineaments.

Figure 9c depicts the magnitude of the maximum shear stress in the intrusion due to cooling. Maximum shear stress magnitudes within the pluton generally range from 30 to 60 MPa, but reach peak values of 102 MPa. This is compatible with the driving stress magnitudes of Segall and Pollard (1983a). Joint traces can be expected to be straight in areas of high thermally induced shear stresses, and eventually less so where maximum shear stresses are low. Lower predicted shear stresses occur at the NW and SE ends of the modeled portion of the Lake Edison Granodiorite.

Figures 10-13 depict modeling results for superposed thermal and tectonic stresses. Tectonic stresses were superposed upon the thermal stresses to evaluate whether a better match of observed photolineament pattern and calculated most compressive stress trajectories could be obtained. The principal tectonic stress directions used in these calculations are those of Fig. 3a-c. The geometry of the pluton itself suggests a most compressive tectonic stress trending N45W. The mean orientation of the first generation of aplite dikes suggest a most compressive regional stress oriented N20W, and the mean orientation of the joints in the pluton indicates a most compressive stress acting N70E (Christiansen, 1995). Magnitudes of the tectonic stresses were chosen to highlight their effects on the resulting overall stress field. The following points emerge if non-isotropic tectonic stresses are considered:

- As the difference between the tectonic principal stresses increases, so does the tendency for the joints to cross the pluton with small deflection and to predominantly track the direction of the most compressive tectonic stress. The actual photolineaments, however, exhibit a distinctive curvature across the pluton. Therefore small differences between the tectonic principal stresses are most likely to help match the observed photolineament pattern the best.

- If σ_H trends N45W and σ_H - σ_h is less than or equal to 90 MPa (Fig. 10), then the directions of the modeled most compressive stress only partially matches the observed fracture pattern. Modeled most compressive stress trajectories, especially at the Kle-Kmo contact, depart from the photolineaments by as much as 45°. This principal tectonic contribution fails to improve the match of observations and predictions.

- If σ_H trends N45W and σ_H - σ_h is greater than 90 MPa (Fig. 11), then the orientations of the most compressive principal stresses near the NW and SE ends of the modeled portion of the pluton are oriented along the long axis of the pluton. This coincides with the locations at which the magnitudes of the thermally induced shear stresses are the lowest (Fig. 9c). The pattern of Fig. 11 is also not consistent with the field observations.

- If σ_H trends N20W and σ_H - σ_h is 30 MPa (Fig. 12), then the predicted most compressive stress trajectories throughout the modeled portion of the pluton trend mostly NE. For greater differences of σ_H and σ_h the predicted directions of the most compressive

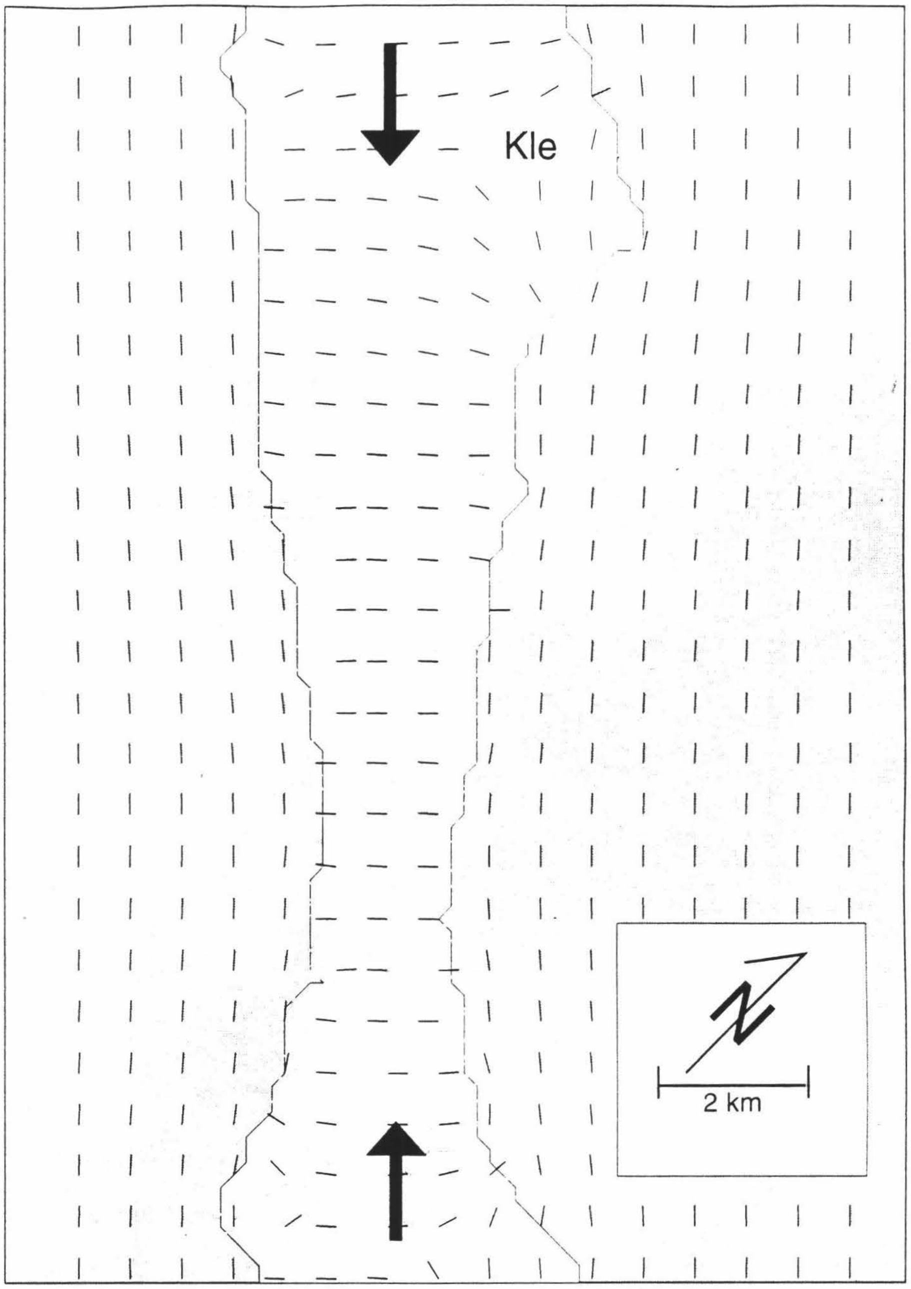

Figure 10. Directions of calculated most compressive stress (heavy ticks) after superposing a remote most compressive stress (black arrows) of 90 MPa at N45W upon the thermal stresses at 86 m.y. Photolineaments in Kle are shown in gray for comparison. Stress trajectories in the shaded area show the direction of the horizontal most compressive thermal stress direction in the host rock due to the cooling of Kle, and are not supposed to match the photolineament pattern there. No photolineaments are shown at locations where Kle is covered by younger deposits (see Fig. 1 for comparison).

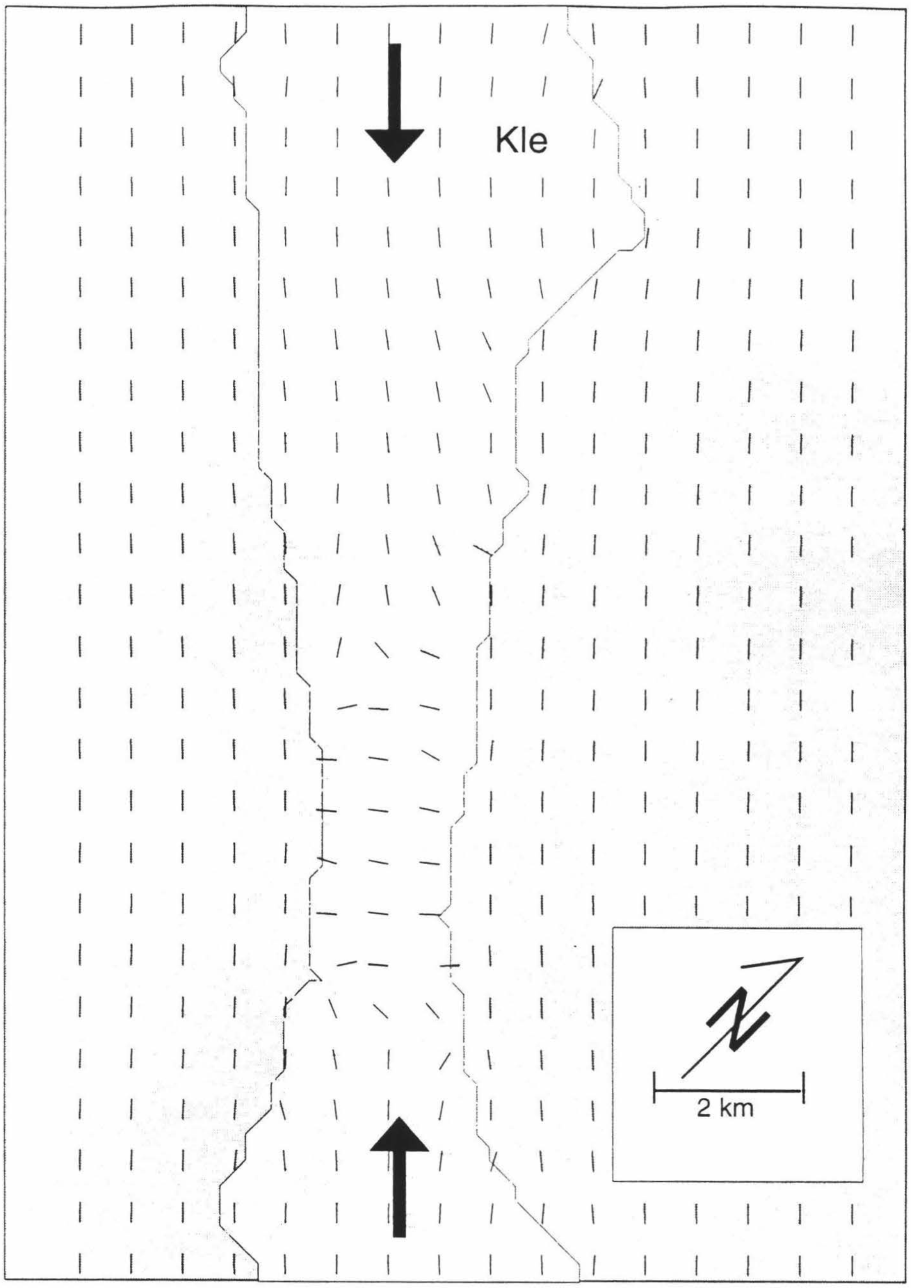

Figure 11. Directions of calculated most compressive stress (heavy ticks) after superposing a remote most compressive stress (black arrows) of 150 MPa at N45W upon the thermal stresses at 86 m.y. Photolineaments in Kle are shown in gray for comparison. Stress trajectories in the shaded area show the direction of the horizontal most compressive thermal stress direction in the host rock due to the cooling of Kle, and are not supposed to match the photolineament pattern there. No photolineaments are shown at locations where Kle is covered by younger deposits (see Fig. 1 for comparison).

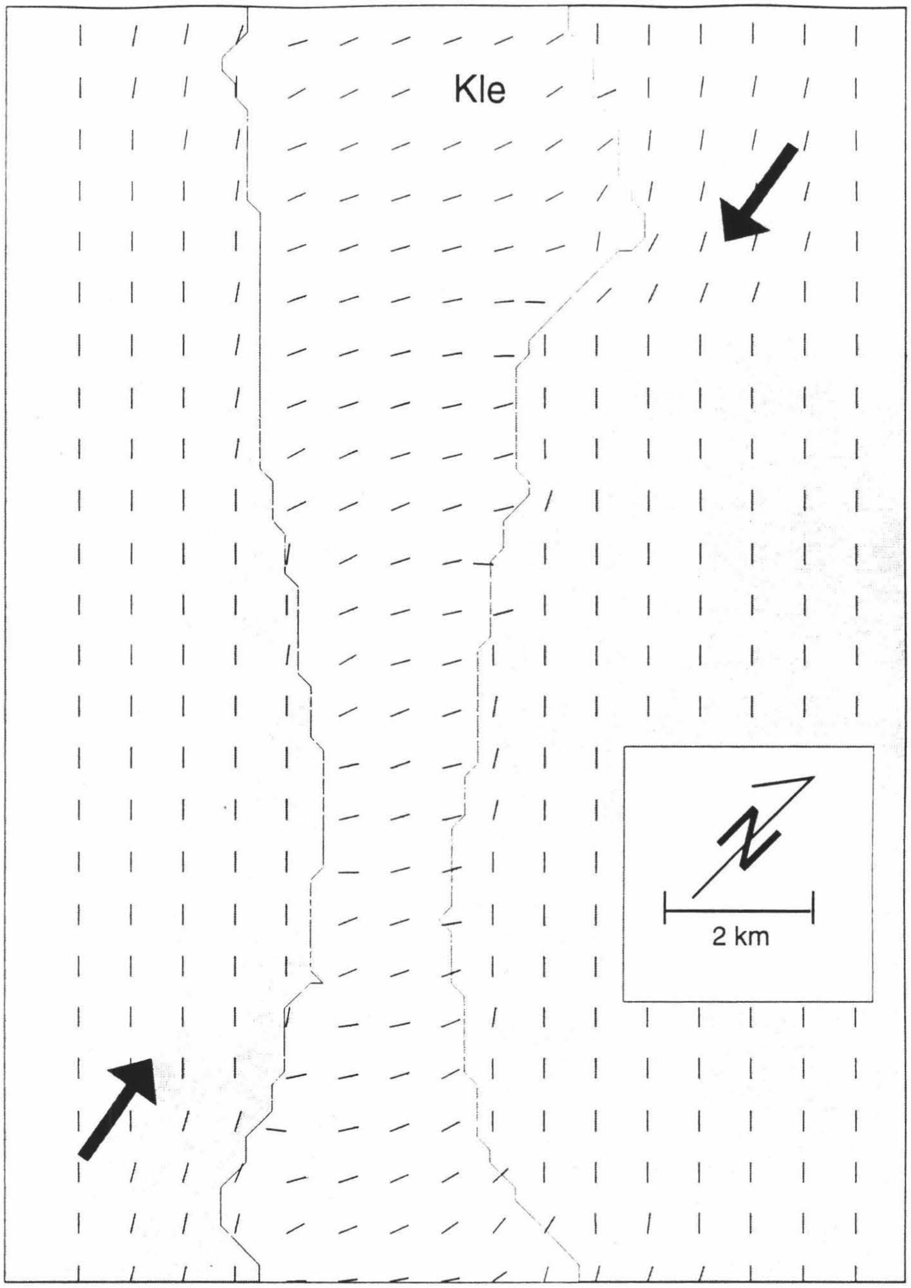

Figure 12. Directions of calculated most compressive stress (heavy ticks) after superposing a remote most compressive stress (black arrows) of 30 MPa at N20W upon the thermal stresses at 86 m.y. Photolineaments in Kle are shown in gray for comparison. Stress trajectories in the shaded area show the direction of the horizontal most compressive thermal stress direction in the host rock due to the cooling of Kle, and are not supposed to match the photolineament pattern there. No photolineaments are shown at locations where Kle is covered by younger deposits (see Fig. 1 for comparison).

stress becomes oriented more and more along the direction of the remote most compressive stress σ_H. This is not in agreement with the observed photolineament pattern.

- A series of trials showed that if σ_H trends N70E and σ_H - σ_h is 10 MPa (Fig. 13), then the directions of the modeled most compressive horizontal stress in the Lake Edison Granodiorite match the observed photolineament pattern better than where tectonic stresses are absent (i.e., Fig. 9). The differences between Figs. 9b and 13a are somewhat subtle, but the curvature of the photolineaments in the northwest half of the study area is better matched by the model where the tectonic stress is included (Fig. 13a). This direction of the most compressive tectonic stress equals the proposed principal stress direction in the pluton at the time the joints formed (Fig. 3c; Christiansen, 1995). Applying a greater difference between σ_H and σ_h would force the predicted most compressive stress trajectories to cross the pluton with almost no deflection, and would therefore not match the observed curvature of the photolineaments in the pluton. Figure 13b illustrates the maximum shear stress magnitudes for this case. The values are comparable to the results for thermal stresses alone (Fig. 9c), with maximum values of 102 MPa. Figure 13c shows the stress trajectories from Fig. 13a with photolineaments from Fig. 1, except that photolineaments trending north to N15E are excluded; these photolineaments are more abundant in the southeast part of the study area. Photolineaments of this orientation were not predicted by the thermo-mechanical model, and I thus infer that they originated from a stress source other than thermal, or are perhaps due to stress redistribution after fracturing. There is no independent evidence available for disregarding this set of fractures other than their trend. An analysis of aerial photographs and field examination could test whether this set of fractures indeed formed

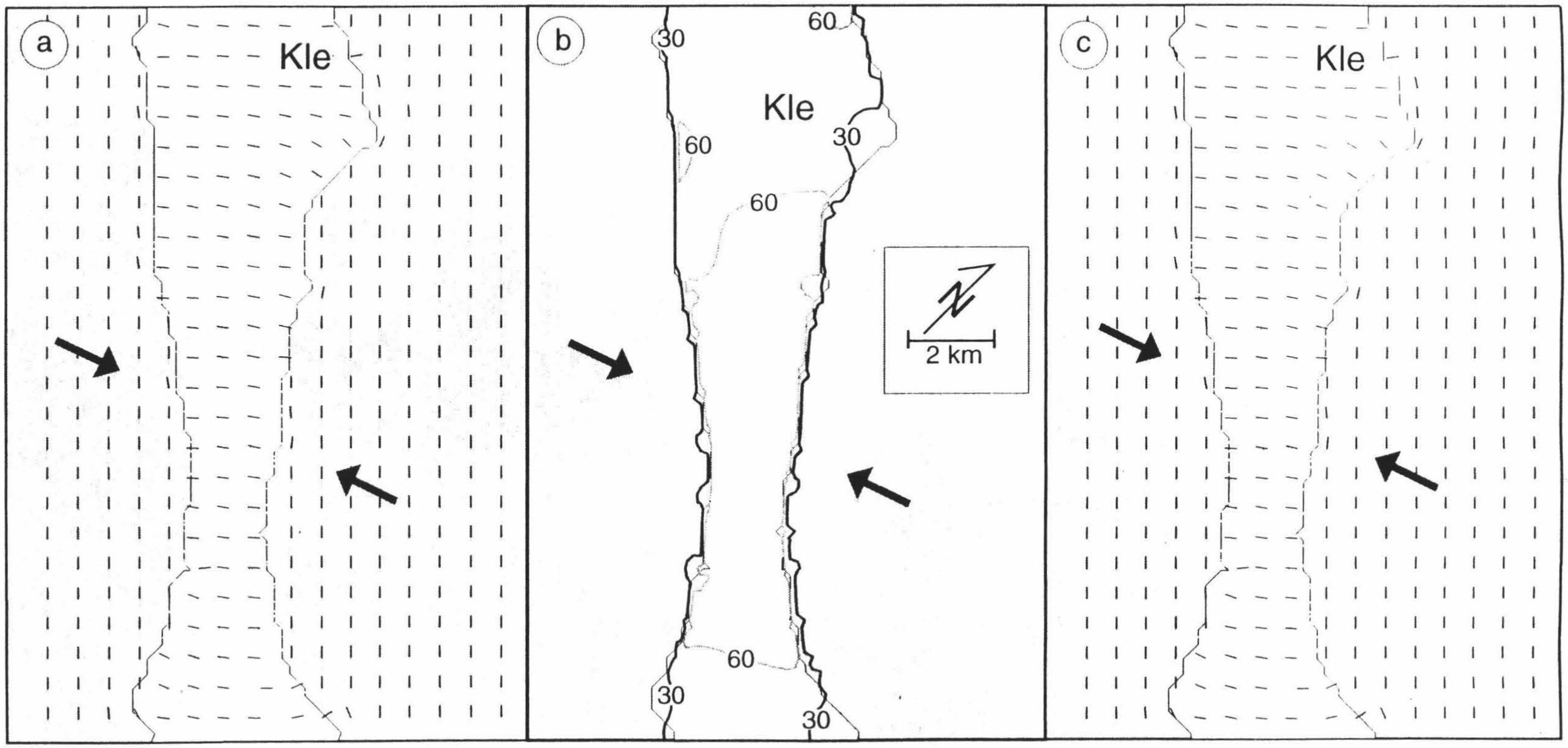

Figure 13. Calculated stresses for the Lake Edison Granodiorite (Kle) at 86 m.y. after superposing a remote compressive stress (black arrows) of 10 MPa at N70E to the thermal stresses. (a)Directions of the calculated most compressive stress (heavy ticks) and Kle-photolineaments from Fig. 1 (gray lines) for comparison. (b) Maximum shear stress in MPa. (c) Modeled ticks from (a) and photolineaments of Fig. 1 without those trending north to N15E. Stress trajectories in the shaded area show the directions of the horizontal most compressive stress in the host rock due to the cooling of Kle, and are not supposed to match the photolineament pattern there. No photolineaments are shown at locations where Kle is covered by younger deposits (see Fig. 1 for comparison).

in response to a dif nt stress source. The ren ng photolineaments and predicted most compressive s s orientations in this Fig. 1. atch rather well.

In addition to the stress calculations, the strain arising from thermal cooling can be calculated. Using Hooke's law for thermo-elastic materials (Timoshenko and Goodier, 1970), a coefficient of thermal expansion α of 8×10^{-6} $°C^{-1}$, and the average temperature in the Lake Edison Granodiorite at 86 m.y., the average thermal strain associated with cooling of the pluton would be 1.3×10^{-3}. This is roughly an order of magnitude greater than the joint-accommodated strain determined by Segall and Pollard (1983a) for outcrops in the Mount Givens Granodiorite. The calculated strains associated with cooling are thus more than sufficient to account for the documented strains.

Chapter 10: Discussion

Geometry strongly effects the orientation of the principle stresses in a cooling pluton. For elongate plutons the preferred orientation of the most tensile stress in the pluton changes during cooling becoming more parallel to its long axis with time. Also, adjacent to intrusions with convex surfaces (circle), the most tensile thermal stresses in the host rock trend perpendicular to the contact at all times, whereas in places where the contact is concave (hourglass) the most tensile stresses in the host can parallel the contact.

Thermal stresses magnitudes also depend significantly on pluton geometry. Calculated thermal stresses in the hourglass plutons, for example, are locally much greater than in the rectangular pluton. Figures 7 and 8 show that stresses are highest where the pluton cooled the most (the corners) and also where it is the thinnest (the waist). The presence of a narrow waist results in a tensile stress concentration, similar to that found in notched samples under uniaxial tension.

The preceding analyses strongly suggests that thermal stresses that occur during the initial cooling of the Lake Edison Granodiorite are of sufficient magnitude to significantly effect jointing in the pluton. The general conclusions are robust even given the uncertainties in temperatures and pressures during cooling. For example, even if uncertainties in these temperatures resulted in a temperature drop too large by 100 K, the error introduced in the computed most tensile stress would only be approximately 20 MPa. This would not change my conclusions qualitatively considering the calculated most tensile thermal stresses magnitudes of 60 to 123 MPa. Furthermore, the solid elastic thermo-mechanical parameter ($E\alpha$) of 0.24 MPa/°C used here is half that of Gerla (1988). Adopting his value would double the calculated thermal stress magnitudes. Even though the fluid pressures and tectonic loads are only weakly constrained, they are unlikely to dwarf thermal stresses of the magnitudes calculated.

A uniform regional stress field alone can not account for the observed curvature of the photolineaments in Fig. 1. In spite of its simplicity, the model used for the thermo-mechanical analysis reproduces the observed joint pattern reasonably well. The match is better in the northwest half of the modeling domain than in the southeastern half. This is somewhat surprising, for the highest thermally induced stresses are predicted in the southeast. The simplest explanation for discrepancies between predictions and observations is that there are at least two distinct sets of fractures. If photolineaments that trend north to N15E are removed from the data set (Fig 13c), the match between model predictions and observations improves markedly. Perhaps the north- to northeast-trending photolineaments represent a second, and non-thermal, set of fractures. Other possible reasons for the discrepancies in the southeastern part of the study area are material heterogeneity and anisotropy: a dike-like intrusion of late Cretaceous age (Kqm1 in Fig. 1) strikes parallel to the long axis of the pluton there, and the Rosy Finch shear zone also crosses the pluton in this area. Both could have perturbed the stress field in this area during fracturing. If the shear zone formed before the joints, it could have influenced joint propagation. At this point the relative ages of the joints and the shear zone remain an outstanding issue.

Other possible explanations are problematic. First, the difference in predicted stress orientations and observed photolineaments could partially be due to assumptions made for the thermo-elastic analyses. I have assumed that the pluton cooled with its contacts as shown on the geologic map. The position and shape of the east contact of the Lake Edison Granodiorite could have been different when the Mono Creek pluton intruded: the existing geometry of the Kle-Kmo contact might not reflect the geometry of the contact at the time the Lake Edison Granodiorite cooled and fractured. However, the observed flow-foliation within the Lake Edison Granodiorite parallels the contact, indicating that the contact geometry might not have changed significantly due to the intrusion of the Mono Creek Granite. Second, stress redistribution due to the fracturing process is not accounted for. Joint propagation affects the stress field in the vicinity of the crack such that the effective most tensile stress locally can depart from its original orientation by as much as 90° (Pollard and Segall, 1987). This could result in multiple fracture orientations where induced thermal stresses are high and driving stresses are sufficient in magnitude to produce more than one set of joints. However, this possibility does not account for the good match in the northwest half of the study area. Third, the most compressive thermal stress direction within an intrusion can change during cooling (Bergbauer et al., 1998). With ongoing cooling, the direction in which a pluton loses heat is influenced less by the local contact geometry and more by the overall pluton geometry. Joints that form early in the cooling history would be oriented roughly perpendicular to the local contact geometry, whereas joints that form late in the cooling history would tend to strike perpendicular to the long axis of a pluton. Depending on the time at which the stress distribution is shown, the orientation of the stress trajectories can vary significantly. I have attempted to overcome this problem by assuming a tensile stress threshold at which the pluton is assumed to fracture. The trajectories shown in Figs. 9-13 for the Lake Edison Granodiorite were "frozen in" when a tensile stress magnitude of 10 MPa was reached. Given the fracture toughness of granite (Ingraffea, 1987) and its grain size, 10 MPa is a reasonable value for joint propagation. This method required calculating the thermal stresses at different times. The time at which this threshold is met at a point could be resolved better by introducing smaller time steps in the calculations. The discrepancies of predictions and observations could also be partially due to an incorrectly assumed tensile stress threshold. Again, this possibility does not account for the good match in the northwest half of the study area.

I based the predictions of the magnitude of the tectonic differential stress and the direction of the most compressive tectonic stress at the time the joins opened by trying to best match the observed photolineaments. Considering a proposed value of 50 MPa by McGarr (1980) for the differential stress at three kilometers depth, and a differential stress of approximately 50 MPa measured in the KTB deep-borehole in Germany at a depth of eight kilometers (Brudy et al., 1997), the value for the differential stress of 10 MPa in Fig. 13 appears to be reasonable. A larger differential stress would force the most compressive stress direction to cross the pluton with less deflection, which would not be in agreement with the observed photolineament pattern. However, the effect of the remote differential stress on the most compressive stress direction depends partially on the magnitude of the thermally induced most tensile stresses. If thermal stresses in the pluton were greater in magnitude, e.g. by using a greater solid elastic thermo-mechanical parameter, a greater remote differential stress magnitude could be applied and would still be consistent with the observed photolineament pattern.

Bateman and Wahrhaftig (1966) stated that the joints in Sierran plutons formed "after the consolidation of the entire batholith" because "they cross pluton boundaries with little or no deflection". Faults and fault zones indeed do extend well across pluton contacts, but my field documentation demonstrates that numerous joints terminate near the Kl-Kle contact, and that joint geometry across that contact varies significantly. A cooling pluton with concave-in contacts (e.g. plutons shaped like hourglasses) can induce most compressive stresses in the adjacent rock that are normal to the contact. This would permit some joints to extend straight across a pluton boundary for some distance. Positive driving stresses that would open a joint in one pluton could also drive the joint some distance into a neighboring rock even if a joint-normal compressive stress acted there (Pollard and Muller, 1976). Thus a thermal stress source does not necessarily require joints to terminate exactly at a pluton boundary.

Chapter 11: Predictions: Granodiorite of Cartridge Pass

In order to test the viability of the thermo-elastic analysis, an additional pluton from the Sierra Nevada batholith was modeled, the Granodiorite of Cartridge Pass (Fig. 14, Moore, 1963, 1978; Bateman, 1965, 1992). This pluton is located approximately 50 km SE of the Mt. Abbot field area, is Cretaceous in age, and is younger than all the neighboring plutons. I modeled the Granodiorite of Cartridge Pass (Kcr) as cooling from an intrusion temperature of 750°C for 0.9 m.y. towards an ambient temperature of 300°C (Bergbauer et al., 1998). Modeled thermal stresses for the Granodiorite of Cartridge Pass are of the same magnitude as predicted thermal stresses for the Lake Edison Granodiorite. A tectonic most compressive horizontal stress at N55E, 30 MPa more compressive than the least compressive stress, was superposed to the thermal stresses to produce the model result shown in Fig. 14. The direction for the most compressive horizontal tectonic stress is similar to the direction used for the Lake Edison Granodiorite. Modeled most compressive stress directions (black ticks) are in good agreement with observed photolineaments (gray lines). Please note that photolineament abundance within the pluton does not scale with the predicted thermal stress magnitudes. Aerial photographs show that lineaments north of 37°00' trend east to northeast, in good agreement with the predictions. These photolineaments lie outside the Mt. Pinchot quadrangle, so they were not mapped by Moore (1963). An unpublished photolineament map by Moore does not show photolineaments in the westernmost part of the Granodiorite of Cartridge Pass. Aerial photographs of that area show that abundant talus conceals much of the bedrock, but two sets of lineaments are present. One set trends north, and the other northeast. Photolineaments of this general orientation are predicted by the model. Based on the model results I infer that photolineaments within the pluton largely reflect joints that occurred during cooling of the pluton.

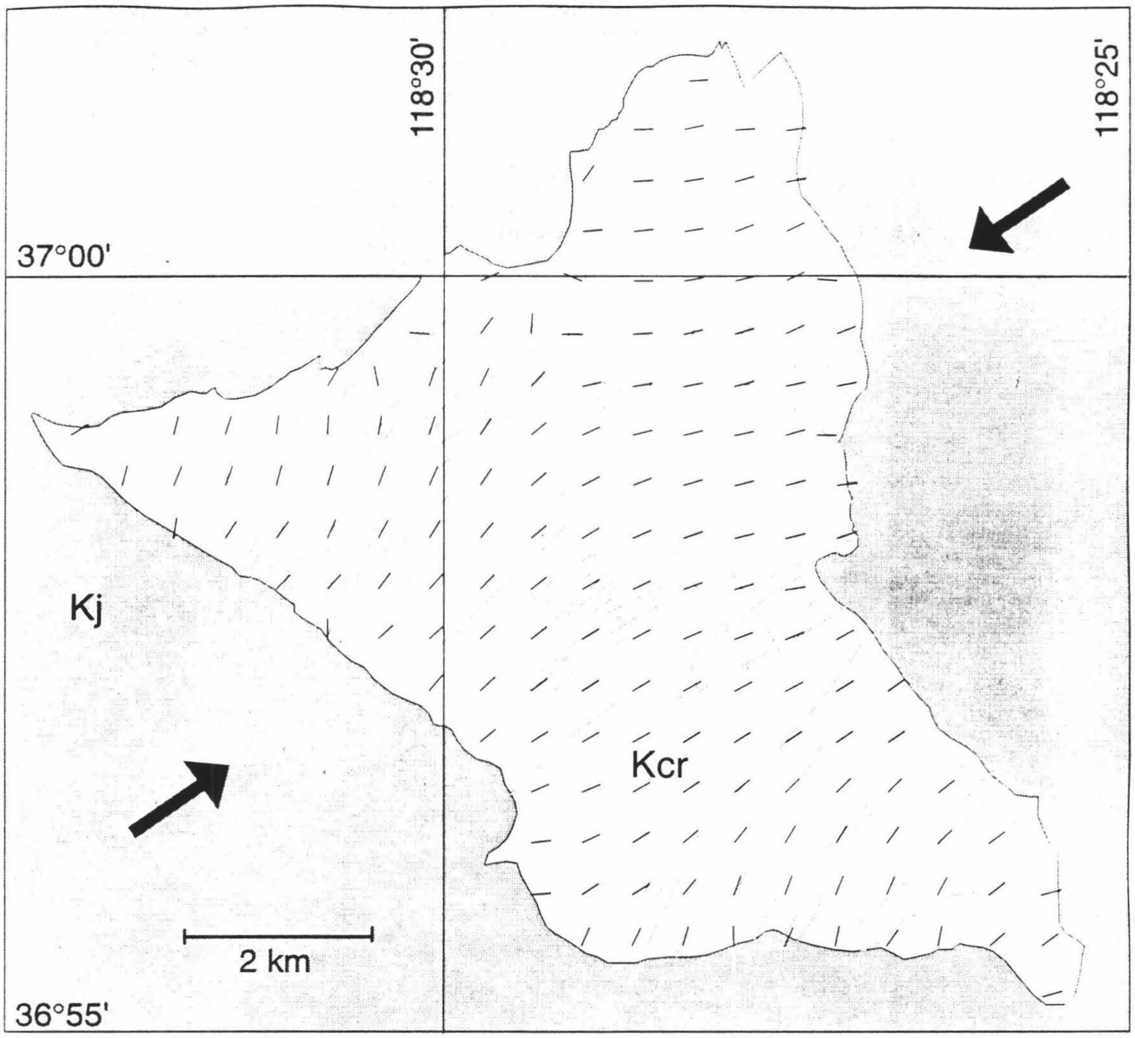

Figure 14. Geologic and photolineament map (after Moore, 1963; Moore, unpublished data) and modeled most compressive stress directions (black ticks) for the Granodiorite of Cartridge Pass (Kcr) after 0.9 m.y. of cooling. All geologic units older than Kcr are labeled Kj. A most compressive tectonic stress (black arrows) of 30 MPa greater than the least compressive stress acting at N55E was superposed upon the thermal stresses. Existing large fractures north of 37°00' and in the westernmost part of Kcr have yet to be mapped as photolineaments .

Chapter 12: Conclusions

The age, mineralogy, kinematics, and geometry of east-northeast-striking joints in the Lake Edison Granodiorite are consistent with the joints originating when the pluton cooled. Fracture geometry on different scales suggests stresses intrinsic to the pluton are responsible for the formation of the vertical joints. Radiometric, geochemical, and kinematics data tie the formation of the joints to the time when the temperature in the pluton was between the hornblende and the biotite closure temperatures. A two-dimensional thermo-elastic stress analysis indicates that thermal stress magnitudes of 60 to 123 MPa could have been attained. These would contribute significantly to the driving stress for jointing. The orientation of the modeled most compressive thermal stress trajectories within the pluton are grossly consistent with the orientation of the joints as revealed by the photolineaments. If the most compressive tectonic horizontal stress were oriented at N70E and exceeded the least compressive stress by 10 MPa, the stress field in the pluton would match the observed photolineament pattern slightly better. Moreover, maximum shear stresses calculated for the pluton agree with proposed driving stresses for the formation of straight joints. Finally, calculated average strains from the thermal stresses are more than sufficient to account for the strain accommodated by the joint openings. Thermal stresses thus appear to be a dominant and plausible mechanism for the formation of the joints in a cooling pluton. If my conclusions apply to other plutons as well, then the general orientations of the early formed joints in a pluton could be predicted mainly from its geometry and age relative to the adjacent rocks.

Appendix A: Thermo-mechanical numerical code

This numerical thermo-elastic code, written in MATLAB, models the conductive cooling in 2-D of the Lake Edison Granodiorite, and calculates the resulting thermal stresses in the intrusion and the host rock. Lines starting with "%" are explanatory only.

The input matrix (Tistress) consists of the initial temperature distribution at the time the younger plutons (Kl, Kmg) have cooled for 3 m.y., and Kle has just intruded instantaneously. Initially, a grid was lain over the geologic map, and nodes in different plutons were assigned different variables. Before the intrusion of the younger plutons (Kl, Kmg), the temperature distribution throughout the modeling domain was set to the ambient temperature (Tambient = 230°C). Then the younger plutons (Kl, Kmg) intruded. Intrusions are modeled by assigning an intrusion temperature (Tintrude = 800°C) to nodes located inside the two plutons in map view. After 3 m.y. of cooling, Kle was intruded by assigning Tintrude to the nodes that coincide with Kle as shown on the geologic map.

```
% data input


load Tcontacts.dat;      % a temp. distribution needed to draw the pluton boundaries
V1=500:100:800;


% initial temperature distribution input, right after Kl cooled and Kle intruded
load Tistress.dat
Ti2=Tistress;
(n,l)=size(Ti2);
```

```
if l/2~=ceil(l/2)
        H=(‘n & l have to be multiples of 2')
        elseif n/2~=ceil(n/2)
                HH=(‘n & l have to be multiples of 2')
        else
                k=5;                % thermal conductivity in W/m/K
end

ro=2630;                            % density in kg/m^3
c= 775;                             % specific heat in J/kg/K
kappa=k/ro/c;                       % diffusivity in m^2/s
a=8e-6;                             % thermal expansion in 1/C from Skinner
E=3.04e4;                           % Young's modulus in MPa
v=0.25;                             % Poisson's ratio
beta=E/(1-v^2);

% introduce matrices
thetaa=zeros(n,l);
flag=zeros(n,l);
thetaa=thetaa(n/2:n,ceil(l/2+50):ceil(l/2+110));        % area of interest of modeling
domain
flag=flag(n/2:n,ceil(l/2+50):ceil(l/2+110));            % area of interest of modeling
domain
Tcontacts=Tcontacts(n/2:n,ceil(l/2+50):ceil(l/2+110));          % area of interest of domain
```

```
% define modeling domain and set up mesh
dx=200;                                          % spacing of mesh in m
ymax=(n-1)*dx;
y=0:dx:ymax;
xmax=(l-1)*dx;
x=0:dx:xmax;
(X,Y)=meshgrid(x,y);
X1=X(n/2:n,ceil(l/2+50):ceil(l/2+110));          % area of interest in the modeling domain
Y1=Y(n/2:n,ceil(l/2+50):ceil(l/2+110));          % area of interest in the modeling domain

% calculating wavenumbers:
kx=2*pi/xmax*fftshift(-l/2:l/2-1);
ky=2*pi/ymax*fftshift(-n/2:n/2-1);
(Kx,Ky)=meshgrid(kx,ky);

% FFT of initial temperature distribution
FC=fft2(Ti2);

clear Tistress y x X Y kx ky

% begin cooling and thermal stress loop for different cooling times
for tmax=(1e5 1e6 2e6 3e6);                      % cooling time in years
e=num2str(tmax);                                 % for plotting routine

clear theta thetaa2 map SIGxx SIGyy SIGxy Ta q S1 S2 X2 Y2 T Tmax
```

```
% calculating cooling
t=tmax*3600*24*365.25;                          % conversion from years to secs
Ta=ifft2(exp(-kappa*t*(Kx.^2+Ky.^2)).*FC);      % temperature distribution after t
Ta=real(Ta);
max(Ta(:,1))                         % check how much heat has reached the boundaries
max(Ta(:,l))
max(max(Ta))


% calculating the integral (Tdt) from 0 to t
t0=0;                                           % initial time
FA=exp(-kappa*t*(Kx.^2+Ky.^2)).*FC;
FIA1=(-1./(kappa*(Kx.^2+Ky.^2))).*FA;           % integral(FA)
FIA2=(-1./(kappa*(Kx.^2+Ky.^2))).*exp(-kappa*t0*(Kx.^2+Ky.^2)).*FC;
FIA=FIA1-FIA2;
FIA(1,1)=FA(1,1)*(t-t0);
%I=ifft2(FIA);                                  % I is the integral (Tdt) from 0 to t
clear FA FIA1 FIA2

Fpsi=(1+v)/(1-v)*a*kappa*FIA;                   % thermo-elastic stress potentials
clear FIA

% calculating 2nd partials of Fpsi wrt x and y
psix=ifft2(-Kx.^2.*Fpsi);
```

```
psiy=ifft2(-Ky.^2.*Fpsi);
psixy=ifft2(-Kx.*Ky.*Fpsi);
clear Fpsi

% calculating stresses
delT=Ta-Ti2;                                              % temperature drop
SIGxx=beta*(real(psix)+v*real(psiy)-(1+v)*a*delT);
SIGyy=beta*(real(psiy)+v*real(psix)-(1+v)*a*delT);
SIGxy=E/(2*(1+v))*real(psixy);
clear psix psiy psixy

% change size of some matrices for plotting routine
SIGxx=SIGxx(n/2:n,ceil(l/2+50):ceil(l/2+110));
SIGyy=SIGyy(n/2:n,ceil(l/2+50):ceil(l/2+110));
SIGxy=SIGxy(n/2:n,ceil(l/2+50):ceil(l/2+110));
T=Ta(n/2:n,ceil(l/2+50):ceil(l/2+110));
(r,ra)=size(T);

% add remote tectonic stress to thermal stress field
phit=115;                          % direction of remote most compressive stress
m=num2str(phit);
phi=phit*pi/180;                   %E-W=0, NE-SW=-45, NW-SE=45
Sr=(-30 0; 0 0);                   % remote tectonic stress tensor
o=num2str(Sr(1,1));
h=num2str(Sr(2,2));
```

```
ad=(cos(phi) sin(phi); -sin(phi) cos(phi));
Srp=ad*Sr*ad';                  % transformation
SIGxx=SIGxx+Srp(1,1);
SIGyy=SIGyy+Srp(2,2);
SIGxy=SIGxy+Srp(1,2);

S1=SIG1(SIGxx,SIGyy,SIGxy);           % most tensile
S2=SIG2(SIGxx,SIGyy,SIGxy);           % most compressive
Tmax=abs(0.5.*(S1-S2));               % maximum shear stress
theta = angp(SIGxx,SIGyy,SIGxy);      % direction of most compressive stress
clear SIGxx SIGyy SIGxy

% freeze the trajectories inside the 10 MPa contour
q=find(S1>=10 & flag~=1);
flag(q)=ones(size(q));
thetaa(q)=theta(q);
%thetaa=theta;                   % if you don't want to freeze the trajectories


% plotting routines for Temperature distribution, most tensile stress with trajectories, and
% the maximum shear stress

% plotting temperature distribution

g='JSG/temp/';
```

```
gg=(g e h o);
b='Temperature for t=';
d=(b e c h f o kl m);

figure
V=200:25:800;
map=contour(X1,Y1,T,V);
clabel(map,V)
title(d)
xlabel('x')
ylabel('y')
old on
map=contour(X1,Y1,Tcontacts,V1,':');
axis('equal')
print(gg,'-dpsc')

% plotting most tensile stress with most compressive stress trajectories

c=' years, Shr=';
f=', SHr= ';
kl=', angle= ';
g='JSG/S1/';
gg=(g e h o);
b='S1,  t=';
d=(b e c h f o kl m);
```

```
figure
map=contour(X1,Y1,Tcontacts,V1,'w:');
hold on
V2=(0, 10, 30, 60, 90, 120);
map=contour(X1,Y1,S1,V2,'b');
hold on
map=contour(X1,Y1,Tcontacts,V1,'w:');
hold on
thetaa2=thetaa(1:4:r,1:4:ra);
X2=X1(1:4:r,1:4:ra);
Y2=Y1(1:4:r,1:4:ra);
traj2 (X2,Y2,-1.*sin(thetaa2),cos(thetaa2),'w');
axis('equal')
title(d)
xlabel('x')
ylabel('y')
print(gg,'-dpsc')

% plotting maximum shear stress

g='JSG/shear/';
gg=(g e h o);
b='Tmax, t=';
d=(b e c h f o kl m);
```

```
figure
V2=(0,30, 60, 90, 120, 150);
map=contour(X1,Y1,Tmax,V2);
clabel(map,V2)
hold on
map=contour(X1,Y1,Tcontacts,V1,'w:');
axis('equal')
title(d)
xlabel('x')
ylabel('y')
print(gg,'-dpsc')

end                                          % end of cooling  time-loop

% calculate mean strain in the modeling domain

% load temperature distribution before any intrusion occurred (Ti_Kl), then image twice
to % invoke boundary conditions
Ti_Kl
Ti=Ti_Kl;
(n,l)=size(Ti);
w=3101;       % pad with zeros...o has to be odd 2901!!!
To=zeros(n,l+w);
for p=1:w
```

```
        To(:,l+p)=Ti(:,l);
end
To(:,1:l)=Ti;
(n,l)=size(To);


for p=1:n       % imaging N-S
        Ti1(n+1-p,:)=To(p,:);
end
Ti3=(Ti1; To); % add Kle (lower part of picture) and its image (upper)
(n,l)=size(Ti3);
for p=1:l       % imaging E-W
        Ti4(:, l+1-p)=Ti3(:,p);
end
Ti2=(Ti4 Ti3);
(n,l)=size(Ti2);
j=find(Ti2==z);
Ta=Ta(j).*ones(size(j));
Ti2=Ti2(j).*ones(size(j));
delT=Ti2-Ta;
strain=mean(mean(delT))*a
-----------------------------------------------------------------------------------------------------
```

Appendix B: Derivation of formulas used in the numerical code

The thermo-elastic code (Appendix A) consists of two major parts. The first part calculates temperature distributions for 2-D conductive cooling, the second part then computes thermal stresses and strains using thermo-elastic stress potentials. The actual computer code is written in MATLAB, and I therefore include the MATLAB translation here of the important formulas used in the code (Appendix A). The numerical routine employs fast Fourier transforms (FFT) to solve the equations. I transform a given spatial array, such as a temperature distribution, into the frequency domain and let them decay there. Numerical codes based on this technique are known as spectral codes. The fast Fourier transform is a fast version of the general Fourier transform and is used in numerical routines to speed up the calculations.

Performing a Fourier or spectral analysis allows me to express any wave as a sum of simple waves, represented by the exponential terms, multiplied by their amplitudes (coefficients). Here, this analysis is performed on a spatial wave, i.e., the temperature distribution in 2-D. To do this, the wave-frequencies have to be "selected". Those wave frequencies (wave numbers) depend on the spatial dimensions of the modeling domain, but not on position or time.

Step 1: Solving the diffusion equation in 2-D using the spectral method to calculate the temperature distribution $T_{(x,y,t)}$ at a given cooling time t:

The diffusion equation assumes the following form:

$$\frac{\partial T}{\partial t} = k \cdot \nabla^2 T, \qquad (12)$$

with κ being the thermal diffusivity, $T_{(x,y,t)}$ being the temperature field at any cooling time t. Defining T using Fourier series notation in 2-D yields:

$$T(x,y,t) = \sum_{k_x}\sum_{k_y} C_{k_x}(t) \cdot C_{k_y}(t) \cdot e^{i \cdot k_x \cdot x} \cdot e^{i \cdot k_y \cdot y}, \qquad (13)$$

with C_{kx} and C_{ky} being the Fourier coefficients, and k_x and k_y being the wave numbers. The Fourier coefficients are defined as:

$$C_{k_x}(t) \cdot C_{k_y}(t) = \sum_{k_x}\sum_{k_y} T(x,y,t) \cdot e^{-i \cdot k_x \cdot x} \cdot e^{-i \cdot k_y \cdot y}. \qquad (14)$$

Wave numbers in the physical (spatial) domain for the 2-D case assume the following form using Matlab:

$$\begin{aligned} k_x &= \frac{2p}{x_{\max}} \cdot fftshift(-\frac{q}{2}:\frac{q}{2}-1) \\ &, \qquad (15) \\ k_y &= \frac{2p}{y_{\max}} \cdot fftshift(-\frac{n}{2}:\frac{n}{2}-1), \end{aligned}$$

in which q and n are the number of grid-points in x and y of the modeling domain, respectively. X_{max} and Y_{max} are the maximum dimensions of the modeling domain. To simplify the analysis let us begin by expressing T(x,y,t) using the Fourier series notation for one wavenumber only:

$$T(x,y,t) = C_{k_x}(t) \cdot C_{k_y}(t) \cdot e^{i \cdot k_x \cdot x} \cdot e^{i \cdot k_y \cdot y}. \tag{16}$$

Substituting for T in (12) using (16) leads to the following expression:

$$\frac{d\left[C_{k_x}(t) \cdot C_{k_y}(t)\right]}{dt} \cdot e^{i \cdot k_x \cdot x} \cdot e^{i \cdot k_y \cdot y}$$

$$= \kappa \cdot \left[\frac{\partial^2 (e^{i \cdot k_x \cdot x})}{\partial^2 x} \cdot e^{i \cdot k_y \cdot y} \cdot C_{k_x}(t) \cdot C_{k_y}(t) + \frac{\partial^2 (e^{i \cdot k_y \cdot y})}{\partial^2 y} \cdot e^{i \cdot k_x \cdot x} \cdot C_{k_x}(t) \cdot C_{k_y}(t)\right].$$

The derivative on the left hand side can be written as a full integral, since C_{kx} and C_{ky} only depend on t but not on x or y. Performing the partial derivatives on the right hand side of the equation gives:

$$\frac{d\left[C_{k_x}(t) \cdot C_{k_y}(t)\right]}{dt} \cdot e^{i \cdot k_x \cdot x} \cdot e^{i \cdot k_y \cdot y} =$$

$$\kappa \cdot \left[-k_x{}^2 \cdot C_{k_x}(t) \cdot C_{k_y}(t) - k_y{}^2 \cdot C_{k_x}(t) \cdot C_{k_y}(t)\right] \cdot e^{i \cdot k_x \cdot x} \cdot e^{i \cdot k_y \cdot y}.$$

The exponential-terms on both sides cancel each other out.

$$\frac{d\left[C_{k_x}(t)\cdot C_{k_y}(t)\right]}{dt} = -\kappa\cdot(k_x{}^2 + k_y{}^2)\cdot C_{k_x}(t)\cdot C_{k_y}(t). \qquad (17)$$

Equation (6) now can be solved by regularly integrating over t and ($C_{kx}\cdot C_{ky}$), respectively:

$$\frac{d\left[C_{k_x}(t)\cdot C_{k_y}(t)\right]}{C_{k_x}(t)\cdot C_{k_y}(t)} = -\kappa\cdot\left(k_x{}^2 + k_y{}^2\right)\cdot dt$$

$$\Leftrightarrow \ln\left[C_{k_x}(t)\cdot C_{k_y}(t)\right] = -\kappa\cdot\left(k_x{}^2 + k_y{}^2\right)\cdot t + A \qquad (18)$$

$$\Leftrightarrow C_{k_x}(t)\cdot C_{k_y}(t) = e^{-\kappa\cdot\left(k_x{}^2+k_y{}^2\right)\cdot t}\cdot A',$$

where

$$A' = e^{A}$$

Expression (18) was derived using the simplification of only considering one wavenumber in x and y. However, combining (18) and (13) leads to a more general expression for T:

$$T(x,y,t) = \sum_{k_x}\sum_{k_y} e^{-\kappa\cdot\left(k_x{}^2+k_y{}^2\right)\cdot t}\cdot A'\cdot e^{i\cdot\left(k_x\cdot x+k_y\cdot y\right)}. \qquad (19)$$

In Matlab, the forward Fourier transformation and its inverse are defined as

$$FFT2 = \sum_{k_x}\sum_{k_y} e^{-i\cdot(k_x\cdot x + k_y\cdot y)}, \qquad \text{(forward)} \qquad (20)$$

and

$$IFFT2 = \sum_{k_x}\sum_{k_y} e^{i\cdot(k_x\cdot x + k_y\cdot y)}, \qquad \text{(inverse)} \qquad (21)$$

respectively. Combining (19) and (21) yields:

$$T(x,y,t) = IFFT2\left[A'\cdot e^{-\kappa\cdot({k_x}^2 + {k_y}^2)\cdot t}\right]. \qquad (22)$$

An expression for A' can be found using initial conditions:

$$\begin{aligned} &T(x,y,t_0) = T(x,y,0) = IFFT2[A'] \\ &\Leftrightarrow A' = FFT2[T(x,y,0)]. \end{aligned} \qquad (23)$$

Combining equations (22) and (23) leads to the final expression for the temperature distribution over time:

$$T(x,y,t) = IFFT2\left[e^{-\kappa\cdot(k_x{}^2 + k_y{}^2)\cdot t} \cdot FFT2(T(x,y,0)) \right]. \qquad (24)$$

Equation (24) shows that the temperature distribution in 2-D after a specific time of cooling can be calculated analytically by first transforming the initial temperature distribution into the frequency domain (Fourier space), multiplying it by a decay term, and subsequently transforming it back into the spatial domain (physical space). For the cases presented here, this solution proves to be an efficient way to solve the diffusion equation because the code does not have to step through time. Test results show that the spectral code method is two to three orders of magnitude faster than a finite-differences scheme.

Step 2: Calculating thermal stresses and strains using thermo-elastic stress potentials:

The formulation for the thermo-elastic stress potentials is taken from Timoshenko and Goodier (1970). However, the integration limits used in the cases presented here differ from the ones Timoshenko and Goodier consider in their book. Starting from the general formulation for the derivative of the thermo-elastic stress potentials, the formula Timoshenko and Goodier used is derived and then contrasted with the equation used here. From there the relationship between the potentials and the stresses and strains is established. Then the appropriate Matlab formulation used in the numerical code is described.

The integration limits are different because I consider the case where thermal stresses arise in a plate initially free of thermal stresses, whereas Timoshenko and Goodier consider that thermal stresses decay in a plate that is already stressed thermally. This initial condition assumed by Timoshenko and Goodier (1970) is not explicitly stated in their book, but it can be inferred by looking at the result for the thermo-elastic stress potentials (equation (o), page 480).

The initial conditions can be obtained from the following formula for the derivative of the thermo-elastic displacement potential ψ with respect to time t on page 480 of Timoshenko and Goodier (1970):

$$\frac{d\psi}{dt} = \frac{1+\nu}{1-\nu} \cdot \alpha \cdot \kappa \cdot T, \tag{25}$$

where α is the coefficient of thermal expansion. Integrating (25) with respect to t yields:

$$\psi_2 - \psi_1 = \frac{1+\nu}{1-\nu} \cdot \alpha \cdot \kappa \cdot \int_{t_1}^{t_2} T dt. \tag{26}$$

According to Hooke's law for thermo-elastic materials, thermal stresses are directly related to the second partial derivative of ψ with respect to x and y. If ψ =0 for all points x and y, then no thermal stresses exist because the second derivative of ψ will equal zero in that case.

Case a:

From equation (o) in Timoshenko and Goodier, their initial conditions can be extracted. Here is their equation (o):

$$\psi = -\frac{1+\nu}{1-\nu} \cdot \alpha \cdot \kappa \cdot \int_{t}^{\infty} T dt. \tag{o}$$

Suppose in equation (15) I set $t_1 = t$, $\psi_1 = \psi$, $t_2 = \infty$, and $\psi_2 = 0$:

$$0 - \psi_1 = \frac{1+\nu}{1-\nu} \cdot \alpha \cdot \kappa \cdot \int_{t}^{\infty} T dt. \tag{27}$$

This clearly corresponds to equation (o) of Timoshenko and Goodier (1970). The term ψ_1 is proportional to all the heat energy that will be lost in the plate after an infinite amount of cooling (i.e., to all the thermo-elastic potential that must be lost). Timoshenko and Goodier have addressed the problem where temperature T initially varies in a plate, so the integral in (27) will vary from point to point; it will not be a constant. Hence:

at $t = t_1$, $\psi_1 \neq 0$, so the modeling domain is thermally stressed;

as $t \Rightarrow \infty$, $\psi_1 \Rightarrow 0$, so the modeling domain is stress free.

Apparently, Timoshenko and Goodier's formula (o) applies to a plate that is initially thermally stressed and that the stresses drop to zero as the plate cools.

Case b:

Now suppose that in equation (26) I set $t_1 = 0$, $\psi_1 = 0$, and $t_2 = t$:

$$\psi_2 - 0 = \frac{1+\nu}{1-\nu} \cdot \alpha \cdot \kappa \cdot \int_0^t T dt. \tag{28}$$

Now the term ψ_2 is proportional to all the heat energy that will be lost in the plate after an infinite amount of cooling. Hence:

at t = 0, $\psi_2 = 0$, so the modeling domain is stress free

at t = ∞: $\psi_2 \neq 0$, so the modeling domain is thermally stressed.

This represents the cases discussed here because I consider the magma and host rock to be initially free of thermal stresses. As the pluton cools and solidifies the modeling domain builds up thermal stresses. This leads to the following formula based on (28):

$$\psi = \frac{1+\nu}{1-\nu} \cdot \alpha \cdot \kappa \cdot \int_0^t T dt. \tag{29}$$

This is the expression for the thermo-elastic stress potentials used here. An expression for the integral in (29) needs to be found now. Using the final result for the temperature distribution after a certain cooling time (24), the integral assumes the following form:

$$\psi(x,y)=\frac{1+\nu}{1-\nu}\cdot\alpha\cdot\kappa\cdot\int_0^t IFFT2\left[e^{-\kappa\cdot\left(k_x{}^2+k_y{}^2\right)\cdot t}\cdot FFT2(T(x,y,t_0))\right]dt$$

$$\Leftrightarrow \psi(x,y)=\frac{1+\nu}{1-\nu}\cdot\alpha\cdot\kappa\cdot IFFT2\left[\frac{e^{-\kappa\cdot\left(k_x{}^2+k_y{}^2\right)\cdot t}}{-\kappa\cdot\left(k_x{}^2+k_y{}^2\right)}\cdot FFT2(T(x,y,t_0))\right]_0^t . \tag{30}$$

Thermo-elastic stresses can be calculated using Hook's Law for thermo-elastic materials:

$$\sigma_{xx}=\frac{E}{1-\nu^2}\cdot\left[\frac{\partial u}{\partial x}+\nu\cdot\frac{\partial v}{\partial y}-(1-\nu)\cdot\alpha\cdot\Delta T\right],$$

$$\sigma_{yy}=\frac{E}{1-\nu^2}\cdot\left[\frac{\partial v}{\partial y}+\nu\cdot\frac{\partial u}{\partial x}-(1-\nu)\cdot\alpha\cdot\Delta T\right], \tag{31}$$

$$\sigma_{xy}=\frac{E}{2\cdot\left(1-\nu^2\right)}\cdot\left[\frac{\partial u}{\partial x}+\frac{\partial v}{\partial y}\right],$$

where u and v are the displacements in x and y, respectively. The partial derivatives in (31) can be calculated by means of the thermo-elastic stress potentials:

$$u=\frac{\partial\psi(x,y)}{\partial x}$$

and

$$v = \frac{\partial \psi(x,y)}{\partial y}$$

Therefore:

$$\frac{\partial u}{\partial x} = \frac{\partial^2 \psi(x,y)}{\partial x^2}$$

and

$$\frac{\partial v}{\partial y} = \frac{\partial^2 \psi(x,y)}{\partial y^2}. \qquad (32)$$

I now need to find an expression for the thermo-elastic stress potentials ψ in order to be able to calculate the partial derivatives in (32). This can be done by defining thermo-elastic stress potentials ψ as a Fourier series, and ψ' as its inverse:

$$\psi' = \sum_{kx}\sum_{ky} \psi(x,y) \cdot e^{-i \cdot (kx \cdot x + ky \cdot y)}, \qquad \text{(forward)} \qquad (33)$$

and

$$\psi(x,y) = \sum_{kx}\sum_{ky} \psi'_{kx,ky} e^{i \cdot (kx \cdot x + ky \cdot y)}. \qquad \text{(inverse)} \qquad (34)$$

The partial derivatives in (32) can now be expressed as:

$$\frac{\partial \psi(x,y)}{\partial x} = \sum_{kx}\sum_{ky} \psi' \cdot i \cdot kx \cdot e^{i\cdot(kx\cdot x + ky\cdot y)}$$

and

$$\frac{\partial^2 \psi(x,y)}{\partial x^2} = \sum_{kx}\sum_{ky} \psi' \cdot \left(-kx^2\right) \cdot e^{i\cdot(kx\cdot x + ky\cdot y)}.$$

Similar equations arise calculating the partials with respect to (y^2) and ($x \cdot y$).

Using the Matlab expressions (20) and (21), the partial derivatives in 2-D assume the form:

$$\frac{\partial^2 \psi(x,y)}{\partial x^2} = IFFT2\left[-kx^2 \cdot FFT2(\psi(x,y))\right],$$

$$\frac{\partial^2 \psi(x,y)}{\partial y^2} = IFFT2\left[-ky^2 \cdot FFT2(\psi(x,y))\right], \qquad (35)$$

$$\frac{\partial^2 \psi(x,y)}{\partial x \partial y} = IFFT2\left[-kx \cdot ky \cdot FFT2(\psi(x,y))\right].$$

Combining equations (30),(31) , and (35) now allows me to calculate thermal stresses in an elastic thin plate after cooling for a time t.

Appendix C: Sample locations and radiometric data

Table 2. Locations of new samples used in the radiometric analyses (map units according to Lockwood & Lydon, 1975)

ID	**Sample**	**Minerals**	**Map Unit**	
J18/19	KLEF3	Hornblende/Biotite	Lake Edison Granodiorite	Klef
J20/21	KLE4	Hornblende/Biotite	Lake Edison Granodiorite	Kle
J22/23	KLEP5	Hornblende/Biotite	Lake Edison Granodiorite	Klep
J24/25	KL2	Hornblende/Biotite	Lamarck Granodiorite	Kl
J27/28	KMR2	Hornblende/Biotite	Mono Creek Granite	Kmr
J30	KLE1	K-Feldspar	Lake Edison Granodiorite	Kle

ID	**Sample**	**Longitude (N)**	**Latitude (W)**	**Elevation (ft)**
J18/19	KLEF3	37°19'44''	118°52'24''	9,800
J20/21	KLE4	37°20'38''	118°52'24''	9,400
J22/23	KLEP5	37°21'06''	118°51'26''	9,700
J24/25	KL2	37°19'11''	118°52'55''	10,000
J27/28	KMR2	37°21'07''	118°51'21''	9,780
J30	KLE1	37°21'06''	118°51'29''	9,680

ID	**Sample**	**Location Description**
J18/19	KLEF3	ca. 130m north of the creek that drains Orchid Lake, ca. 60 m east of Kl/Klef contact
J20/21	KLE4	ca. 80m east of John Muir Trail, ca. 200m south of Hilgard Branch of Bear Creek
J22/23	KLEP5	ca. 120m north of Hilgard Branch of Bear Creek, ca. 95m west of Klep/Kmr contact
J24/25	KL2	ca. 1km south-east of Orchid Lake
J27/28	KMR2	ca. 60m north of Hilgard Branch of Bear Creek, ca. 25 m east of Klep/Kmr contact
J30	KLE1	ca. 250m north of Hilgard Branch of Bear Creek, ca. 60m west of Kle/Klep contact

Table 3. Summary of radiometric dating results for all samples

ID	Sample	Mineral	Total Gas Age (Ma)	SD (Ma)
J18	KLEF3H	Hornblende	86.5	0.8
J19	KLEF3B	Biotite	83.0	0.1
J20	KLE4H	Hornblende	88.7	0.4
J21	KLE4B	Biotite	80.7	0.2
J22	KLEP5H	Hornblende	85.3	0.7
J23	KLEP5B	Biotite	80.6	0.2
J24	KL2H	Hornblende	90.3	0.7
J25	KL2B	Biotite	80.0	0.2
J27	KMR2H	Hornblende	84.5	0.6
J28	KMR2B	Biotite	81.1	0.1
J30	KLE1	K-Feldspar	77.3	0.3

ID	Sample	Weighted Mean Age(Ma)	SE (Ma)	MSWD
J18	KLEF3H	86.2	0.2	11
J19	KLEF3B	83.4	0.1	189
J20	KLE4H	88.4	0.1	11
J21	KLE4B	81.2	0.1	202
J22	KLEP5H	86.0	0.2	11
J23	KLEP5B	81.1	0.1	144
J24	KL2H	90.8	0.2	4
J25	KL2B	81.2	0.1	238
J27	KMR2H	84.5	0.2	7
J28	KMR2B	81.7	0.04	99
J30	KLE1	-	-	-

(1) corresponds to a MSWD of 1.0

ID	Sample	Adjusted SE (Ma)[1]	Isochron Age (Ma)	s (Ma)
J18	KLEF3H	0.7	86.0	0.3
J19	KLEF3B	0.7	84.8	0.1
J20	KLE4H	0.5	87.8	0.2
J21	KLE4B	0.7	82.0	0.1
J22	KLEP5H	0.6	86.3	0.3
J23	KLEP5B	0.6	81.6	0.1
J24	KL2H	0.4	91.2	0.3
J25	KL2B	0.9	82.6	0.1
J27	KMR2H	0.5	85.1	0.3
J28	KMR2B	0.4	82.1	0.04
J30	KLE1	-	-	-

ID	Sample	MSWD	Adjusted SE (Ma)[1]	Trapped ^{40}Ar/^{36}Ar	σ
J18	KLEF3H	12.6	1.1	301	4
J19	KLEF3B	83	0.5	204	3
J20	KLE4H	10	0.8	328	9
J21	KLE4B	179	0.8	237	2
J22	KLEP5H	12	1.1	284	10
J23	KLEP5B	152	0.7	256	0
J24	KL2H	4	0.6	281	7
J25	KL2B	122	0.7	232	2
J27	KMR2H	7	0.7	276	8
J28	KMR2B	41	0.3	234	3
J30	KLE1	-	-	-	-

Table 4. Ar-diffusion data for sample Klef3H (J18)

step	T (C)	t (min)	$^{40}Ar/^{39}Ar$	$^{38}Ar/^{39}Ar$	$^{37}Ar/^{39}Ar$	$^{36}Ar/^{39}Ar$	^{39}Ar (mol)	$\Sigma ^{39}Ar$	$^{36}Ar/^{40}Ar$	Cl/K
1	750	10	8.155	3.31E-02	7.84E-02	4.04E-03	5.39E-14	17.6	4.94E-04	5.36E-03
2	800	10	8.485	3.10E-02	2.63E-01	4.38E-03	4.62E-14	32.7	5.09E-04	4.76E-03
3	850	10	8.592	3.34E-02	8.10E-01	4.78E-03	1.65E-14	38.1	5.34E-04	5.41E-03
4	900	10	8.275	3.77E-02	9.38E-01	3.90E-03	2.32E-14	45.6	4.44E-04	6.66E-03
5	950	10	7.476	8.49E-02	2.94E+00	3.28E-03	3.37E-14	56.7	3.41E-04	1.98E-02
6	1000	10	7.500	1.84E-01	5.36E+00	2.21E-03	7.49E-14	81.1	1.17E-04	4.74E-02
7	1025	10	8.228	1.99E-01	5.68E+00	5.92E-03	9.21E-15	84.1	5.48E-04	5.14E-02
8	1050	10	8.325	2.51E-01	7.16E+00	5.45E-03	2.36E-14	91.8	4.41E-04	6.61E-02
9	1120	10	15.06	2.42E-01	7.27E+00	2.88E-02	2.03E-14	98.4	1.80E-03	6.24E-02
10	1200	10	24.73	2.60E-01	6.92E+00	5.92E-02	4.77E-15	100.0	2.33E-03	6.57E-02

step	$\%^{40}Ar^*$	$^{40}Ar^*/^{39}Ar_K$	$\pm\sigma_{40/39}$	Age (Ma)	$\pm\sigma_{Age}$ (an)	$1/\sigma_{Age}^2$	(Age-Mean Age)^2	$^{39}Ar_K/^{40}Ar$	$\pm\sigma_{39/40}$	$\pm\sigma_{36/40}$
1	85.0	6.943	0.035	84.56	0.42	5.770	2.759	1.23E-01	2.48E-04	1.29E-05
2	84.6	7.188	0.040	87.47	0.47	4.457	1.570	1.18E-01	1.84E-04	1.51E-05
3	83.7	7.218	0.102	87.84	1.21	0.682	2.617	1.17E-01	2.99E-04	3.93E-05
4	86.4	7.172	0.072	87.29	0.85	1.384	1.133	1.21E-01	2.61E-04	2.84E-05
5	89.5	6.714	0.053	81.83	0.64	2.465	19.266	1.34E-01	3.17E-04	2.29E-05
6	96.1	7.244	0.038	88.14	0.45	4.974	3.697	1.33E-01	2.43E-04	1.59E-05
7	83.0	6.902	0.190	84.07	2.26	0.195	4.613	1.21E-01	3.90E-04	7.74E-05
8	86.5	7.254	0.072	88.26	0.86	1.355	4.159	1.20E-01	2.61E-04	2.84E-05
9	46.8	7.090	0.124	86.31	1.47	0.461	0.008	6.62E-02	1.22E-04	2.73E-05
10	31.1	7.748	0.438	94.12	5.18	0.037	62.429	4.03E-02	1.06E-04	5.93E-05
	Total Gas Age	**7.105**	**0.065**	**86.5**	**0.8**		**J-Factor**	**0.006912**		

step	$\pm\sigma_{Cl/K}$	Ca/K	$\pm\sigma_{Ca/K}$
1	7.10E-05	1.58E-01	1.57E-02
2	1.75E-04	5.32E-01	5.27E-02
3	2.13E-04	1.64E+00	1.62E-01
4	2.32E-04	1.90E+00	1.88E-01
5	1.49E-04	5.96E+00	5.90E-01
6	2.23E-04	1.09E+01	1.08E+00
7	6.37E-04	1.15E+01	1.14E+00
8	2.92E-04	1.45E+01	1.44E+00
9	5.47E-04	1.48E+01	1.46E+00
10	9.98E-04	1.40E+01	1.39E+00

Weighted	Mean	Age (Ma)	**86.2**
	Standard	Error (Ma)	**0.2**
		MSWD	**11.2**
Adjusted	Standard	Error (Ma)	**0.7**

***** INVERSE ISOCHRON PARAMETERS *****

ISOCHRON AGE (Ma): 85.95132
UNCERTAINTY: .2871485
TRAPPED 40Ar/36Ar: 301.3398
UNCERTAINTY 4.263863
SAMPLE 40Ar*/39Ar: 7.059603
UNCERTAINTY .0241512

***** NEW [illegible]RK REGRESSION PARAMETERS *****

SLOPE: 2.342738E-02
UNCERTAINTY: 3.892651E-04
Y-INT: 3.318513E-03
UNCERTAINTY: 4.695591E-05
X-INT: .141651
UNCERTAINTY 4.845942E-04
SWD: 12.63457

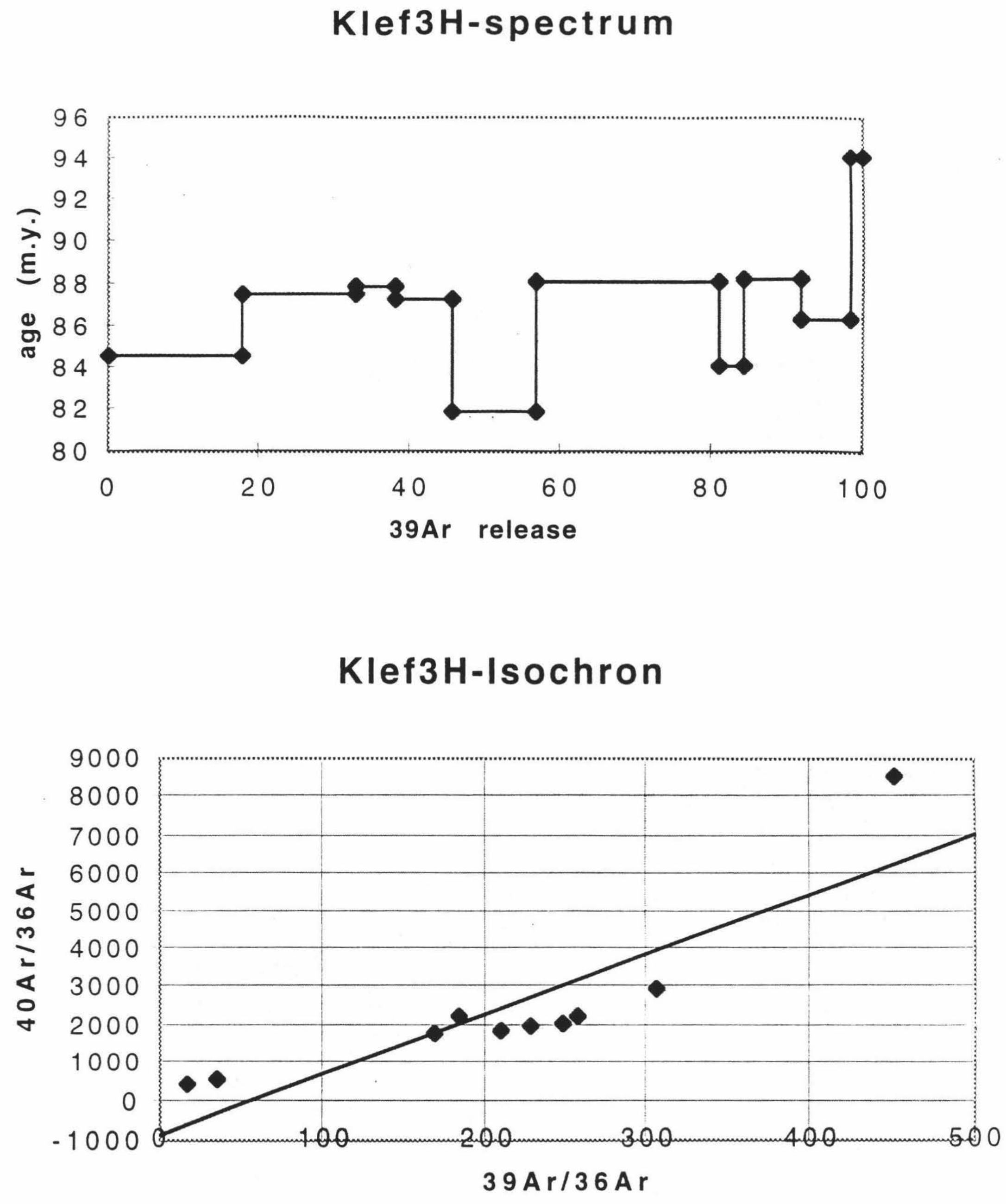

Figure 15. Spectrum and isochron plots for sample Klef3H (J18)

Table 5. Ar-diffusion data for sample Klef3B (J19)

step	T (C)	t (min)	^{40}Ar/^{39}Ar	^{38}Ar/^{39}Ar	^{37}Ar/^{39}Ar	^{36}Ar/^{39}Ar	^{39}Ar (mol)	Σ^{39}Ar	^{36}Ar/^{40}Ar	Cl/K
1	600	14	8.432039	3.31E-02	5.65E-03	7.92E-03	1.85E-13	7.97	9.42E-04	5.16E-03
2	650	10	7.548275	2.89E-02	2.87E-03	2.34E-03	2.66E-13	19.4	3.11E-04	4.29E-03
3	700	10	7.431239	0.027646	2.89E-03	1.76E-03	3.96E-13	36.5	2.37E-04	3.97E-03
4	750	10	7.262029	2.74E-02	3.89E-03	1.31E-03	1.88E-13	44.6	1.81E-04	3.93E-03
5	800	10	7.399433	2.83E-02	7.92E-03	1.40E-03	1.16E-13	49.6	1.90E-04	4.16E-03
6	850	11	7.325842	2.84E-02	8.83E-03	1.23E-03	1.10E-13	54.4	1.67E-04	4.19E-03
7	950	10	7.018036	2.77E-02	6.86E-03	4.22E-04	4.05E-13	71.8	6.00E-05	4.05E-03
8	1150	10	6.975353	2.71E-02	2.41E-02	2.94E-04	6.54E-13	100	4.14E-05	3.88E-03

step	%^{40}Ar*	^{40}Ar*/^{39}Ar$_K$	$\pm\sigma_{40/39}$	Age (Ma)	$\pm\sigma_{Age}$ (an)	$1/\sigma_{Age}^2$	(Age-Mean Age)^2	^{39}Ar$_K$/^{40}Ar	$\pm\sigma_{39/40}$	$\pm\sigma_{36/40}$
1	71.9	6.066	0.022	74.1	0.3	14.0100	87.0072	0.1189475	1.89E-04	7.36E-06
2	90.5	[illegible]31	0.013	83.2	0.2	44.1187	0.0407	0.1329206	1.73E-04	3.63E-06
3	92.6	[illegible]7	0.012	83.9	0.1	51.1394	0.2204	0.135021	1.81E-04	2.90E-06
4	94.3	[illegible]0	0.011	83.4	0.1	58.6209	0.0004	0.1381779	1.52E-04	3.54E-06
5	94.0	[illegible]1	0.016	84.8	0.2	28.5491	1.8036	0.1356029	2.54E-04	3.46E-06
6	94.6	[illegible]40	0.018	84.5	0.2	21.7757	1.1870	0.1369696	3.03E-04	3.73E-06
7	97.8	6.869	0.008	83.7	0.1	103.1705	0.0626	0.1429987	1.48E-04	1.93E-06
8	98.4	6.865	0.007	83.6	0.1	127.6865	0.0430	0.1438751	1.38E-04	1.60E-06
	Total Gas Age	**6.809**	**0.011**	**83.0**	**0.1**			**J-Factor**	**0.006911**	

step	$\pm\sigma_{Cl/K}$	Ca/K	$\pm\sigma_{Ca/K}$
1	1.08E-04	1.14E-02	1.13E-03
2	3.10E-05	5.80E-03	5.78E-04
3	1.59E-05	5.84E-03	5.86E-04
4	4.60E-05	7.85E-03	7.79E-04
5	9.01E-05	1.60E-02	1.59E-03
6	1.22E-04	1.78E-02	1.77E-03
7	8.45E-06	1.39E-02	1.37E-03
8	1.06E-05	4.88E-02	4.83E-03

Weighted Mean Age (Ma)	**83.42**
Standard Error (Ma)	**0.05**
MSWD	**188.8**
Adjusted Standard Error (Ma)	**0.6**

***** INVERSE ISOCHRON PARAMETERS *****

ISOCHRON AGE (Ma): 84.74666
UNCERTAINTY: 5.903989E-02
TRAPPED 40Ar/36Ar: 203.5116
UNCERTAINTY 2.565192
SAMPLE 40Ar*/39Ar: 6.959323
UNCERTAINTY 4.963071E-03

***** NEW YORK REGRESSION PARAMETERS *****

SLOPE: -3.419621E-02
UNCERTAINTY: 4.483987E-04
Y-INT: 4.913726E-03
UNCERTAINTY: 6.193581E-05
X-INT: .1436921
UNCERTAINTY 1.024747E-04
SWD: 82.57448

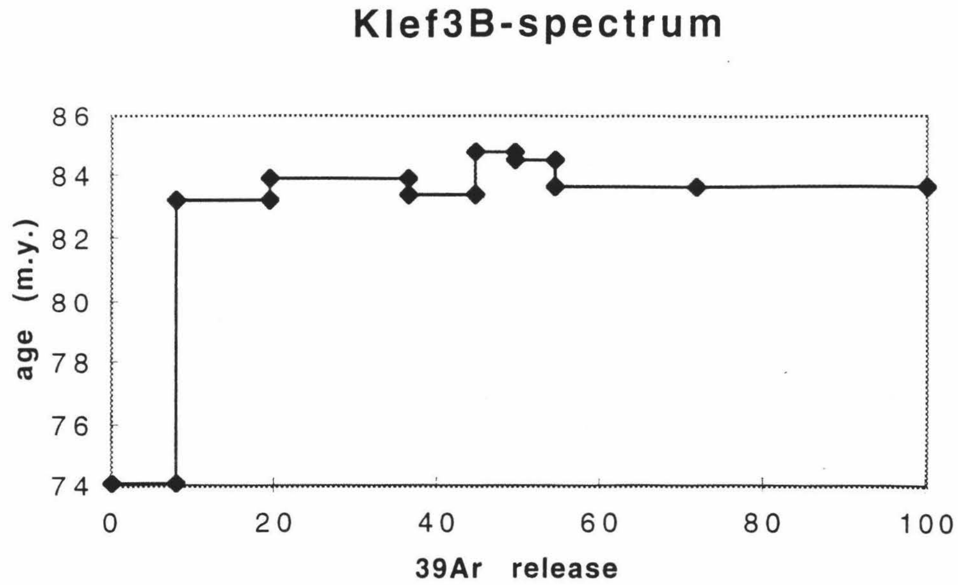
Klef3B-spectrum

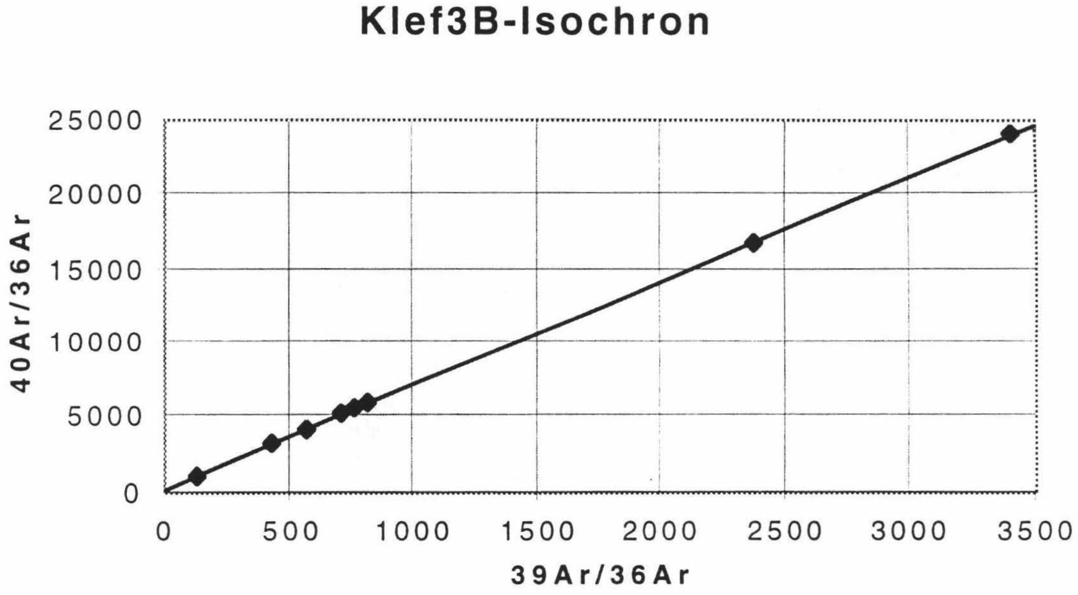
Klef3B-Isochron

Figure 16. Spectrum and isochron plots for sample Klef3B (J19)

Table 6. Ar-diffusion data for sample Kle4H (J20)

step	T (C)	t (min)	$^{40}Ar/^{39}Ar$	$^{38}Ar/^{39}Ar$	$^{37}Ar/^{39}Ar$	$^{36}Ar/^{39}Ar$	^{39}Ar (mol)	$\Sigma^{39}Ar$	$^{36}Ar/^{40}Ar$	Cl/K
1	750	10	8.340	2.29E-02	1.08E-01	3.53E-03	6.31E-14	16.3	4.21E-04	2.55E-03
2	850	10	8.365	2.50E-02	3.70E-01	2.00E-03	2.41E-14	22.6	2.29E-04	3.24E-03
3	950	10	7.648	7.04E-02	2.35E+00	1.88E-03	5.83E-14	37.6	1.69E-04	1.59E-02
4	980	10	7.481	2.09E-01	5.84E+00	2.34E-03	8.16E-14	58.7	1.18E-04	5.44E-02
5	1010	10	7.417	2.32E-01	5.25E+00	2.01E-03	4.38E-14	70.1	9.38E-05	6.09E-02
6	1050	10	7.756	2.42E-01	6.32E+00	3.65E-03	3.37E-14	78.8	2.68E-04	6.36E-02
7	1150	10	7.508	2.73E-01	6.93E+00	2.43E-03	5.25E-14	92.4	9.30E-05	7.25E-02
8	1300	10	9.578	2.92E-01	7.28E+00	9.30E-03	2.94E-14	100	7.83E-04	7.72E-02

step	$\%^{40}Ar^*$	$^{40}Ar^*/^{39}Ar_K$	$\pm\sigma_{40/39}$	Age (Ma)	$\pm\sigma_{Age}$ (an)	$1/\sigma_{Age}^2$	(Age-Mean Age)^2	$^{39}Ar_K/^{40}Ar$	$\pm\sigma_{39/40}$	$\pm\sigma_{36/40}$
1	87.2	7.282	0.031	88.6	0.4	7.420	0.023	1.20E-01	1.61E-04	1.18E-05
2	92.6	7.777	0.066	94.4	0.8	1.620	36.187	1.20E-01	1.32E-04	2.67E-05
3	94.5	7.254	0.031	88.2	0.4	7.420	0.034	1.31E-01	1.95E-04	1.28E-05
4	96.1	7.224	0.021	87.9	0.3	15.878	0.284	1.34E-01	1.13E-04	9.11E-06
5	96.7	7.213	0.038	87.8	0.5	4.919	0.442	1.35E-01	1.86E-04	1.67E-05
6	91.6	7.152	0.054	87.0	0.6	2.444	1.958	1.29E-01	2.58E-04	2.25E-05
7	96.8	7.313	0.034	88.9	0.4	6.300	0.267	1.33E-01	1.69E-04	1.45E-05
8	76.5	7.381	0.063	89.7	0.7	1.806	1.759	1.04E-01	2.72E-04	2.04E-05
	Total Gas Age	**7.289**	**0.037**	**88.7**	**0.4**		**J-Factor**	**0.006910**		

step	$\pm\sigma_{Cl/K}$	Ca/K	$\pm\sigma_{Ca/K}$
1	4.28E-05	2.18E-01	2.16E-02
2	1.92E-04	7.47E-01	7.40E-02
3	9.76E-05	4.76E+00	4.71E-01
4	1.59E-04	1.18E+01	1.17E+00
5	2.05E-04	1.06E+01	1.05E+00
6	3.87E-04	1.28E+01	1.27E+00
7	5.20E-04	1.41E+01	1.39E+00
8	5.23E-04	1.48E+01	1.46E+00

Weighted	Mean	Age (Ma)	**88.4**
	Standard	Error (Ma)	**0.1**
		MSWD	**10.8**
Adjusted	Standard	Error (Ma)	**0.5**

***** INVERSE ISOCHRON PARAMETERS *****

ISOCHRON AGE (Ma): 87.77782
UNCERTAINTY: .2359175
TRAPPED 40Ar/36Ar: 327.6542
UNCERTAINTY 8.824221
SAMPLE 40Ar*/39Ar: 7.215389
UNCERTAINTY 1.986816E-02

***** NEW YORK REGRESSION PARAMETERS *****

SLOPE: -2.202136E-02
UNCERTAINTY: 6.393902E-04
Y-INT: 3.051998E-03
UNCERTAINTY: 8.219491E-05
X-INT: .1385927
UNCERTAINTY 3.816262E-04

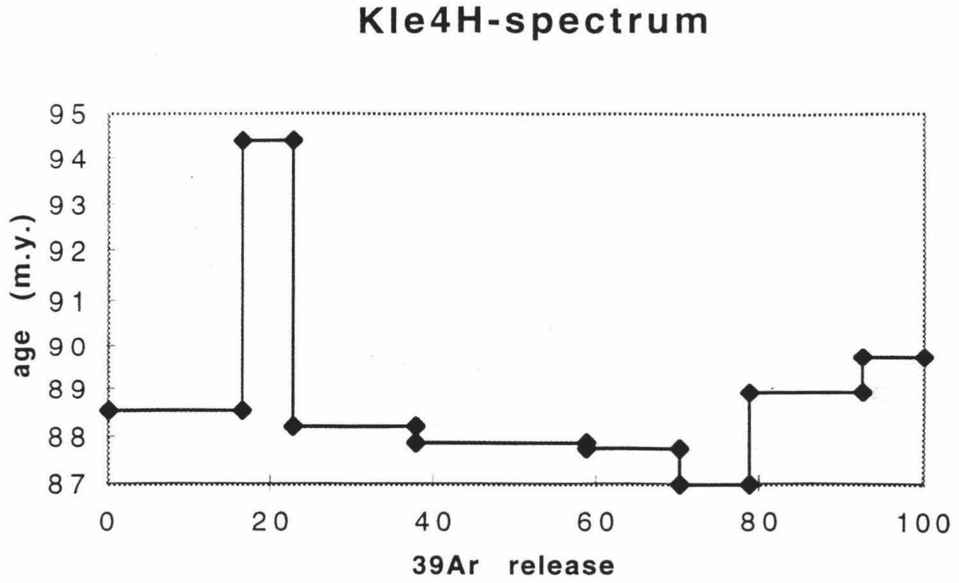

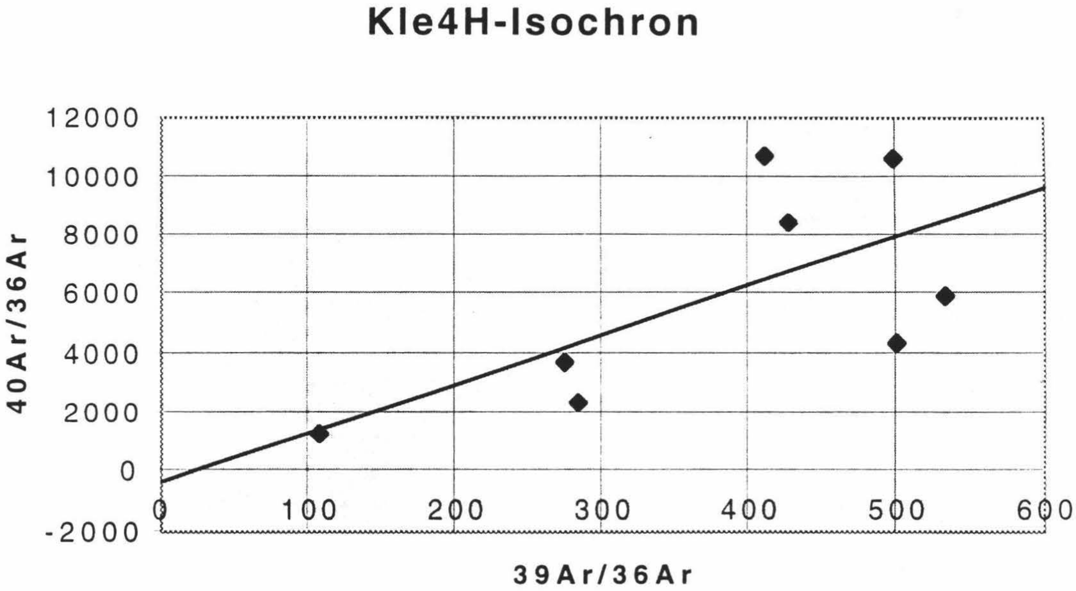

Figure 17. Spectrum and isochron plots for sample Kle4H (J20)

Table 7. Ar-diffusion data for sample Kle4B (J21)

step	T (C)	t (min)	^{40}Ar/^{39}Ar	^{38}Ar/^{39}Ar	^{37}Ar/^{39}Ar	^{36}Ar/^{39}Ar	^{39}Ar (mol)	Σ^{39}Ar	^{36}Ar/^{40}Ar	Cl/K
1	600	10	7.534	1.99E-02	1.32E-02	5.90E-03	4.06E-14	3.03	7.59E-04	1.48E-03
2	650	10	8.736	1.93E-02	5.09E-03	7.81E-03	1.73E-13	16.0	8.66E-04	1.23E-03
3	700	10	6.950	1.70E-02	3.37E-03	8.41E-04	1.23E-13	25.2	1.17E-04	9.50E-04
4	750	10	7.054	1.69E-02	4.18E-03	7.85E-04	9.28E-14	32.1	1.08E-04	9.27E-04
5	800	10	7.108	1.69E-02	5.59E-03	1.05E-03	8.15E-14	38.2	1.44E-04	9.28E-04
6	850	10	6.991	1.72E-02	5.24E-03	8.94E-04	1.31E-13	48.0	1.24E-04	1.00E-03
7	950	10	6.828	1.70E-02	7.91E-03	5.48E-04	4.72E-13	83.3	7.77E-05	9.58E-04
8	1150	10	7.099	1.79E-02	4.95E-02	1.20E-03	2.24E-13	100	1.63E-04	1.18E-03

step	%^{40}Ar*	^{40}Ar*/^{39}Ar$_K$	$\pm\sigma_{40/39}$	Age (Ma)	$\pm\sigma_{Age}$ (an)	$1/\sigma_{Age}^2$	(Age-Mean Age)^2	^{39}Ar$_K$/^{40}Ar	$\pm\sigma_{39/40}$	$\pm\sigma_{36/40}$
1	76.3	5.766	0.028	70.5	0.3	9.19	114.95	1.33E-01	3.88E-04	9.89E-06
2	73.3	6.404	0.023	78.1	0.3	13.60	9.59	1.15E-01	2.61E-04	7.78E-06
3	96.0	6.677	0.014	81.3	0.2	35.46	0.02	1.44E-01	3.76E-04	3.98E-06
4	96.2	6.797	0.012	82.8	0.1	47.79	2.54	1.42E-01	3.38E-04	3.97E-06
5	95.1	6.772	0.014	82.5	0.2	38.56	1.67	1.41E-01	3.43E-04	4.45E-06
6	95.8	6.702	0.025	81.6	0.3	11.24	0.21	1.44E-01	5.72E-04	3.52E-06
7	97.2	6.642	0.007	80.9	0.1	157.31	0.06	1.47E-01	3.23E-04	1.68E-06
8	94.6	6.722	0.011	81.9	0.1	63.00	0.49	1.41E-01	3.46E-04	1.93E-06
	Total Gas Age	**6.626**	**0.013**	**80.7**	**0.2**		**J-Factor**	**0.006908**		

step	$\pm\sigma_{Cl/K}$	Ca/K	$\pm\sigma_{Ca/K}$
1	1.02E-04	2.59E-02	2.57E-03
2	7.17E-05	1.00E-02	9.93E-04
3	4.08E-05	6.62E-03	6.58E-04
4	1.27E-05	8.21E-03	8.22E-04
5	2.71E-05	1.10E-02	1.09E-03
6	2.10E-05	1.03E-02	1.02E-03
7	2.23E-05	1.55E-02	1.54E-03
8	3.91E-05	9.72E-02	9.63E-03

Weighted	Mean	Age (Ma)	**81.19**
	Standard	Error (Ma)	**0.05**
		MSWD	**202.5**
Adjusted	Standard	Error (Ma)	**0.7**

***** INVERSE ISOCHRON PARAMETERS *****

ISOCHRON AGE (Ma): 82.03669
UNCERTAINTY: 5.964024E-02
TRAPPED 40Ar/36Ar: 236.6979
UNCERTAINTY 2.412363
SAMPLE 40Ar*/39Ar: 6.734609
UNCERTAINTY 5.008187E-03

***** NEW YORK REGRESSION PARAMETERS *****

SLOPE: -2.845234E-02
UNCERTAINTY: 3.034112E-04
Y-INT: 4.224794E-03
UNCERTAINTY: 4.305799E-05
X-INT: .1484867
UNCERTAINTY 1.10422E-04
SWD: 178.5983

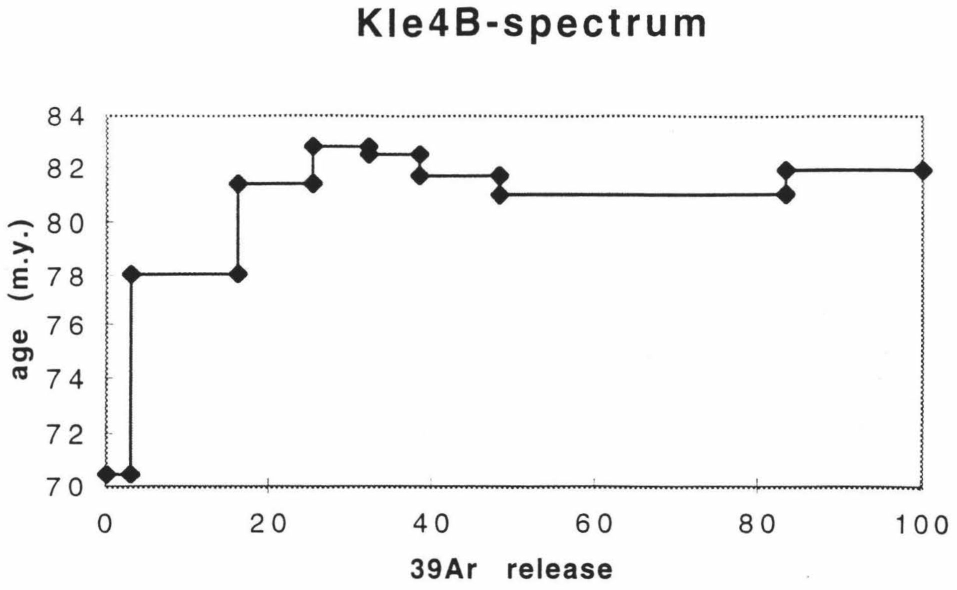

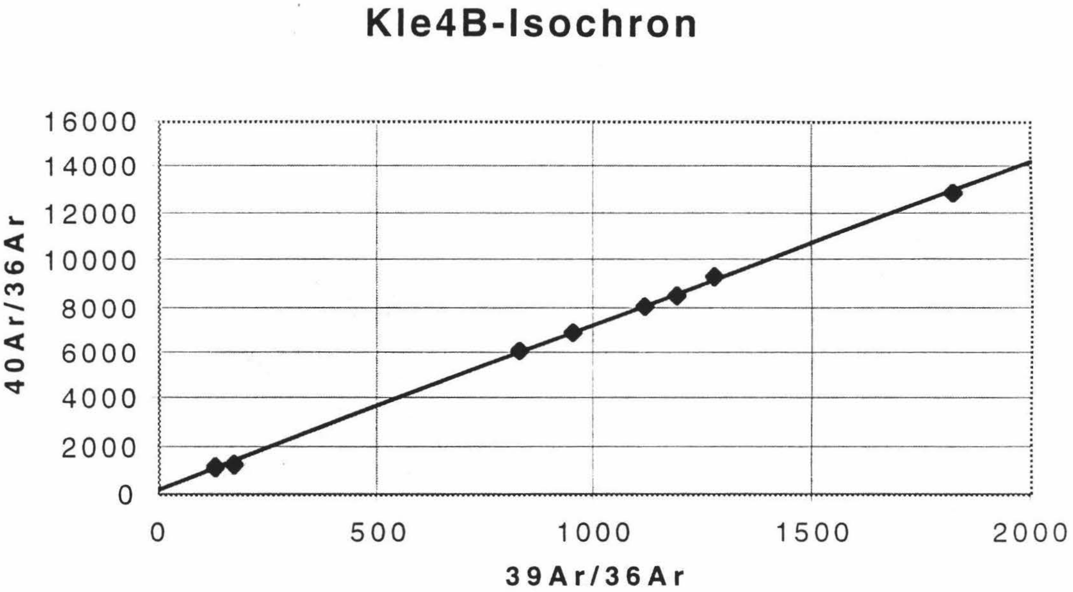

Figure 18. Spectrum and isochron plots for sample Kle4B (J21)

Table 8. Ar-diffusion data for sample Klep5H (J22)

step	T (C)	t (min)	$^{40}Ar/^{39}Ar$	$^{38}Ar/^{39}Ar$	$^{37}Ar/^{39}Ar$	$^{36}Ar/^{39}Ar$	^{39}Ar (mol)	$\Sigma^{39}Ar$	$^{36}Ar/^{40}Ar$	Cl/K
1	750	10	7.943	2.68E-02	1.32E-01	4.30E-03	3.57E-14	10.9	5.39E-04	3.61E-03
2	800	10	8.112	2.64E-02	2.55E-01	4.61E-03	1.49E-14	15.5	5.62E-04	3.48E-03
3	850	10	8.177	2.90E-02	6.45E-01	5.07E-03	8.33E-15	18.0	6.02E-04	4.18E-03
4	900	10	8.213	3.56E-02	1.31E+00	5.02E-03	9.37E-15	20.9	5.73E-04	6.03E-03
5	950	10	7.713	7.78E-02	3.21E+00	3.32E-03	1.86E-14	26.5	3.27E-04	1.79E-02
6	1000	10	8.050	2.57E-01	6.47E+00	4.63E-03	7.99E-14	50.9	3.75E-04	6.77E-02
7	1025	10	7.296	2.49E-01	5.43E+00	1.88E-03	5.30E-14	67.2	7.16E-05	6.57E-02
8	1050	10	7.654	1.55E-01	3.95E+00	3.50E-03	1.63E-14	72.1	3.29E-04	3.93E-02
9	1150	10	7.506	2.36E-01	6.82E+00	3.22E-03	6.90E-14	93.2	2.02E-04	6.20E-02
10	1300	10	9.468	2.87E-01	7.55E+00	1.01E-02	2.23E-14	100	8.67E-04	7.58E-02

step	$\%^{40}Ar^*$	$^{40}Ar^*/^{39}Ar_K$	$\pm\sigma_{40/39}$	Age (Ma)	$\pm\sigma_{Age}$ (an)	$1/\sigma_{Age}^2$	(Age-Mean Age)^2	$^{39}Ar_K/^{40}Ar$	$\pm\sigma_{39/40}$	$\pm\sigma_{36/40}$
1	83.5	6.659	0.052	81.1	0.6	2.6500	23.6822	1.26E-01	1.20E-04	2.18E-05
2	82.4	6.746	0.118	82.2	1.4	0.5077	14.6256	1.24E-01	3.39E-04	4.85E-05
3	80.7	6.706	0.202	81.7	2.4	0.1734	18.5606	1.23E-01	7.54E-04	8.11E-05
4	81.7	6.808	0.192	82.9	2.3	0.1909	9.5594	1.22E-01	5.41E-04	7.80E-05
5	89.4	6.961	0.087	84.7	1.0	0.9370	1.5978	1.30E-01	3.26E-04	3.72E-05
6	88.5	7.168	0.026	87.2	0.3	10.4278	1.4143	1.24E-01	1.02E-04	1.06E-05
7	97.3	7.145	0.032	86.9	0.4	6.7277	0.8328	1.37E-01	1.50E-04	1.46E-05
8	89.2	6.906	0.107	84.0	1.3	0.6151	3.7143	1.31E-01	4.83E-04	4.58E-05
9	93.5	7.068	0.026	86.0	0.3	10.7727	0.0000	1.33E-01	1.17E-04	1.12E-05
10	73.8	7.061	0.113	85.9	1.3	0.5548	0.0065	1.05E-01	5.48E-04	3.65E-05
	Total Gas Age	**7.014**	**0.057**	**85.3**		**J-Factor**	**0.006906**			

step	$\pm\sigma_{Cl/K}$	Ca/K	$\pm\sigma_{Ca/K}$
1	8.40E-05	2.67E-01	2.65E-02
2	1.14E-04	5.15E-01	5.11E-02
3	3.40E-04	1.30E+00	1.29E-01
4	2.56E-04	2.65E+00	2.62E-01
5	1.45E-04	6.51E+00	6.45E-01
6	1.16E-04	1.31E+01	1.30E+00
7	1.95E-04	1.10E+01	1.09E+00
8	4.02E-04	8.00E+00	7.92E-01
9	3.08E-04	1.38E+01	1.37E+00
10	4.01E-04	1.53E+01	1.52E+00

Weighted	Mean	Age (Ma)	**86.0**
	Standard	Error (Ma)	**0.2**
		MSWD	**9.9**
Adjusted	Standard	Error (Ma)	**0.5**

***** INVERSE ISOCHRON PARAMETERS *****

ISOCHRON AGE (Ma): 86.29475
UNCERTAINTY: .3249565
TRAPPED 40Ar/36Ar: 283.572
UNCERTAINTY 10.42342
SAMPLE 40Ar*/39Ar: 7.094649
UNCERTAINTY 2.736007E-02

***** NEW YORK REGRESSION PARAMETERS *****

SLOPE: -2.501886E-02
UNCERTAINTY: 1.003909E-03
Y-INT: 3.526441E-03
UNCERTAINTY: 1.296234E-04
X-INT: .1409513
UNCERTAINTY 5.4357E-04
SWD: 12.36785

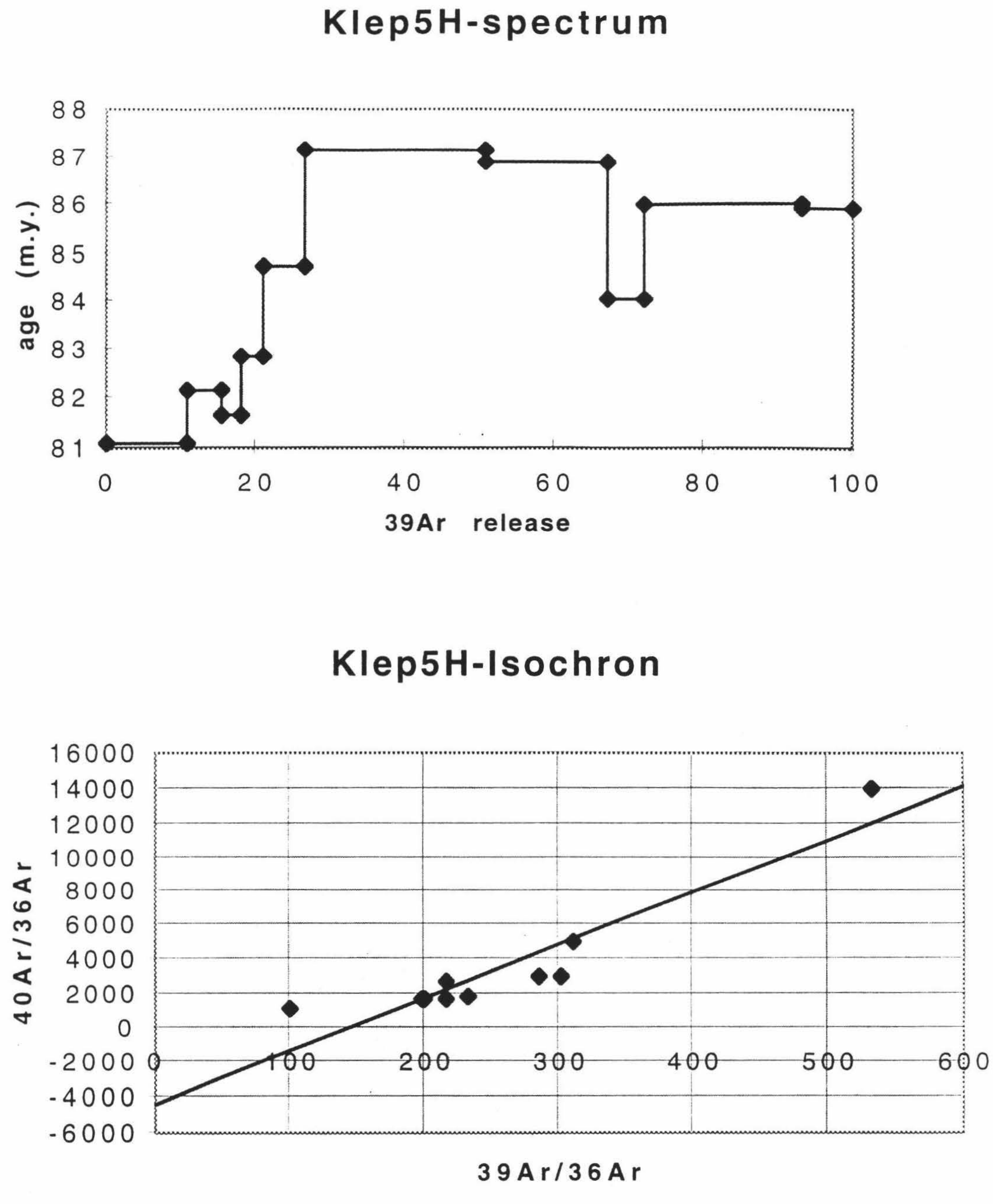

Figure 19. Spectrum and isochron plots for sample Klep5H (J22)

Table 9. Ar-diffusion data for sample Klep5B (J23)

step	T (C)	t (min)	^{40}Ar/^{39}Ar	^{38}Ar/^{39}Ar	^{37}Ar/^{39}Ar	^{36}Ar/^{39}Ar	^{39}Ar (mol)	Σ^{39}Ar	^{36}Ar/^{40}Ar	Cl/K
1	600	10	10.34	4.31E-02	2.49E-02	1.74E-02	8.04E-15	0.535	1.63E-03	7.18E-03
2	650	10	8.394	2.64E-02	8.29E-03	6.61E-03	4.48E-13	30.4	7.64E-04	3.21E-03
3	700	10	6.802	2.42E-02	3.46E-03	4.25E-04	2.00E-13	43.7	6.06E-05	2.93E-03
4	750	10	6.963	2.46E-02	1.45E-02	6.70E-04	6.37E-14	48.0	9.29E-05	3.02E-03
5	800	10	6.984	2.49E-02	1.52E-02	9.22E-04	7.76E-14	53.1	1.28E-04	3.10E-03
6	950	10	6.918	2.40E-02	1.24E-02	9.42E-04	2.32E-13	68.6	1.32E-04	2.84E-03
7	950	10	6.796	2.37E-02	1.09E-02	4.55E-04	2.84E-13	87.5	6.46E-05	2.79E-03
8	1150	10	7.390	2.47E-02	8.61E-02	1.19E-03	1.87E-13	100	1.54E-04	3.01E-03

step	%^{40}Ar*	^{40}Ar*/^{39}Ar$_K$	$\pm\sigma_{40/39}$	Age (Ma)	$\pm\sigma_{Age}$ (an)	$1/\sigma_{Age}^2$	(Age-Mean Age)^2	^{39}Ar$_K$/^{40}Ar	$\pm\sigma_{39/40}$	$\pm\sigma_{36/40}$
1	49.6	5.182	0.136	63.4	1.6	0.37528	312.23192	9.69E-02	6.38E-04	3.91E-05
2	76.4	6.415	0.016	78.2	0.2	27.70159	8.42465	1.19E-01	2.57E-04	5.68E-06
3	97.7	6.651	0.007	81.0	0.1	138.37359	0.00797	1.48E-01	3.30E-04	1.59E-06
4	96.6	6.741	0.016	82.1	0.2	25.96669	0.95589	1.44E-01	3.87E-04	5.22E-06
5	95.6	6.688	0.016	81.4	0.2	27.51937	0.11842	1.44E-01	3.88E-04	4.76E-06
6	95.6	6.615	0.009	80.6	0.1	93.81386	0.27199	1.45E-01	3.35E-04	2.01E-06
7	97.6	6.638	0.008	80.8	0.1	101.61043	0.06422	1.48E-01	3.45E-04	1.38E-06
8	94.9	7.019	0.015	85.4	0.2	32.51594	18.32803	1.36E-01	3.69E-04	2.82E-06
	Total Gas Age	**6.616**	**0.013**	**80.6**	**0.2**		**J-Factor**	**0.006904**		

step	$\pm\sigma_{Cl/K}$	Ca/K	$\pm\sigma_{Ca/K}$
1	1.70E-04	4.89E-02	4.99E-03
2	3.29E-05	1.63E-02	1.61E-03
3	4.86E-05	6.79E-03	6.78E-04
4	5.60E-05	2.85E-02	2.83E-03
5	5.49E-05	2.99E-02	2.96E-03
6	7.96E-05	2.43E-02	2.41E-03
7	1.67E-05	2.14E-02	2.13E-03
8	9.35E-05	1.69E-01	1.67E-02

Weighted	Mean	Age (Ma)	**81.09**
	Standard	Error (Ma)	**0.05**
		MSWD	**144.0**
Adjusted	Standard	Error (Ma)	**0.6**

***** NEW YORK REGRESSION PARAMETERS *****

SLOPE: -2.622265E-02

UNCERTAINTY: 2.646753E-04

Y-INT: 3.910941E-03

UNCERTAINTY: 3.776169E-05

X-INT: .1491436

UNCERTAINTY 1.046628E-04

SWD: 152.0557

***** INVERSE ISOCHRON PARAMETERS *****

ISOCHRON AGE (Ma): 81.63717

UNCERTAINTY: 5.601271E-02

TRAPPED 40Ar/36Ar: 255.693

UNCERTAINTY 2.468817

SAMPLE 40Ar*/39Ar: 6.704947

UNCERTAINTY 4.705255E-03

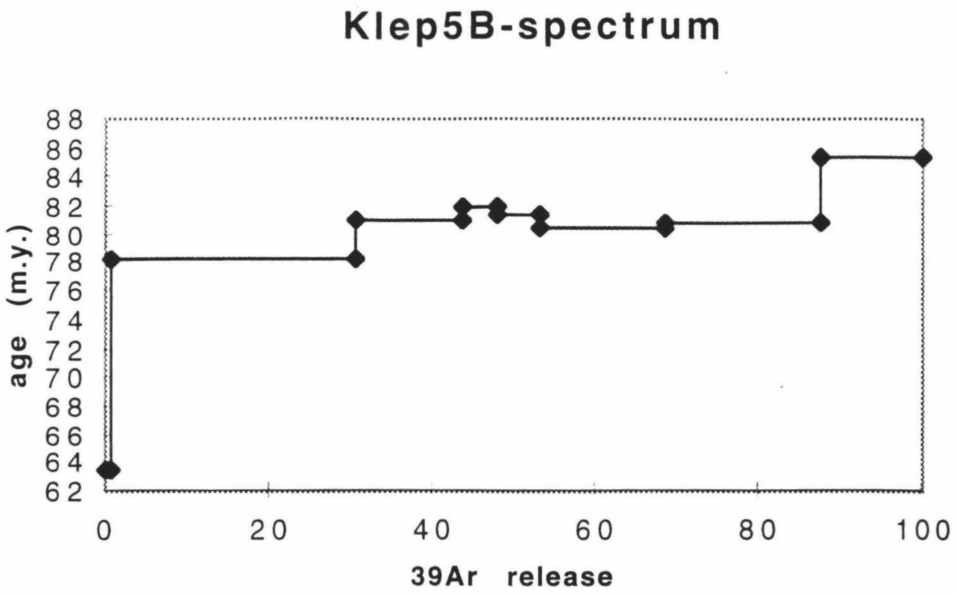
Klep5B-spectrum

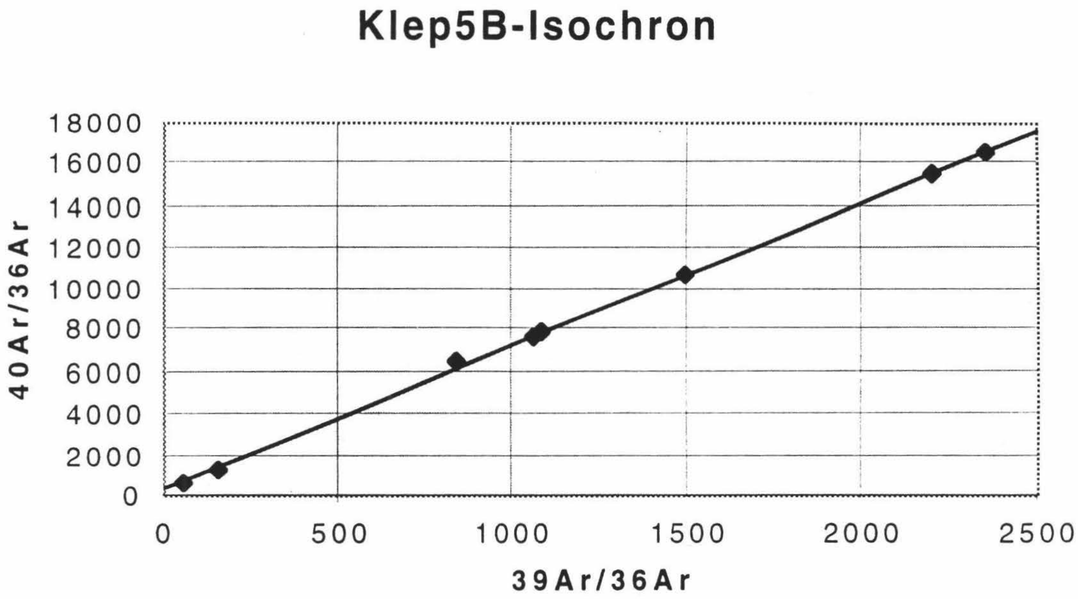
Klep5B-Isochron

Figure 20. Spectrum and isochron plots for sample Klep5B (J23)

Table 10. Ar-diffusion data for sample KI2H (J24)

step	T (C)	t (min)	$^{40}Ar/^{39}Ar$	$^{38}Ar/^{39}Ar$	$^{37}Ar/^{39}Ar$	$^{36}Ar/^{39}Ar$	^{39}Ar (mol)	$\Sigma^{39}Ar$	$^{36}Ar/^{40}Ar$	Cl/K
1	750	10	12.70	6.64E-02	1.03E+00	2.07E-02	4.23E-15	1.79	1.61E-03	1.37E-02
2	850	10	10.12	7.73E-02	3.21E+00	1.27E-02	3.56E-15	3.30	1.18E-03	1.72E-02
3	950	10	8.746	4.39E-01	9.81E+00	7.54E-03	3.17E-14	16.7	5.84E-04	1.19E-01
4	980	10	7.689	5.65E-01	7.42E+00	2.53E-03	7.93E-14	50.2	8.85E-05	1.54E-01
5	1010	10	8.280	5.40E-01	7.73E+00	4.62E-03	2.41E-14	60.4	3.26E-04	1.47E-01
6	1050	10	8.806	5.46E-01	8.66E+00	7.05E-03	1.77E-14	67.9	5.56E-04	1.48E-01
7	1150	10	8.082	5.52E-01	8.16E+00	4.05E-03	4.62E-14	87.4	2.50E-04	1.50E-01
8	1300	10	9.706	6.01E-01	8.82E+00	9.56E-03	2.98E-14	100	7.59E-04	1.64E-01

step	$\%^{40}Ar^*$	$^{40}Ar^*/^{39}Ar_K$	$\pm\sigma_{40/39}$	Age (Ma)	$\pm\sigma_{Age}$ (an)	$1/\sigma_{Age}^2$	$(Age\text{-}Mean\ Age)^2$	$^{39}Ar_K/^{40}Ar$	$\pm\sigma_{39/40}$	$\pm\sigma_{36/40}$
1	51.8	6.645	0.371	80.9	4.4	0.05134	9.77E+01	7.88E-02	4.19E-04	9.76E-05
2	64.1	6.585	0.412	80.2	4.9	0.04146	1.12E+02	9.88E-02	5.03E-04	1.37E-04
3	82.4	7.267	0.058	88.3	0.7	2.12769	6.21E+00	1.14E-01	1.55E-04	2.18E-05
4	97.0	7.502	0.024	91.1	0.3	12.51982	8.63E-02	1.30E-01	1.49E-04	9.74E-06
5	89.9	7.502	0.068	91.1	0.8	1.56473	8.20E-02	1.20E-01	2.86E-04	2.63E-05
6	83.1	7.383	0.094	89.7	1.1	0.81371	1.25E+00	1.13E-01	3.07E-04	3.47E-05
7	92.2	7.506	0.044	91.1	0.5	3.73739	1.15E-01	1.23E-01	2.33E-04	1.71E-05
8	77.2	7.556	0.061	91.7	0.7	1.91077	8.56E-01	1.03E-01	1.71E-04	2.05E-05
	Total Gas Age	**7.440**	**0.059**	**90.3**	**0.7**		**J-Factor**	**0.006901**		

step	$\pm\sigma_{Cl/K}$	Ca/K	$\pm\sigma_{Ca/K}$
1	3.81E-04	2.07E+00	2.06E-01
2	4.87E-04	6.50E+00	6.44E-01
3	5.34E-04	2.00E+01	1.98E+00
4	3.01E-04	1.51E+01	1.49E+00
5	5.74E-04	1.57E+01	1.56E+00
6	4.68E-04	1.76E+01	1.74E+00
7	4.23E-04	1.66E+01	1.64E+00
8	6.05E-04	1.79E+01	1.78E+00

Weighted	Mean	Age (Ma)	**90.8**
	Standard	Error (Ma)	**0.2**
		MSWD	**3.9**
Adjusted	Standard	Error (Ma)	**0.4**

***** INVERSE ISOCHRON PARAMETERS *****

ISOCHRON AGE (Ma):	91.15575
UNCERTAINTY:	.2767482
TRAPPED 40Ar/36Ar:	281.0299
UNCERTAINTY	7.181887
SAMPLE 40Ar*/39Ar:	7.509915
UNCERTAINTY	2.338092E-02

***** NEW YORK REGRESSION PARAMETERS *****

SLOPE:	-2.672283E-02
UNCERTAINTY:	7.430905E-04
Y-INT:	3.55834E-03
UNCERTAINTY:	9.093551E-05
X-INT:	.1331573
UNCERTAINTY	4.145639E-04
SWD:	3.977941

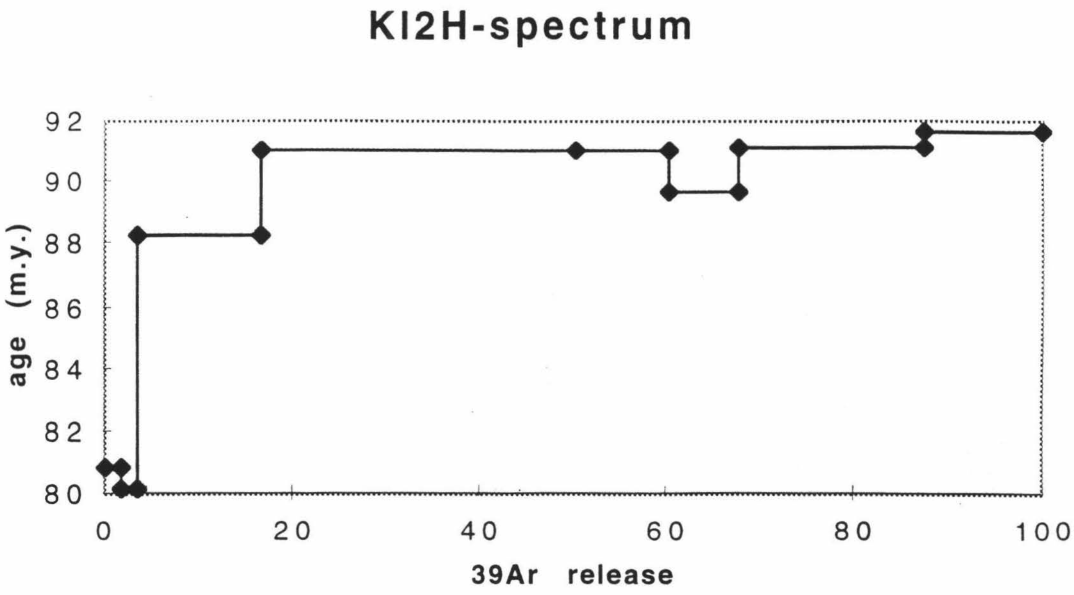

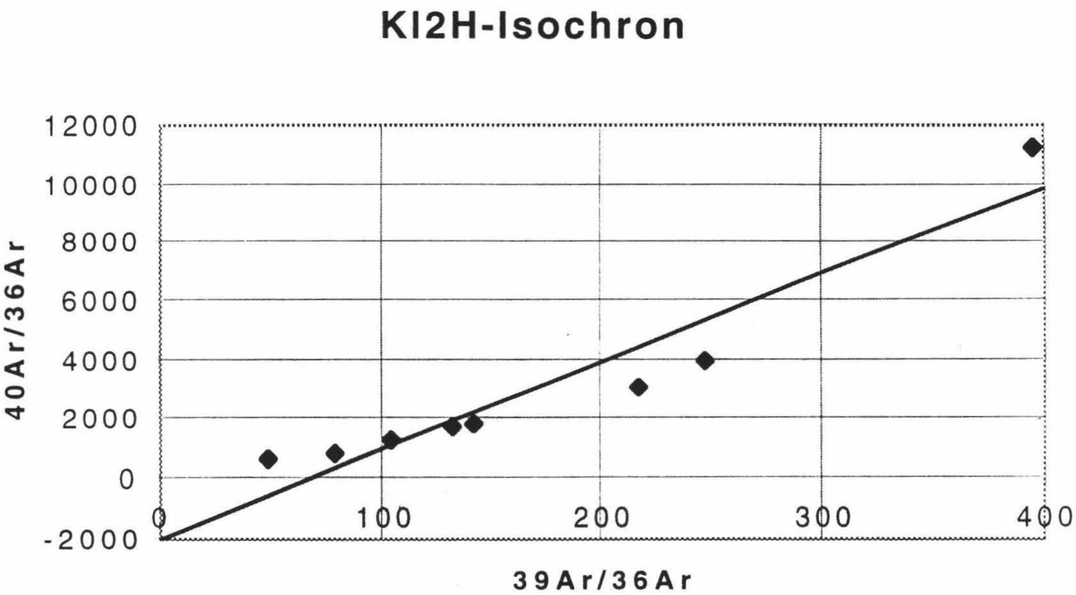

Figure 21. Spectrum and isochron plots for sample KI2H (J24)

Table 11. Ar-diffusion data for sample Kl2B (J25)

step	T (C)	t (min)	^{40}Ar/^{39}Ar	^{38}Ar/^{39}Ar	^{37}Ar/^{39}Ar	^{36}Ar/^{39}Ar	^{39}Ar (mol)	Σ^{39}Ar	^{36}Ar/^{40}Ar	Cl/K
1	600	11	10.52	4.02E-02	1.74E-02	1.86E-02	9.48E-14	5.01	1.77E-03	6.56E-03
2	700	13	7.978	3.37E-02	4.92E-03	5.11E-03	3.29E-13	22.4	6.43E-04	5.46E-03
3	750	40	7.080	3.27E-02	2.82E-03	1.14E-03	4.29E-13	45.1	1.62E-04	5.38E-03
4	800	10	7.183	3.22E-02	1.03E-02	1.51E-03	4.97E-13	71.4	2.10E-04	5.25E-03
5	900	10	7.102	3.25E-02	3.70E-02	1.33E-03	2.91E-13	86.8	1.87E-04	5.33E-03
6	1000	10	7.361	3.28E-02	1.15E-01	2.20E-03	2.31E-13	99.0	2.96E-04	5.37E-03
7	1150	10	16.77	5.10E-02	1.18E+00	3.47E-02	1.85E-14	100	2.05E-03	8.74E-03

step	%^{40}Ar*	^{40}Ar*/^{39}Ar$_K$	$\pm\sigma_{40/39}$	Age (Ma)	$\pm\sigma_{Age}$ (an)	$1/\sigma_{Age}^2$	(Age-Mean Age)^2	^{39}Ar$_K$/^{40}Ar	$\pm\sigma_{39/40}$	$\pm\sigma_{36/40}$
1	47.5	4.999	0.047	61.2	0.6	3.1272	399.5827	9.53E-02	1.50E-04	1.45E-05
2	80.7	6.443	0.020	78.4	0.2	17.6236	7.3174	1.26E-01	1.49E-04	7.54E-06
3	94.8	6.717	0.008	81.7	0.1	105.8650	0.3082	1.42E-01	9.09E-05	3.27E-06
4	93.4	6.714	0.026	81.7	0.3	10.7137	0.2785	1.40E-01	4.85E-04	3.13E-06
5	94.1	6.687	0.008	81.4	0.1	110.8313	0.0392	1.41E-01	1.24E-04	2.42E-06
6	90.9	6.695	0.009	81.5	0.1	80.2447	0.0903	1.36E-01	1.38E-04	2.66E-06
7	39.2	6.591	0.150	80.2	1.8	0.3126	0.8820	5.97E-02	1.94E-04	2.91E-05
	Total Gas Age	**6.574**	**0.018**	**80.0**	**0.2**		**J-Factor**	**0.006898**		

step	$\pm\sigma_{Cl/K}$	Ca/K	$\pm\sigma_{Ca/K}$
1	4.72E-05	3.52E-02	3.50E-03
2	6.09E-05	9.95E-03	9.92E-04
3	2.98E-05	5.70E-03	5.69E-04
4	2.76E-05	2.09E-02	2.08E-03
5	2.43E-05	7.48E-02	7.41E-03
6	4.48E-05	2.33E-01	2.31E-02
7	1.32E-04	2.39E+00	2.37E-01

Weighted	Mean	Age (Ma)	**81.2**
	Standard	Error (Ma)	**0.1**
		MSWD	**237.7**
Adjusted	Standard	Error (Ma)	**0.9**

***** NEW YORK REGRESSION PARAMETERS *****

SLOPE: -2.933297E-02
UNCERTAINTY: 2.327964E-04
Y-INT: 4.320449E-03
UNCERTAINTY: 3.204319E-05
X-INT: .1472898
UNCERTAINTY 1.139307E-04
SWD: 121.7843

***** INVERSE ISOCHRON PARAMETERS *****

ISOCHRON AGE (Ma): 82.57127
UNCERTAINTY: 6.243043E-02
TRAPPED 40Ar/36Ar: 231.4574
UNCERTAINTY 1.716635
SAMPLE 40Ar*/39Ar: 6.789334
UNCERTAINTY 5.251645E-03

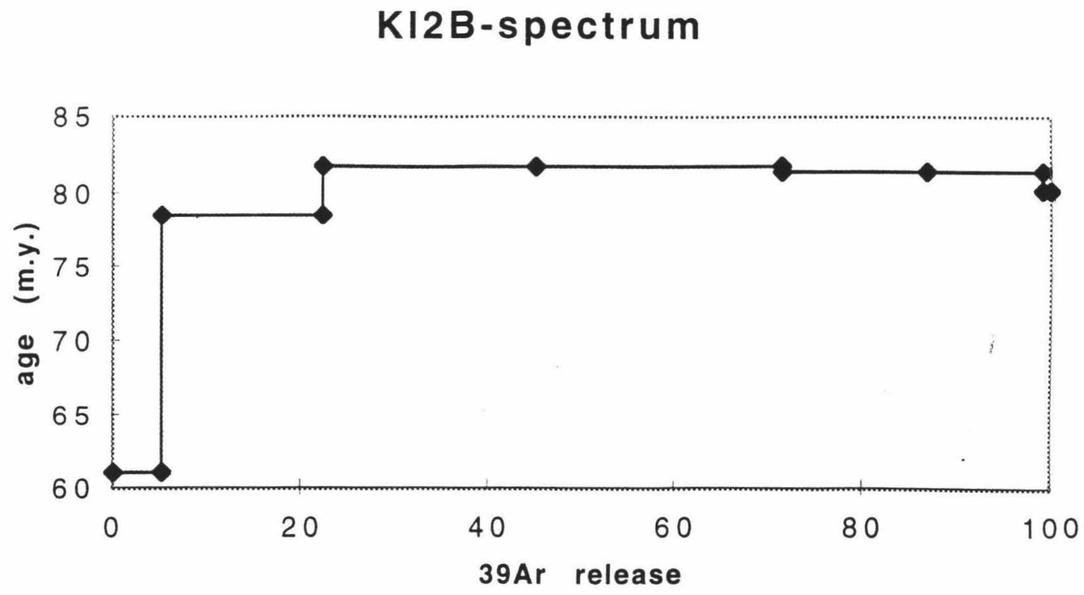
Kl2B-spectrum

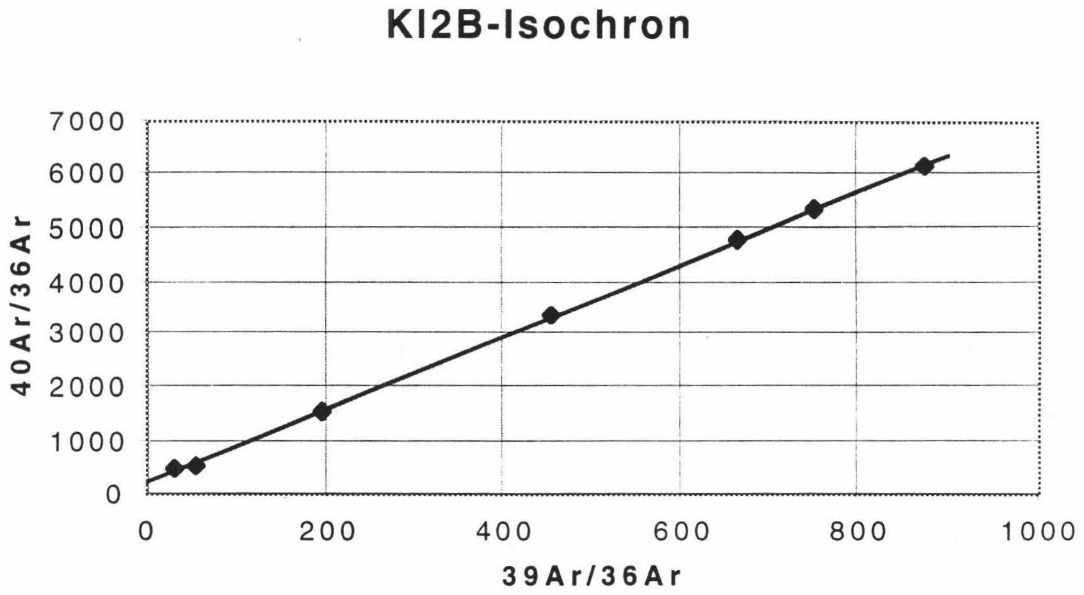
Kl2B-Isochron

Figure 22. Spectrum and isochron plots for sample Kl2B (J25)

Table 12. Ar-diffusion data for sample Kmr2H (J27)

step	T (C)	t (min)	^{40}Ar/^{39}Ar	^{38}Ar/^{39}Ar	^{37}Ar/^{39}Ar	^{36}Ar/^{39}Ar	^{39}Ar (mol)	Σ^{39}Ar	^{36}Ar/^{40}Ar	Cl/K
1	750	13	8.107	1.77E-02	8.14E-02	4.62E-03	4.45E-14	14.7	5.69E-04	1.06E-03
2	850	10	7.697	1.81E-02	3.16E-01	2.17E-03	2.15E-14	21.8	2.73E-04	1.30E-03
3	950	12	7.369	2.71E-02	1.10E+00	1.49E-03	5.51E-14	40.0	1.65E-04	3.84E-03
4	980	10	7.476	7.53E-02	4.09E+00	2.73E-03	3.58E-14	51.8	2.30E-04	1.72E-02
5	1010	10	7.306	1.35E-01	5.20E+00	2.26E-03	6.32E-14	72.6	1.31E-04	3.39E-02
6	1050	13	7.394	1.20E-01	3.97E+00	2.32E-03	3.05E-14	82.7	1.80E-04	2.97E-02
7	1150	12	8.179	1.60E-01	5.84E+00	5.58E-03	3.54E-14	94.4	5.05E-04	4.07E-02
8	1300	10	10.10	1.52E-01	6.61E+00	1.18E-02	1.71E-14	100	1.01E-03	3.83E-02

step	%^{40}Ar*	^{40}Ar*/^{39}Ar$_K$	$\pm\sigma_{40/39}$	Age (Ma)	$\pm\sigma_{Age}$ (an)	$1/\sigma_{Age}^2$	(Age-Mean Age)^2	^{39}Ar$_K$/^{40}Ar	$\pm\sigma_{39/40}$	$\pm\sigma_{36/40}$
1	82.7	6.724	0.037	81.7	0.4	5.08498	7.72707	1.24E-01	1.37E-04	1.52E-05
2	91.0	7.054	0.072	85.6	0.9	1.36985	1.30901	1.30E-01	3.53E-04	3.04E-05
3	94.5	6.991	0.032	84.9	0.4	7.05171	0.15168	1.36E-01	2.32E-04	1.34E-05
4	92.5	6.966	0.046	84.6	0.5	3.34271	0.00856	1.34E-01	2.19E-04	2.01E-05
5	95.6	7.024	0.028	85.3	0.3	9.17088	0.62178	1.37E-01	1.29E-04	1.25E-05
6	93.9	6.997	0.055	84.9	0.7	2.31359	0.22253	1.35E-01	2.29E-04	2.47E-05
7	84.5	6.966	0.051	84.6	0.6	2.71773	0.00861	1.22E-01	2.40E-04	2.01E-05
8	69.5	7.096	0.112	86.1	1.3	0.56980	2.70458	9.88E-02	1.91E-04	3.69E-05
	Total Gas Age	**6.964**	**0.045**	**84.5**	**0.5**		**J-Factor**	**0.006889**		

step	$\pm\sigma_{Cl/K}$	Ca/K	$\pm\sigma_{Ca/K}$
1	5.78E-05	1.64E-01	1.63E-02
2	1.62E-04	6.38E-01	6.32E-02
3	6.60E-05	2.22E+00	2.20E-01
4	2.17E-04	8.29E+00	8.20E-01
5	1.96E-04	1.05E+01	1.04E+00
6	1.15E-04	8.05E+00	7.97E-01
7	1.74E-04	1.18E+01	1.17E+00
8	2.39E-04	1.34E+01	1.33E+00

Weighted	Mean	Age (Ma)	**84.5**
	Standard	Error (Ma)	**0.2**
		MSWD	**7.1**
Adjusted	Standard	Error (Ma)	**0.5**

***** INVERSE ISOCHRON PARAMETERS *****

ISOCHRON AGE (Ma): 85.08184
UNCERTAINTY: .2625859
TRAPPED 40Ar/36Ar: 271.7375
UNCERTAINTY 7.835461
SAMPLE 40Ar*/39Ar: 7.009817
UNCERTAINTY 2.214837E-02

***** NEW YORK REGRESSION PARAMETERS *****

SLOPE: -2.579628E-02
UNCERTAINTY: 8.091498E-04
Y-INT: 3.680022E-03
UNCERTAINTY: 1.061122E-04
X-INT: .1426571
UNCERTAINTY 4.507425E-04
SWD: 7.137449

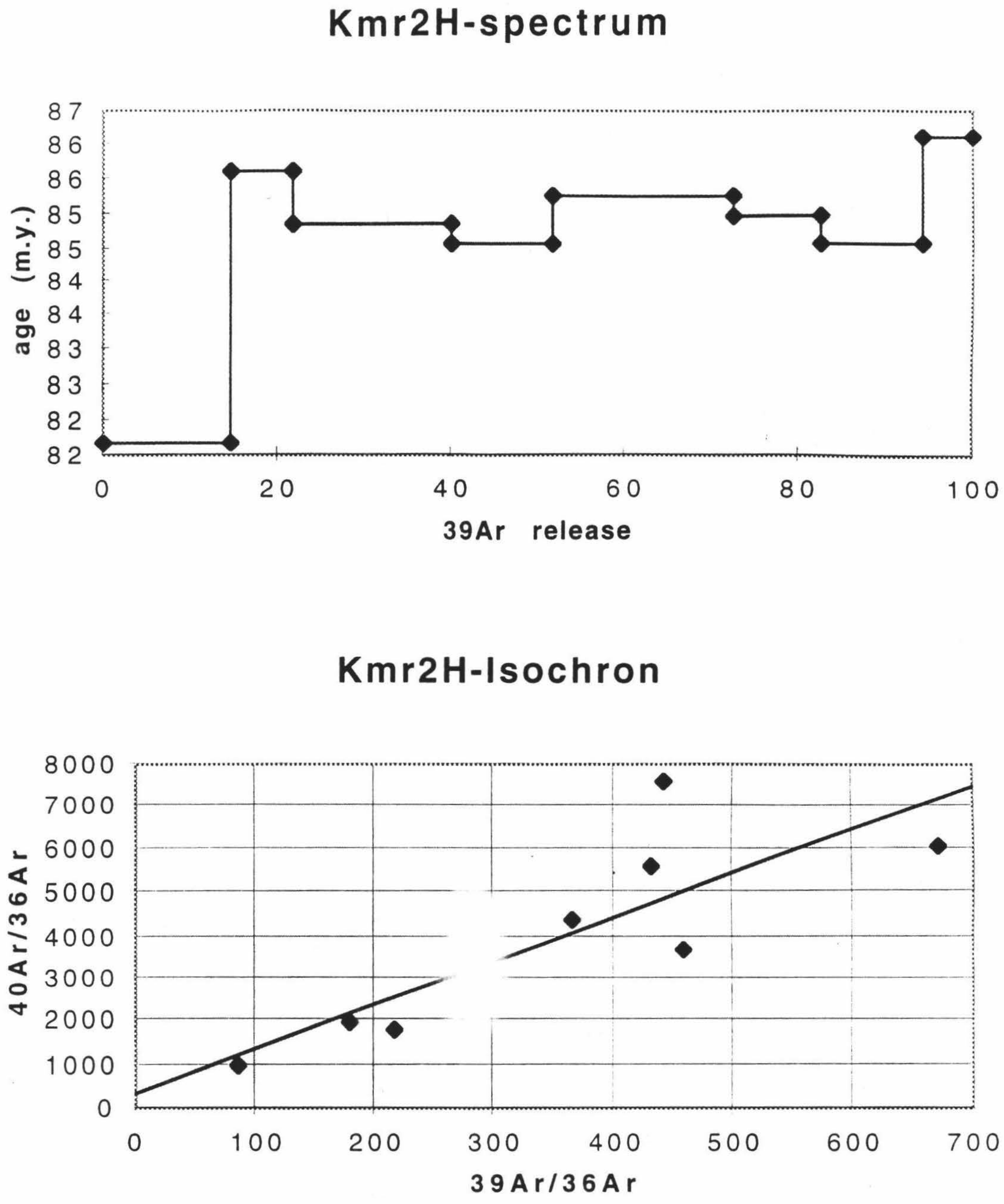

Figure 23. Spectrum and isochron plots for sample Kmr2H (J27)

Table 13. Ar-diffusion data for sample Kmr2B (J28)

step	T (C)	t (min)	^{40}Ar/^{39}Ar	^{38}Ar/^{39}Ar	^{37}Ar/^{39}Ar	^{36}Ar/^{39}Ar	^{39}Ar (mol)	Σ^{39}Ar	^{36}Ar/^{40}Ar	Cl/K
1	700	10	7.945	1.77E-02	6.81E-03	4.98E-03	3.63E-13	26.2	6.28E-04	1.04E-03
2	750	10	6.843	1.49E-02	3.83E-03	2.37E-04	4.12E-13	55.9	3.47E-05	5.09E-04
3	800	10	6.856	1.46E-02	7.28E-03	4.12E-04	1.47E-13	66.5	6.00E-05	4.30E-04
4	850	10	6.964	1.53E-02	9.97E-03	5.23E-04	1.85E-13	79.9	7.50E-05	6.06E-04
5	900	10	6.854	1.48E-02	6.43E-03	3.82E-04	1.65E-13	91.7	5.57E-05	4.84E-04
6	1150	10	7.032	1.53E-02	6.34E-03	4.58E-04	1.15E-13	100	6.51E-05	6.07E-04

step	%^{40}Ar*	^{40}Ar*/^{39}Ar$_K$	$\pm\sigma_{40/39}$	Age (Ma)	$\pm\sigma_{Age}$ (an)	$1/\sigma_{Age}^2$	(Age-Mean Age)^2	^{39}Ar$_K$/^{40}Ar	$\pm\sigma_{39/40}$	$\pm\sigma_{36/40}$
1	81.2	6.450	0.015	78.4	0.2	32.5378	10.9201	1.26E-01	1.42E-04	5.06E-06
2	98.6	6.748	0.007	81.9	0.1	135.7716	0.0543	1.47E-01	1.42E-04	1.49E-06
3	97.8	6.710	0.007	81.5	0.1	155.4847	0.0487	1.46E-01	1.07E-04	2.25E-06
4	97.4	6.785	0.007	82.4	0.1	139.8401	0.4566	1.44E-01	1.22E-04	1.95E-06
5	97.9	6.717	0.007	81.5	0.1	137.3083	0.0194	1.46E-01	1.35E-04	1.72E-06
6	97.5	6.872	0.019	83.4	0.2	20.4774	2.8930	1.43E-01	3.00E-04	5.50E-06
	Total Gas Age	**6.678**	**0.010**	**81.1**	**0.1**		**J-Factor**	**0.006884**		

step	$\pm\sigma_{Cl/K}$	Ca/K	$\pm\sigma_{Ca/K}$
1	3.28E-05	1.38E-02	1.36E-03
2	1.50E-05	7.74E-03	7.68E-04
3	3.38E-05	1.47E-02	1.46E-03
4	4.26E-05	2.01E-02	2.00E-03
5	5.72E-05	1.30E-02	1.31E-03
6	2.31E-05	1.28E-02	1.32E-03

Weighted	Mean	Age (Ma)	**81.7**
	Standard	Error (Ma)	**0.04**
		MSWD	**99.2**
Adjusted	Standard	Error (Ma)	**0.4**

***** NEW YORK REGRESSION PARAMETERS *****

SLOPE: -2.891229E-02
UNCERTAINTY: 3.514662E-04
Y-INT: 4.272161E-03
UNCERTAINTY: 5.066358E-05
X-INT: .1477628
UNCERTAINTY 8.045222E-05
SWD: 41.24172

***** INVERSE ISOCHRON PARAMETERS *****

ISOCHRON AGE (Ma): 82.1496
UNCERTAINTY: 4.372482E-02
TRAPPED 40Ar/36Ar: 234.0736
UNCERTAINTY 2.77588
SAMPLE 40Ar*/39Ar: 6.767604
UNCERTAINTY 3.684749E-03

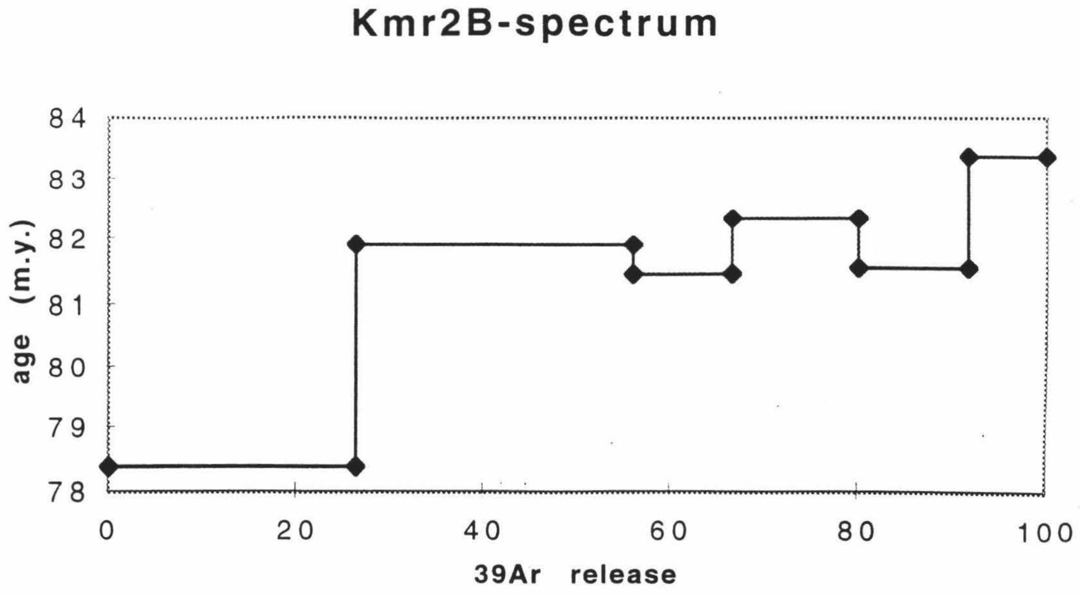

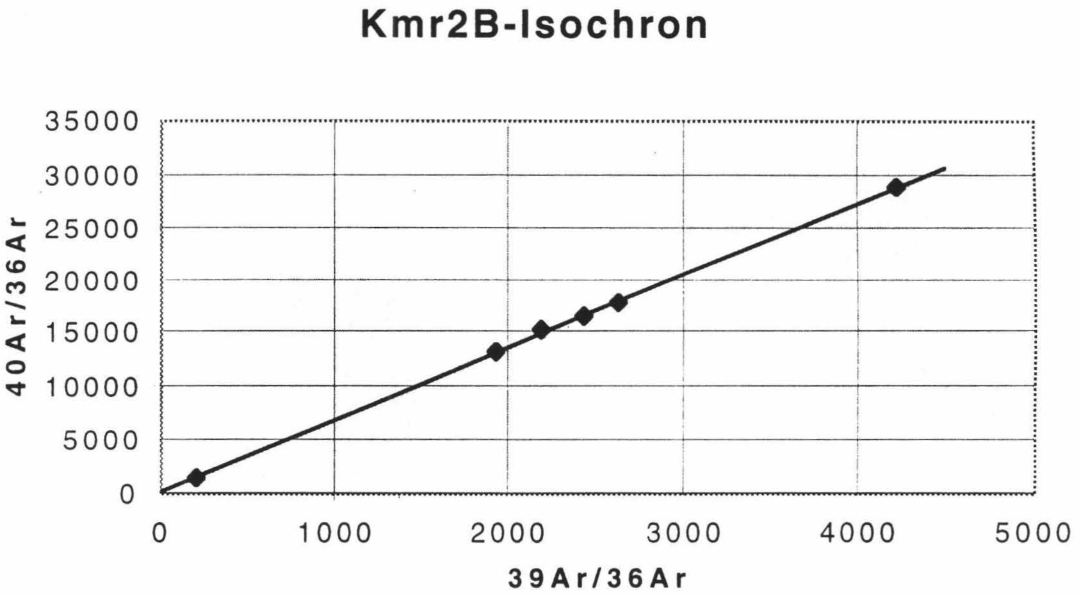

Figure 24. Spectrum and isochron plots for sample Kmr2B (J28)

Table 14. Ar-diffusion data for sample Kle1 (J30)

step	T (C)	t (min)	^{40}Ar/^{39}Ar	^{38}Ar/^{39}Ar	^{37}Ar/^{39}Ar	^{36}Ar/^{39}Ar	^{39}Ar (mol)	Σ^{39}Ar	%^{40}Ar*	^{40}Ar*/^{39}Ar$_K$	$\pm\sigma_{40/39}$
1	450	11	90.147	3.28E-01	3.64E-01	2.30E-01	6.24E-15	0.240	24.5	22.128	0.722
2	450	20	17.033	7.04E-02	2.83E-01	3.71E-02	2.96E-15	0.354	35.1	6.073	0.249
3	500	15	9.816	4.20E-02	3.05E-01	1.22E-02	9.93E-15	0.737	62.7	6.212	0.094
4	500	27	9.178	2.42E-02	3.30E-01	1.10E-02	9.09E-15	1.09	63.9	5.926	0.106
5	550	15	9.054	2.01E-02	3.98E-01	1.06E-02	2.32E-14	1.98	65.3	5.935	0.056
6	550	21	7.145	1.46E-02	3.92E-01	4.32E-03	1.78E-14	2.66	81.7	5.875	0.044
7	600	17	7.477	1.56E-02	4.45E-01	4.97E-03	4.27E-14	4.31	80.3	6.018	0.039
8	600	21	8.260	1.54E-02	4.60E-01	7.95E-03	3.36E-14	5.60	71.5	5.923	0.049
9	650	15	10.056	1.96E-02	7.92E-01	1.41E-02	6.67E-14	8.17	58.9	5.931	0.044
10	650	15	6.223	1.23E-02	5.80E-01	6.83E-04	4.30E-14	9.83	96.7	6.042	0.015
11	700	12	6.412	1.28E-02	7.43E-01	1.17E-03	9.26E-14	13.4	94.9	6.099	0.010
12	700	15	6.182	1.21E-02	6.72E-01	5.59E-04	5.29E-14	15.4	97.5	6.045	0.016
13	750	12	6.317	1.23E-02	8.16E-01	9.32E-04	8.64E-14	18.8	96.1	6.081	0.009
14	750	20	6.218	1.20E-02	7.50E-01	6.78E-04	6.57E-14	21.3	97.1	6.051	0.011
15	800	12	6.471	1.29E-02	8.35E-01	1.31E-03	7.29E-14	24.1	94.4	6.125	0.014
16	825	15	6.373	1.23E-02	7.56E-01	1.11E-03	8.18E-14	27.2	95.2	6.078	0.011
17	850	15	6.448	1.26E-02	6.47E-01	1.21E-03	7.85E-14	30.3	94.6	6.115	0.010
18	875	15	6.503	1.27E-02	5.40E-01	1.38E-03	6.62E-14	32.8	93.8	6.111	0.013
19	900	15	6.424	1.26E-02	4.27E-01	1.00E-03	5.96E-14	35.1	95.3	6.137	0.012
20	925	15	6.487	1.29E-02	3.37E-01	1.18E-03	6.22E-14	37.5	94.4	6.139	0.016
21	950	10	6.537	1.28E-02	2.74E-01	1.29E-03	5.54E-14	39.6	93.9	6.152	0.015
22	975	16	6.630	1.36E-02	2.71E-01	1.55E-03	6.73E-14	42.2	92.9	6.169	0.016
23	1000	15	6.746	1.42E-02	2.82E-01	1.85E-03	7.38E-14	45.1	91.7	6.196	0.015
24	1025	15	6.896	1.45E-02	2.75E-01	2.04E-03	8.82E-14	48.5	91.1	6.290	0.017
25	1050	20	7.023	1.55E-02	2.69E-01	2.09E-03	1.18E-13	53.0	91.1	6.402	0.012
26	1075	16	7.073	1.59E-02	2.65E-01	2.02E-03	1.06E-13	57.1	91.4	6.472	0.013
27	1100	18	7.151	1.60E-02	2.45E-01	2.02E-03	1.20E-13	61.7	91.4	6.547	0.011
28	1100	29	7.281	1.61E-02	2.40E-01	2.34E-03	1.24E-13	66.5	90.3	6.585	0.014
29	1100	44	7.503	1.68E-02	2.73E-01	3.23E-03	1.41E-13	71.9	87.2	6.546	0.022
30	1100	65	7.730	1.76E-02	3.00E-01	4.17E-03	1.34E-13	77.1	83.9	6.496	0.021
31	1100	67	8.023	1.75E-02	3.39E-01	5.02E-03	1.04E-13	81.1	81.4	6.542	0.025
32	1200	10	6.993	1.55E-02	2.13E-01	1.59E-03	2.71E-13	91.5	93.1	6.515	0.009
33	1225	14	8.210	2.11E-02	7.51E-01	5.40E-03	1.01E-13	95.4	80.9	6.650	0.032
34	1250	10	10.532	3.35E-02	1.97E+00	1.25E-02	2.80E-14	96.5	65.9	6.972	0.073
35	1300	17	10.604	3.20E-02	1.65E+00	1.30E-02	6.33E-14	98.9	64.7	6.881	0.055
36	1350	10	14.746	4.65E-02	2.46E+00	2.68E-02	2.81E-14	100	47.4	7.009	0.121

Table 14. (Continued) Ar-diffusion data for sample Kle1 (J30)

step	Age (Ma)	$\pm\sigma_{Age}$ (an)	$^{39}Ar_K/^{40}Ar$	$\pm\sigma_{39/40}$	$^{36}Ar/^{40}Ar$	$\pm\sigma_{36/40}$	Cl/K	$\pm\sigma_{Cl/K}$	Ca/K	$\pm\sigma_{Ca/K}$
1	255.1	7.8	1.11E-02	2.35E-05	2.55E-03	2.67E-05	7.54E-02	6.27E-04	7.35E-01	7.28E-02
2	73.7	3.0	5.88E-02	3.17E-04	2.18E-03	4.76E-05	1.40E-02	6.64E-04	5.73E-01	5.72E-02
3	75.3	1.1	1.02E-01	3.51E-04	1.24E-03	3.06E-05	7.40E-03	2.87E-04	6.16E-01	6.10E-02
4	71.9	1.3	1.09E-01	4.03E-04	1.19E-03	3.74E-05	2.53E-03	1.42E-04	6.68E-01	6.62E-02
5	72.0	0.7	1.11E-01	1.62E-04	1.16E-03	2.03E-05	1.42E-03	1.08E-04	8.04E-01	7.97E-02
6	71.3	0.5	1.40E-01	5.48E-04	5.93E-04	1.61E-05	2.15E-04	5.23E-05	7.92E-01	7.84E-02
7	73.0	0.5	1.34E-01	1.71E-04	6.52E-04	1.74E-05	4.70E-04	7.61E-05	8.99E-01	8.91E-02
8	71.9	0.6	1.21E-01	2.72E-04	9.51E-04	1.88E-05	2.60E-04	5.82E-05	9.30E-01	9.22E-02
9	72.0	0.5	9.96E-02	1.02E-04	1.38E-03	1.46E-05	1.11E-03	6.81E-05	1.60E+00	1.58E-01
10	73.3	0.2	1.61E-01	1.50E-04	8.68E-05	7.61E-06	-2.10E-04	4.92E-05	1.17E+00	1.16E-01
11	74.0	0.1	1.56E-01	1.29E-04	1.54E-04	4.20E-06	-9.83E-05	2.55E-05	1.50E+00	1.49E-01
12	73.3	0.2	1.62E-01	3.37E-04	6.35E-05	5.28E-06	-2.65E-04	6.22E-05	1.36E+00	1.34E-01
13	73.8	0.1	1.59E-01	1.90E-04	1.16E-04	2.95E-06	-2.19E-04	2.41E-05	1.65E+00	1.63E-01
14	73.4	0.1	1.61E-01	1.76E-04	7.91E-05	4.56E-06	-3.08E-04	5.04E-05	1.52E+00	1.50E-01
15	74.3	0.2	1.55E-01	1.95E-04	1.71E-04	5.76E-06	-7.26E-05	2.85E-05	1.69E+00	1.67E-01
16	73.7	0.1	1.57E-01	1.58E-04	1.46E-04	4.76E-06	-2.42E-04	3.68E-05	1.53E+00	1.51E-01
17	74.2	0.1	1.56E-01	1.49E-04	1.64E-04	4.11E-06	-1.69E-04	3.62E-05	1.31E+00	1.29E-01
18	74.1	0.2	1.54E-01	1.54E-04	1.93E-04	5.75E-06	-1.47E-04	7.50E-05	1.09E+00	1.08E-01
19	74.4	0.1	1.56E-01	1.82E-04	1.40E-04	5.22E-06	-1.54E-04	2.29E-05	8.62E-01	8.53E-02
20	74.5	0.2	1.55E-01	1.94E-04	1.70E-04	6.95E-06	-9.62E-05	4.58E-05	6.81E-01	6.74E-02
21	74.6	0.2	1.54E-01	1.60E-04	1.88E-04	7.08E-06	-1.26E-04	4.41E-05	5.53E-01	5.48E-02
22	74.8	0.2	1.51E-01	2.72E-04	2.24E-04	5.19E-06	7.84E-05	7.16E-05	5.48E-01	5.43E-02
23	75.1	0.2	1.49E-01	2.42E-04	2.65E-04	4.95E-06	2.36E-04	6.30E-05	5.69E-01	5.64E-02
24	76.3	0.2	1.46E-01	2.63E-04	2.86E-04	5.41E-06	3.06E-04	2.73E-05	5.55E-01	5.50E-02
25	77.6	0.1	1.43E-01	1.50E-04	2.89E-04	4.78E-06	5.79E-04	4.18E-05	5.44E-01	5.39E-02
26	78.4	0.1	1.42E-01	1.11E-04	2.77E-04	5.43E-06	7.15E-04	5.65E-05	5.35E-01	5.29E-02
27	79.3	0.1	1.40E-01	1.39E-04	2.76E-04	4.30E-06	7.23E-04	2.38E-05	4.95E-01	4.90E-02
28	79.8	0.2	1.38E-01	1.93E-04	3.14E-04	4.57E-06	7.30E-04	4.45E-05	4.86E-01	4.81E-02
29	79.3	0.3	1.34E-01	2.39E-04	4.22E-04	7.73E-06	8.80E-04	1.88E-05	5.52E-01	5.46E-02
30	78.7	0.3	1.30E-01	1.06E-04	5.32E-04	8.98E-06	1.07E-03	3.22E-05	6.06E-01	6.00E-02
31	79.2	0.3	1.25E-01	1.79E-04	6.17E-04	9.35E-06	9.92E-04	4.37E-05	6.85E-01	6.79E-02
32	78.9	0.1	1.43E-01	9.54E-05	2.20E-04	3.93E-06	6.10E-04	1.19E-05	4.30E-01	4.26E-02
33	80.5	0.4	1.22E-01	1.19E-04	6.36E-04	1.27E-05	1.99E-03	9.85E-05	1.52E+00	1.50E-01
34	84.3	0.9	9.50E-02	2.52E-04	1.14E-03	2.18E-05	5.06E-03	2.25E-04	3.99E+00	3.95E-01
35	83.3	0.7	9.44E-02	1.24E-04	1.19E-03	1.72E-05	4.61E-03	9.81E-05	3.33E+00	3.30E-01
36	84.8	1.4	6.78E-02	1.53E-04	1.78E-03	2.70E-05	7.94E-03	1.81E-04	4.97E+00	4.92E-01

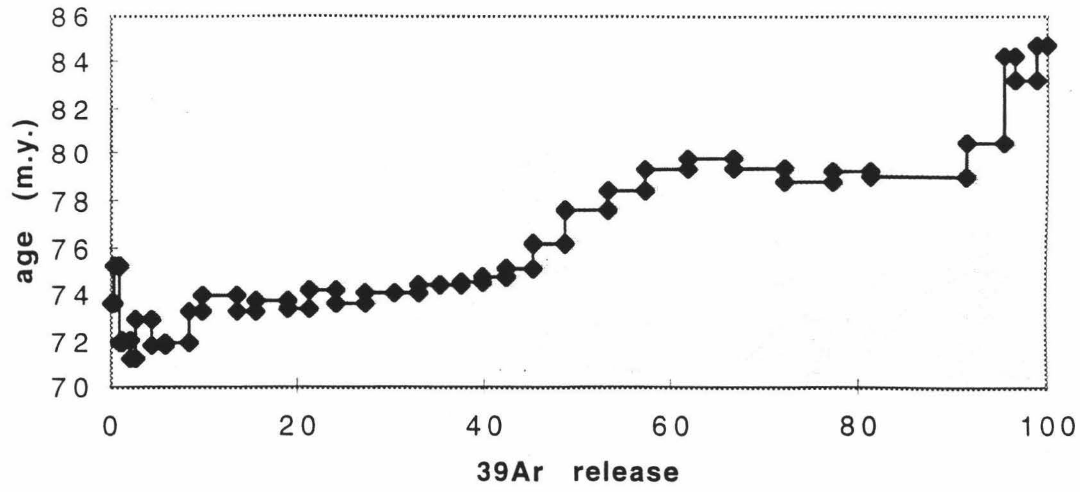

Kle1-spectrum

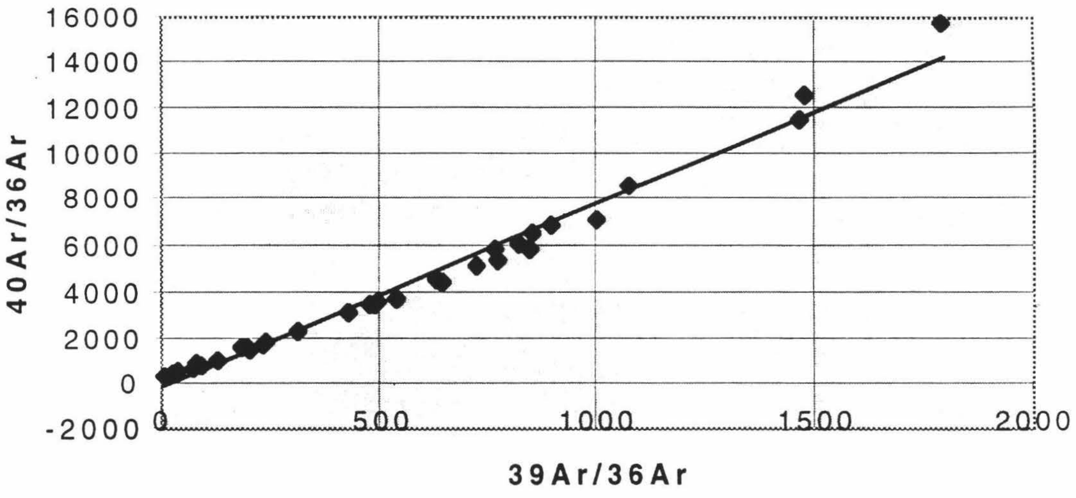

Kle1-Isochron

Figure 25. Spectrum and isochron plots for sample Kle1 (J30)

References

Ague, J. J. (1997) Thermodynamic calculation of emplacement pressures for batholithic rocks, California: Implications for the aluminum-in-hornblende barometer. *Geology*, **25**, 481-576.

Ague, J. J. and Brimhall, G. H. (1988) Magmatic arc asymmetry and distribution of anomalous plutonic belts in the batholiths of California: effects of assimilation, crustal thickness, and depth of crystallization. *Geological Society of America Bulletin*, **100**, 912-927.

Balk, R. (1937) Structural behavior of igneous rocks. *Geological Society of America Memoirs*, **5**, p. 177.

Bateman, P. C. (1992) Plutonism in the central part of the Sierra Nevada batholith, California. *U.S. Geological Survey Professional Paper* **1483**, p. 186.

Bateman, P. C. (1965) Geology and tungsten mineralization of the Bishop district, California. *U.S. Geological Survey Professional Paper* **470**, p. 208.

Bateman, P. C. and Wahrhaftig, C. (1966) Geology of the Sierra Nevada, ed. E. H. Bailey. *Geology of northern California: California Division of Mines and Geology Bulletin* **190**, 107-172.

Becker, G. F. (1892) The structure of a portion of the Sierra Nevada of California. *Geological Society of America Bulletin*, **2**, 49-74.

Bergantz, G. W. (1990) Melt fraction diagrams: The link between chemical and transport models. *Reviews in Mineralogy*, **24**, 239-257.

Bergbauer, S., Martel, S. J. and Hieronymus, C. F. (1998) Thermal stress evolution in cooling pluton environments of different geometries. *Geophysical Research Letters*, **25**, 707-710.

Best, M. G. (1982) *Igneous and Metamorphic Petrology*. W. H. Freeman and Company, San Francisco.

Bracewell, R. N. (1978) *The Fourier Transform and its Applications.* McGraw-Hill, Kogakusha.

Brudy, M., Zoback, M. D., Fuchs, K., Rummel, F. and Baumgärtner J. (1997) Estimation of the complete stress tensor to 8 km depth in the KTB scientific drill holes: Implications for crustal strength. *Journal of Geophysical Research*, **102**, 18,453-18,475.

Burnham, C. W. (1979) Magmas and Hydrothermal Fluids, ed. H. L. Barnes. *Geochemistry of Hydrothermal Ore Deposits*, John Wiley & Sons, New York, 71-136.

Bürgmann, R. and Pollard, D. D. (1994). Strain accommodation about strike-slip fault discontinuities in granitic rock under brittle-to-ductile conditions. *Journal of Structural Geology*, **16**, 1655-1674.

Carslaw, H. S. and Jaeger, J. C. (1959) *Conduction of heat in solids*. Clarendon Press, Oxford.

Carmichael, R. S. (1989) *Practical handbook of physical properties of rocks and minerals*. CRC Press, Boca Raton.

Christiansen, P. P. (1995) Faulting and hydrothermal processes in a granitic batholith. Stanford University Ph.D. thesis.

Devore, G. W. (1969) Differential thermal contractions and compressibilities as a cause for mineral fracturing and annealing. *Contributions to Geology,* **8**, 21-36.

Engebretson, D. C., Cox, A. and Gordon, R. G. (1985) Relative motions between oceanic and continental plates in the Pacific basin. *Geological Society of America Special Paper* **206**.

Gerla, J. P (1988) Stress and fracture evolution in a cooling pluton: An example from the Diamond Joe stock, western Arizona, USA. *Journal of Volcanology and Geothermal Research*, **34**, 267-282.

Grove, M. and Harrison, T. M. (1996) ^{40}Ar* diffusion in Fe-rich biotite. *American Mineralogist*, **81**, 940-951.

Harrison, T. M. (1981) Diffusion of ^{40}Ar in Hornblende. *Contributions to Mineralogy and Petrology*, **78**, 324-331.

Hulin, C. D. (1948) Factors in the localization of mineralized districts. *Transactions of the American Institue of Mining and Metallurgical Engineers*, **178**, 36-52.

Hyndman, D. W. (1985) *Petrology of Igneous and Metamorphic Rocks*. McGraw-Hill Book Co., New York.

Ingraffea, A. R. (1987) Theory of crack initiation and propagation in rock, ed. B. K. Atkinson. *Fracture mechanics of rock*, Academic Press, London, 71-110.

Kistler, R. W., Bateman, P. C. and Brannock, W. W. (1965) Isotopic ages of minerals from granitic rocks of the Central Sierra Nevada and Inyo Mountains, California. *Geological Society of America Bulletin,* **76**, 155-164.

Knapp, R. B. and Norton, D. (1981) Preliminary numerical analysis of processes related to magma crystallization and stress evolution in cooling pluton environments. *American Journal of Science*, **281**, 35-68.

Lisle, R. J. (1989) Paleostress analysis from sheared dike sets. *Geological Society of America Bulletin*, **101**, 968-972.

Lockwood, J. P. and Moore, J. G. (1979) Regional deformation of the Sierra Nevada, California, on conjugate microfault sets. *Journal of Geophysical Research*, **84**, 6041-6049.

Lockwood, J. P. and Lydon, P. A. (1975) Geologic map of the Mount Abbot quadrangle, Sierra Nevada, California: U.S. Geological Survey Geologic Quadrangle Map GQ-1155.

Marsh, B. D. (1989) Magma Chambers. *Annual Review of Earth and Planetary Sciences*, 17,439-474.

Martel, S. J. (1990) Formation of compound strike-slip fault zones, Mount Abbot quadrangle, California. *Journal of Structural Geology*, **12**, 869-882.

Martel, S. J. and Peterson, J. E. (1991) Interdisciplinary characterization of fracture systems at the US/BK site, Grimsel Laboratory, Switzerland. *International Journal of Rock Mechanics and Mining Sciences & Geomechanics Abstracts*, **28**, 295-323.

Martel, S. J., Pollard, D. D. and Segall, P. (1988) Development of simple strike-slip fault zones, Mount Abbot quadrangle, Sierra Nevada, California. *Geological Society of America Bulletin*, **100**, 1451-1465.

McBirney, A. R. (1984) *Igneous Petrology*. Freeman, Cooper and Co., San Francisco.

McGarr, A. (1980) Some Constraints on levels of shear stress in the crust from observations and theory. *Journal of Geophysical Research*, **85**, 6231-6238.

Moore, J. G. (1978) Geologic map of the Marion Peak Quadrangle, Fresno County, California, U.S. Geological Survey Quadrangle Map GQ-1399.

Moore, J. G. (1963) Geology of the Mount Pinchot quadrangle, southern Sierra Nevada, California. *U.S. Geological Survey Bulletin*, **1130**.

Nakamura, K. and Uyeda, S. (1980) Stress gradient in arc-back regions and plate subduction. *Journal of Geophysical Research*, **85**, 6419-6428.

National Academy of Sciences (1996) Rock fractures and fluid flow: contemporary understanding and applications. *National Research Council*.

Nur, A. and Simmons, G. (1970) The origin of small cracks in igneous rocks. *International Journal of Rock Mechanics and Mining Sciences*, **7**, 307-314.

Olson, J. and Pollard, D. D. (1989) Inferring paleostresses from natural fracture patterns: a new method. *Geology*, **17**, 345-348.

Piwinskii, A. J. (1968) Experimental studies of igneous rock series central Sierra Nevada batholith, California. *Journal of Geology*, **76**, 548-570.

Pollard, D. D. and Aydin, A. (1988) Progress in understanding jointing over the past century. *Geological Society of America Bulletin*, **100**, 1181-1204.

Pollard, D. D. and Muller, O. H. (1976) The effect of gradients in regional stress and magma pressure on the form of sheet intrusion in cross section. *Journal of Geophysical Research*, **81**, 975-984.

Pollard, D. D. and Segall, P. (1987) Theoretical displacements and stresses near fractures in rock: With applications to faults, joints, veins, dikes, and solution surfaces, ed. B. K. Atkinson. *Fracture mechanics of rock*, Academic Press, London, 277-349.

Robertson, J. K. and Wyllie, P. J. (1971) Rock-water systems, with special reference to the water-deficient region. *American Journal of Science*, **271**, 252-277.

Secor, D. T. (1965) Role of fluid pressure in jointing. *American Journal of Science*, **263**, 633-646.

Segall, P. (1984) Formation and growth of extensional fracture sets. *Geological Society of America Bulletin*, **95**, 454-462.

Segall, P., McKee, E. H., Martel, S. J. and Turrin, B. D. (1990) Late Cretaceous age of fractures in the Sierra Nevada batholith. *Geology*, **18**, 1248-1251.

Segall, P. and Pollard, D. D. (1983a) Joint formation in granitic rock of the Sierra Nevada. *Geological Society of America Bulletin*, **94**, 563-575.

Segall, P. and Pollard, D. D. (1983b) Nucleation and growth of strike slip faults in granite. *Journal of Geophysical Research*, **88**, p. 555-568.

Segall, P. and Pollard, D. D. (1980) Mechanics of discontinuous faults. *Journal of Geophysical Research*, **85**, 4337-4350.

Sinton, J. M., Langmuir, C. H., Bender, J. F. and Detrick, R. S. (1992) What is a magma chamber?. *Ridge Events*, 3, 46-48.

Skinner, J. B. (1966) *Handbook of physical constants*, Geological Society of America Memoir **97**.

Tikoff, B. and Teyssier, C. (1992) Crustal-scale, en echelon "P-shear" tensional bridges: A possible solution to the batholithic room problem. *Geology*, **20**, 927-930.

Tikoff, B. and Saint Blanquat, M. (1997) Transpressional shearing and strike-slip partitioning in the Late Cretaceous Sierra Nevada magmatic arc, California. *Tectonics*, **16**, 442-459.

Timoshenko, S. P. and Goodier, J. N. (1970) *Theory of* elasticity. McGraw-Hill, New York.

Wang, H. F., Bonner, B. P., Carlson, S. R., Kowallis, B. J. and Heard, H. C. (1989) Thermal stress cracking in granite. *Journal of Geophysical Research*, **94**, 555-568.